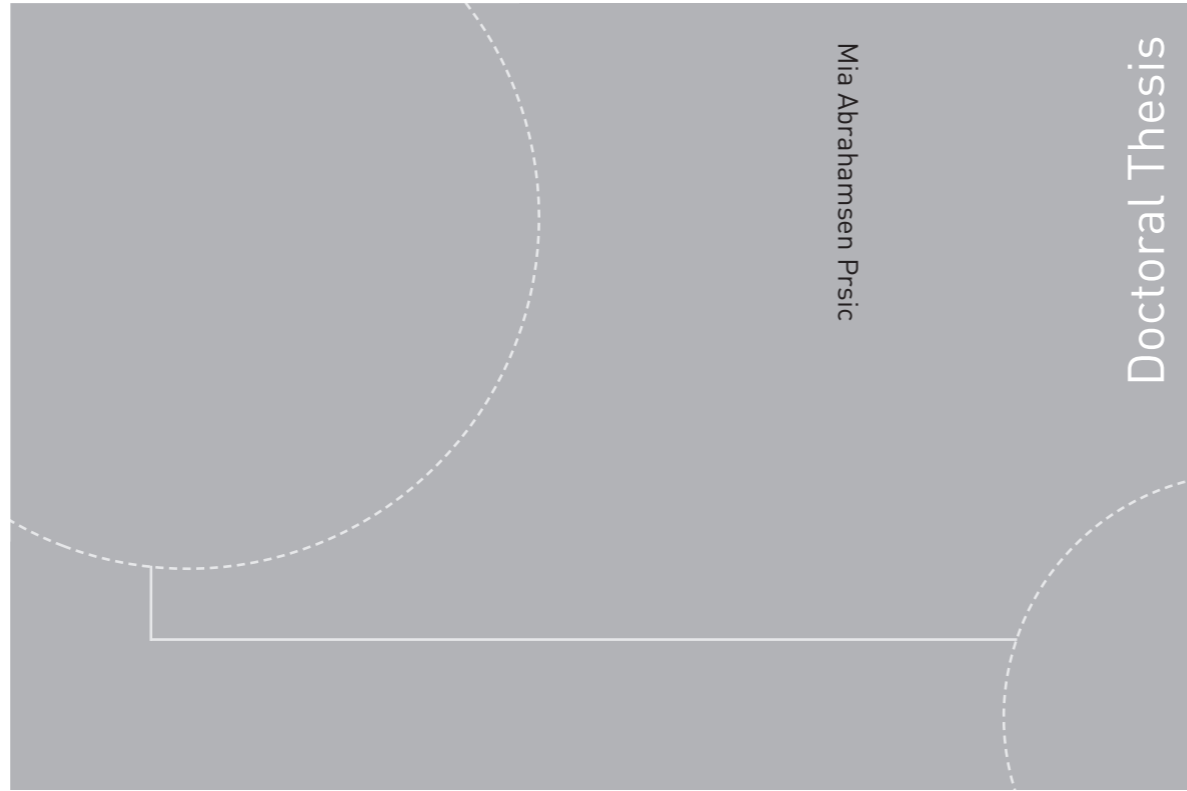


ISBN 978-82-326-1426-4 (printed version)  
ISBN 978-82-326-1427-1 (electronic version)  
ISSN 1503-8181



Doctoral theses at NTNU, 2016:43

Mia Abrahamsen Prsic

## Numerical simulations of the flow around single and tandem circular cylinders close to a plane wall

Mia Abrahamsen Prsic

# Numerical simulations of the flow around single and tandem circular cylinders close to a plane wall

Thesis for the degree of Philosophiae Doctor

Trondheim, February 2016

Norwegian University of Science and Technology  
Faculty of Engineering Science and Technology  
Department of Marine Technology



Norwegian University of  
Science and Technology

**NTNU**

Norwegian University of Science and Technology

Thesis for the degree of Philosophiae Doctor

Faculty of Engineering Science and Technology  
Department of Marine Technology

© Mia Abrahamsen Prsic

ISBN 978-82-326-1426-4 (printed version)  
ISBN 978-82-326-1427-1 (electronic version)  
ISSN 1503-8181

Doctoral theses at NTNU, 2016:43



Printed by Skipnes Kommunikasjon as

# Abstract

In order to model the turbulent flow around cylindrical structures in various configurations, Large Eddy Simulations (LES) are used in the present work. LES utilize a highly accurate model at reasonable time-consumption, offering an insight into the details of a complex flow. Standard Smagorinsky subgrid scale model is used to include the effects of the subgrid scale motions.

Three configurations of cylindrical structures are chosen in this study, inspired by the arrangements of the subsea pipelines in the marine environment. The simplest and most extensive studied arrangement is the flow around a single, smooth circular cylinder in a uniform current. Hence, this configuration is used for the assessment of the numerical tools' performance.

The second configuration, a circular cylinder in the vicinity of a plane wall is chosen to represent the flow around free-spanning subsea pipelines. Performed for various gap to diameter ratios ( $G/D$ ), the simulations successfully capture the details of the flow in the cylinder wake and the interaction with the seabed boundary layer. The influence of the less explored parameters, the thickness and the shape of the inflow profile, is explored. The three-dimensional (3D) LES results show clear improvements over the previously published two-dimensional (2D) simulations.

Two circular cylinders, placed one behind the other, relative to the incoming current, are called the tandem arrangement. The third configuration, tandem cylinders in the vicinity of a plane wall correspond to double pipelines or flowlines in the subsea systems. This configuration has received little research attention. The flow around tandem cylinders close to the wall is therefore compared to the simpler and more thoroughly understood configurations. It is concluded that the existing classification of the flow around one cylinder close to the wall describes well the flow around the upstream cylinder at large horizontal span ratios ( $L/D$ ). Behaviour of the flow around tandem cylinders at large  $G/D$  can be described through the flow classification for the tandem cylinders in the infinite fluid. At intermediate  $G/D$  (and various  $L/D$ ), the presence of the wall causes stronger influence than recorded for the flow around one cylinder at the same  $G/D$ .



# Nomenclature

## *Abbreviations*

2D	Two-dimensional
3D	Three-dimensional
CFD	Computational Fluid Dynamics
CPU	Central processing unit
DDES	Delayed Detached Eddy Simulations
DES	Detached Eddy Simulations
DNS	Direct Numerical Simulations
LES	Large Eddy Simulations
PIV	Particle Image Velocimetry
RANS	Reynolds – Averaged Navier-Stokes Equations
RMS or rms	Root mean square
TRSL	Transition in shear layers flow regime
TRSL1	Transition in shear layers – development of transition waves flow regime
TRSL2	Transition in shear layers – formation of transition eddies flow regime
URANS	Unsteady Reynolds – Averaged Navier-Stokes Equations

## *Greek letters*

$\alpha$	Angle between cylinders' centres and the incoming current for two cylinders in staggered configuration
$\Delta t$	Dimensionless time-step
$\Delta t$ (s)	Dimensional time-step
$\delta$	Thickness of the bottom boundary layer
$\delta/D$	Bottom boundary layer thickness to diameter ratio
$\delta^+$ or $\eta^+$	Dimensionless wall distance
$\theta_s$	Separation angle
$\nu$	Kinematic viscosity of the fluid
$\rho$	Fluid density
$\omega$	Vorticity

## ***Roman letters***

$A$	Projected area of the cylinder exposed to the current
$C_d$	Instantaneous drag coefficient
$\overline{C_d}$	Time-averaged (mean) drag coefficient
$C_l$	Instantaneous lift coefficient
$\overline{C_l}$	Time-averaged (mean) lift coefficient
$ C_l $	Absolute value of the lift coefficient
$C_{l_{rms}}$	Root mean square of the lift coefficient
$C_p$	Pressure coefficient
$\overline{C_p}$	Time-averaged (mean) pressure coefficient
$C$	Courant number
$C_s$	Smagorinsky constant
$D$	Diameter of the cylinder
$f$	Vortex shedding frequency
$f_{St}$	Strouhal number normalized frequency
$F_d$	Drag force
$F_l$	Lift force
$G$	Gap between the cylinder and the bottom wall
$G/D$	Gap to diameter ratio
$(G/D)_c$	Critical gap to diameter ratio
$L$	Longitudinal spacing between the cylinders in tandem configuration
$L/D$	Longitudinal spacing to diameter ratio
$(L/D)_c$	Critical longitudinal spacing to diameter ratio
$L_r$	Mean dimensionless recirculation length
$p_\infty$	Pressure in the undisturbed fluid
$Re$	Reynolds number
$St$	Strouhal number
$T$	Vortex shedding period
$T'$	Transverse spacing between cylinders in the side-by-side arrangement
$U_c$ or $U_\infty$	Undisturbed, inflow velocity
$u_{mean}$ or $U$	Time- and spanwise averaged streamwise velocity component
$v_{mean}$	Time- and spanwise averaged crossflow velocity component
$z_w$	Bed roughness

## ***Subscripts***

1	Upstream cylinder in tandem configuration
2	Downstream cylinder in tandem configuration
x	Streamwise direction
y	Crossflow direction
z	Spanwise direction

## ***General rules for naming of the numerical simulations***

### *Cylinder in a uniform current*

1 <sup>st</sup> term	13100 or 3900 - Reynolds number
2 <sup>nd</sup> term	m, t, sm, sl – key parameters for the convergence study: mesh, time-step, spanwise mesh refinement, spanwise cylinder length
3 <sup>rd</sup> term	1-4 – grade of the mesh/time-step refinement

### *Cylinder in the vicinity of the plane wall*

1 <sup>st</sup> term	gap to diameter ratio
2 <sup>nd</sup> term	key parameters for the convergence study: 1 – the converged case chosen for further analysis i – boundary layer thickness to diameter ratio m – mesh t – time-step L0/4/8 – cylinder spanwise length
3 <sup>rd</sup> term	Reynolds number

### *Tandem cylinders in the vicinity of the plane wall*

1 <sup>st</sup> term	gap to diameter ratio
2 <sup>nd</sup> term	longitudinal spacing to diameter ratio
3 <sup>rd</sup> term	key parameters for the convergence study m – mesh t – time-step





# Acknowledgements

My profound gratitude goes to my supervisors, Prof. Bjørnar Pettersen, Prof. Dag Myrhaug and Prof. Muk Chen Ong. I would like to thank you for your knowledge, patience and guidance. Bjørnar, thank you for the continuous motivation through your curiosity, positivity and new thoughts. Dag, thank you for being the role model of a true researcher in pursuit of the fresh ideas and their thorough understanding. Muk, thank you for sharing vast amounts of your time, knowledge, insights, support, strength, honesty and elan.

I am grateful for being a part of the positive and lively atmosphere at the Department of Marine Technology at the Norwegian University of Science and Technology. Special thanks goes to my colleagues for sharing their thoughts about both hydrodynamics and life, and showing me that chocolate, climbing and music really do complement the research.

This work is performed with support from the Research Council of Norway through the Program for Supercomputing. I am grateful for being provided with the computing time, a crucial component of the present work. I would also like to thank to the staff of NTNU HPC for their quick and professional support.

At the end of the work, at the end of every day, my gratitude goes to my family. I thank mama i tata for teaching me to look into the world with curiosity and belief of a bright future. Bjørn, thank you for being the best companion on every step, sharing your joy, knowledge, experience, and support. Adam, you are the sun of my days. With you two, every road, and so the academic one, makes a wonderful journey.



# Table of Contents

Abstract .....	i
Nomenclature .....	iii
Acknowledgements .....	vii
Table of Contents .....	ix
1. Introduction .....	1
1.1. Background and motivation.....	1
1.2. Outline of the present study.....	3
References .....	6
2. Viscous flow around a circular cylinder .....	7
2.1. Boundary layers and separation.....	7
2.2. Flow regimes around a smooth circular cylinder in a steady current .....	9
References .....	13
3. Circular cylinder in the vicinity of a plane wall .....	15
3.1. Introduction .....	15
3.2. Flow regimes relative to the key parameters .....	16
3.2.1. Influence of the gap to diameter ratio ( $G/D$ ) .....	16
3.2.2. Influence of the boundary layer thickness to diameter ratio ( $\delta/D$ ) .....	20
References .....	23
4. Circular cylinders arranged in tandem configuration .....	25
4.1. Flow around two circular cylinders in close proximity .....	25
4.2. Classification of flow regimes around tandem circular cylinders .....	27
4.3. Influence of the wall proximity .....	30
References .....	34
5. Computational method .....	35
5.1. Modelling of turbulent flows.....	35
5.2. LES with Smagorinsky subgrid scale model.....	36
5.3. OpenFOAM computational package.....	38
References .....	39
6. Large Eddy Simulations of three-dimensional flow around a pipeline in a uniform current.....	41
Abstract .....	41
6.1. Introduction .....	42
6.2. Numerical Method.....	43
6.2.1. Case set-up.....	45
6.3. Results .....	49
6.3.1. Reynolds number 3900.....	49
6.3.2. Results for $Re = 13100$ .....	53

6.4. Conclusions .....	59
References .....	60
7. Large Eddy Simulations of flow around a smooth circular cylinder in a uniform current in the subcritical flow regime .....	63
Abstract .....	63
7.1. Introduction .....	64
7.2. Numerical Method .....	66
7.3. Computational model .....	69
7.4. Results and discussion .....	73
7.4.1. Analysis procedure .....	73
7.4.2. Validation study - Reynolds number 3900 .....	75
7.4.3. Flow around the circular cylinder at $Re = 13100$ .....	79
7.5. Conclusions .....	89
Acknowledgement .....	91
References .....	92
8. Large Eddy Simulations of flow around a circular cylinder close to a flat seabed .....	95
Abstract .....	95
8.1. Introduction .....	96
8.2. Numerical method .....	97
8.2.1. Governing equations .....	97
8.2.2. Computational setup .....	98
8.3. Code validation and convergence studies .....	100
8.3.1. Cylinder in an infinite fluid at $Re = 13100$ – code validation .....	100
8.3.2. Cylinder in the vicinity of a wall - convergence studies .....	100
8.4. Results for the cylinder in the vicinity of a plane wall at $Re=13100$ .....	110
8.4.1. Influence of the gap ( $G/D$ ) .....	110
8.4.2. Influence of incoming boundary layer thickness $\delta/D$ .....	120
8.5. Conclusions .....	125
Acknowledgements .....	126
References .....	127
9. Large Eddy Simulations of flow around tandem cylinders close to a horizontal wall .....	129
Abstract .....	129
9.1. Introduction .....	130
9.2. Numerical method and setup .....	133
9.2.1. Governing equations .....	133
9.2.2. Numerical Setup .....	134
9.3. Convergence study .....	137
9.4. Results .....	140

Conclusions .....	146
References .....	148
10. Large Eddy Simulations of flow around tandem circular cylinders in the vicinity of a plane wall.....	151
Abstract .....	151
10.1. Introduction .....	152
10.2. Numerical method and set-up.....	155
10.2.1. Governing equations.....	155
10.2.2. Numerical set-up.....	157
10.3. Convergence study .....	159
10.4. Results .....	164
10.4.1. Classification of the flow.....	165
10.4.2. Influence of the spacing ratio .....	173
10.4.3. Influence of the gap .....	178
10.4.4. Spanwise variation.....	181
10.5. Conclusions .....	183
References .....	185
11. Conclusions and suggestions for future work.....	189
Appendix: List of additional publications .....	191



# Chapter 1

## Introduction

### *1.1. Background and motivation*

Deep sea, once an untouched vastness, became one of the key focuses of the marine industry. The rapidly developing offshore industry is spreading the fields of operation to progressively deeper water, placing larger and more complex structures in harsher marine environment. An overview of the offshore development was presented by Veldman and Lagers (1997). To assure safety of the structures, accurate predictions of the hydrodynamic forces exerted on these structures became an imperative in marine research.

Circular cylinders are common components of many structures, either of interest to the oil and gas industry, the aquaculture or the renewable energy development. Legs of offshore platforms, spar buoys or mooring systems of the offshore wind turbines, bundles of marine risers, flowlines and umbilicals, frames of fish cages and feeding systems and the subsea pipelines present some common utilisations of the cylindrical structures.

A subsea pipeline, used as motivation for the present work, meets a variety of challenges the industry is facing during installation and maintenance of offshore structures. Commonly placed in deep water, the pipelines are exposed to current, while the wave excitation is negligible. The pipelines may be placed far from all obstacles, acting as isolated, slender circular cylinders, either straight or curved. More often, they rest on the seabed or in its immediate vicinity (on the free-spanning sections, usually in the range between 0.1 and 1 diameter ( $D$ ) away from the seabed). They also appear as two or several parallel circular cylinders at various spacing and configurations regarding physical constraints (Zdravkovich, 2009). The flow fields around such multiple-cylinder configurations with constraints involve complex interaction between the shear layers, vortices and wakes.



Even though the diameter of subsea pipelines can be large (1420 mm in case of Nord Stream (Nord Stream, 2015) and 1067 mm for the Langeled (Langeled Project, 2004), the two longest and largest subsea pipelines), it is significantly smaller than the pipeline's length. Due to the large length to diameter ratios, the slender structures are susceptible to movements and vortex-induced vibrations, exposing it to large hydrodynamic loads. To prevent the damage and potentially fatal failures, it is important to predict the loads correctly and therefore understand the flow around the cylindrical structures and the vortex shedding mechanisms.

The importance of understanding the complex interaction between the flow around the subsea pipeline and the seabed reveals itself through the issue of scour. Placing a subsea pipeline, exposed to a current, near the erodible seabed usually causes an increase in the sediment transport below and behind the pipeline. It further leads to scour and additional loads on the structure as well as to significant modifications of the wake flow behaviour (Sumer and Fredsøe, 2002). It is thus important to understand the details of the complex interaction between the seabed boundary layer and the flow around the pipeline, as well as the wake flow behaviour.

The experimental measurements of the flow around circular cylinders have received large interest over the past 50 years. Covering a large span of Reynolds numbers ( $Re$ ) and many various configurations of circular cylinders and constraints (such as walls, channels, trenches), experiments often offer a good insight into the average forces exerted on the cylinders as well as a general overview of the flow features. However, the details of the complex flow interactions can be difficult to capture by both classical measurements (such as Bearman and Zdravkovich, 1978) and novel measurement technologies, such as Particle Image Velocimetry (Parnaudeau et al., 2008, Wang et al., 2015).

Large Eddy Simulations (LES), a branch of the Computational Fluid Dynamics (CFD), provide highly resolved modelling of the complex boundary layers, wakes and their interaction. The LES results offer an insight in the fine details of the time-dependent behaviour of the flow, wakes and the hydrodynamic loads, thus complementing the experimental results. The rapidly developing computational processing power is beginning to meet the high demands of LES, making them a feasible tool for marine applications. As presented in this study, LES allow for a gradual development of knowledge. The well explored configurations, such as a single circular cylinder in uniform flow, make it possible to compare the results and verify the numerical tool's capabilities. Gradual increase in the complexity of the geometrical configurations can extend the present knowledge with confidence in the quality of the results.

## ***1.2. Outline of the present study***

The physical models explored in the present study are single and tandem subsea pipelines in deep sea, placed in the vicinity of the seabed; and modelled as the infinite, fixed circular cylinders. The cylinders are exposed to a steady flow in the subcritical flow regime, with developed boundary layer in cases where the plane wall is present. The hydrodynamic focus of the present study is to numerically investigate the forces and the flow around circular cylinders in three configurations:

- 1) Single circular cylinder immersed in an infinite fluid with a steady incoming flow;
- 2) Single circular cylinder in the vicinity of a plane wall;
- 3) Two circular cylinders in tandem configuration close to a plane wall.

The chosen numerical tool is LES and OpenFOAM computational package is utilised. LES, allowing 3D modelling with detailed refinement of numerical grid, are applied to the engineering problem of flow around subsea pipelines (in the abovementioned configurations). An objective of this study is to assess the applicability of LES on the abovementioned flows. The other aim is to utilize the LES capabilities for precise modelling of the forces exerted on the cylinders and improving of the understanding about the details of the complex flows around the cylinders in the vicinity of the plane wall.

The thesis consists of two conceptual parts. An overview over the established theories and knowledge supporting the present research is presented in Chapters 2 – 5. The second part consists of a collection of original papers by the author, focusing on the above three specific topics, is presented in Chapters 6 – 10.

Chapter 2 focuses on the fundamental knowledge about the most general configuration – the flow around a single circular cylinder. The main characteristics of the viscous flows are described alongside an overview over various flow regimes of flow around a smooth, circular cylinder immersed in a steady current at various  $Re$ . The focus is put on the subcritical flow regimes.

The general behaviour of the flow around a circular cylinder in the vicinity of a plane wall is described in Chapter 3. Influences of the key parameters – the distance from the wall and the thickness of the incoming boundary layer are distinguished, and paired with the classification of the investigated flow types.

Chapter 4 discusses the flow around two circular cylinders, classifying it regarding the relative position of the two cylinders. The focus is put on the tandem

configuration of the two cylinders, where a classification according to the behaviour of cylinders' wakes is presented. An overview of the present knowledge and the challenges of understanding the flow around tandem cylinders in the vicinity of a wall are also given.

An overview over numerical models commonly used for simulating the turbulent flows around cylindrical structures is given in Chapter 5. LES and the Smagorinsky subgrid scale model, chosen in the present study, are introduced. The OpenFOAM computational package is presented through its general features and specifications of the numerical tools used in the present simulations.

Chapter 6 presents the numerical simulations of the flow around a smooth circular cylinder in a uniform current at  $Re = 3900$  and  $13100$  (Prsic et al., 2012). The flow at  $Re = 3900$  was used in previous studies as a benchmark case, and provides detailed published analysis of the flow physics. It is thus used for a thorough comparison and assessing the capabilities of the chosen numerical model and the computational package. The main results for the higher  $Re = 13100$  show that 3D simulations using LES are suitable for this type of flow.

As the previous Chapter verified the suitability of the numerical simulations, Chapter 7 focuses on the analysis of the flow around a smooth cylinder in moderately high subcritical flow (Abrahamsen Prsic, 2014). Here,  $Re = 13100$  is chosen to mimic the operational conditions of offshore structures. The flow is analysed through the hydrodynamic loads as well as through the time-averaged flow in the cylinder wake. The results compare well with the available experimental measurements.

Chapter 8 discusses the flow around a circular cylinder close to a flat wall. LES are performed for simulating the 3D flow around a circular cylinder at three distances from the wall and immersed in three thicknesses of the incoming boundary layer profile. The influence of these governing parameters is discussed separately, in order to isolate the specific flow phenomena. The behaviour of the flow is discussed through the hydrodynamic forces, the time-averaged velocity profiles in the cylinder wake and through the mean and instantaneous flow fields. The details of the wake behaviour as well as the three-dimensionality of the flow are addressed and comparison to the previously published results is provided.

An initial study of the flow around tandem circular cylinders close to a plane wall is given in Chapter 9 (Abrahamsen Prsic et al., 2015). The cylinders are placed  $1D$  away from the wall and immersed in a steady current with a fully developed boundary layer flow. The distances between the cylinder centres are  $2D$  and  $5D$ . The results are presented through the mean and time-dependant values of the drag- and the lift coefficient, the vorticity and the velocity fields. Due to the relatively large distance

from the plane wall and thus its mild influence on the flow, the results are compared to the flow around tandem circular cylinders in an infinite fluid and in a uniform current, allowing the discussion about the flow specifics.

A more comprehensive study of the flow around tandem circular cylinders in the vicinity of a plane wall is given in Chapter 10. LES were performed for the steady current flow with a logarithmic boundary layer profile at subcritical  $Re = 13100$ . The cylinders are placed in four configurations, i.e. at  $0.6D$  and  $1D$  gap from the wall and with  $2D$  and  $5D$  distances between the cylinders' centres. The focus of the analysis was put on the classification of the flow types, through comparison with the flow around a single cylinder in the vicinity of a wall and the tandem cylinders in an infinite fluid. The time-averaged characteristics of the flow and the time development of the wake behaviour are discussed together with the 3D effects.

Chapter 11 contains an overview of the conclusions for the three chosen topics as well as the recommendations for further work.

## References

Abrahamsen Prsic, M., Ong, M. C., Pettersen, B., and Myrhaug, D. (2014) Large-Eddy Simulations of three-dimensional flow around a smooth circular cylinder in a uniform current in the subcritical flow regime. *Ocean Engineering*, 77, 61-73.

Abrahamsen Prsic, M., Ong, M. C., Pettersen, B., Myrhaug, D. (2015) LES of flow around tandem cylinders close to a horizontal wall. *International Journal of Offshore and Polar Engineering IJOPE*, 25, 3, 161-169.

Bearman, P. W., Zdravkovich, M. M. (1978) Flow around a circular cylinder near a plane boundary. *Journal of Fluid Mechanics*, 89, 33-47.

Langed project (2004) UK/Norway median line to the UK mean low water mark at Easington, East Riding of Yorkshire – Environmental statement. Available on: [www.statoil.com](http://www.statoil.com).

Nord Stream (2015) Secure energy for Europe, the Nord Stream pipeline project 2005-2015. Available on: [www.nord-stream.com](http://www.nord-stream.com).

Parnaudeau, P., Carlier, J., Heitz, D., Lamballais, E. (2008) Experimental and numerical studies of the flow over a circular cylinder at Reynolds number 3900. *Physics of Fluids*, 20, 085101.

Prsic, M., Ong, M. C., Pettersen, B., Myrhaug, D. (2012) Large Eddy Simulations of three-dimensional flow around a pipeline in a uniform current. *Proceedings of 31<sup>st</sup> International Conference on Ocean, Offshore and Arctic Engineering OMAE2012, June 10 – 15, 2012, Rio De Janeiro, Brazil*

Sumer, B. M., Fredsøe, J. (2002) *The Mechanics of Scour in the Marine Environment*. Advanced Series on Ocean Engineering, World Scientific Publishing, Singapore.

Veldman, H., Lagers, G. (1997) *50 Years Offshore*. Foundation of Offshore Studies. Delft, The Netherlands.

Wang, X. K., Zhang, J.-X., Hao, Z., Zhou, B., Tan, S. K. (2015) Influence of wall proximity on flow around two tandem circular cylinders. *Ocean Engineering*, 94, 36-50.

Zdravkovich M. M. (2009) *Flow Around Circular Cylinders, Vol 2: Applications*. Oxford University Press, Oxford, UK.

## Chapter 2

### Viscous flow around a circular cylinder

#### 2.1. *Boundary layers and separation*

The flow around bluff bodies has intrigued human thoughts for centuries. The understanding that the flow around a stationary body causes a region of disturbed flow is documented on the drawings of Leonardo da Vinci in the 15<sup>th</sup> century. The parameters governing the transition of the flow from laminar to turbulent were first discussed in detail by Reynolds (1883). In 1908, Prof. Osborne Reynolds was indorsed for the introduction of the Reynolds number ( $Re$ ), today the most commonly used dimensionless parameter for characterising the flow around cylindrical structures.  $Re$  represents the ratio of inertial to viscous forces, defined as:

$$Re = \frac{DU_c}{\nu} \quad (2.1)$$

where  $U_c$  represents the inflow velocity undisturbed by the presence of the cylinder with diameter  $D$ , and  $\nu$  is the kinematic viscosity of the fluid.

The boundary layer, a thin layer of fluid adjacent to the solid boundary (e.g. wall of the bluff body), is characterized by high vorticity; and the viscous effects are dominant. Boundary layers remain attached to the solid wall unless separation is initiated. The separation occurs due to the development of the adverse pressure gradient. It further causes the shear stress to vanish, and results in the detachment of the boundary layer at the wall surface. Consequently, a free shear layer is formed in the fluid over a bluff body, such as a circular cylinder. The area behind the cylinder, bounded by the shear layers, is called the wake. The vorticity from the boundary layers is conveyed to the free shear layers. The detached shear layers roll up and form vortices, which may be shed further in the cylinder wake. A schematic overview over the characteristic flow regions around a cylinder is given in Figure 2.1a. For the subcritical  $Re = 13100$  (used in the present study), the regions are identified in Figure

2.1b. The flow visualisations obtained by experiments in this Re range were presented by Coutanceau and Defaye (1991).

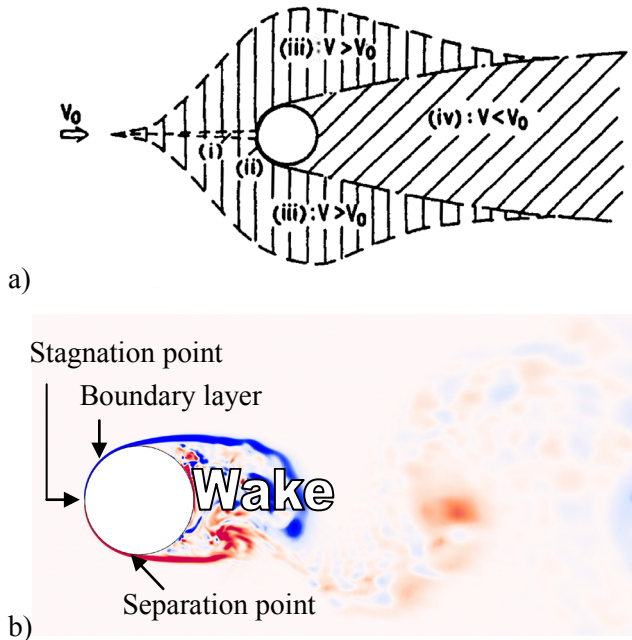


Figure 2.1. Regions of the disturbed flow around a circular cylinder.

a) A schematic overview. (i) stagnation region; (ii) boundary layers attached to the surface of the cylinder; (iii) sidewise regions of accelerated flow; (iv) the wake.  $V_0$  is the velocity of the undisturbed fluid and  $V$  is the local velocity (taken from Zdravkovich (1997)).

b) Identification through instantaneous spanwise vorticity ( $\omega_z$ ). Red colour represents the positive values and blue the negative  $\omega_z$  values.  $Re = 13100$  (present study).

For  $Re > 40$ , the most prominent feature of the flow in the cylinder wake is the vortex shedding. The recognizable street of eddies is created in the cylinder wake, shed interchangeably from the two halves of the cylinder. The alternating procession of eddies was initially observed in the laminar wake by Benard (1908) and von Kármán (1912). The repeating pattern of rolling vortices in the wake of the circular cylinder is therefore often called the Kármán – Benard eddy street.

The vortex shedding frequency is commonly analysed through a dimensionless parameter – the Strouhal number ( $St$ ).

$$St = \frac{fD}{U_c} \quad (2.2)$$

where  $f$  stands for the vortex shedding frequency. The dependency of  $St$  versus  $Re$  is presented in Figure 2.2. For a wide range of  $Re$ , including the subcritical  $Re$  regime (of interest in the present study),  $St$  appears to be a stable parameter, with values around 0.2.

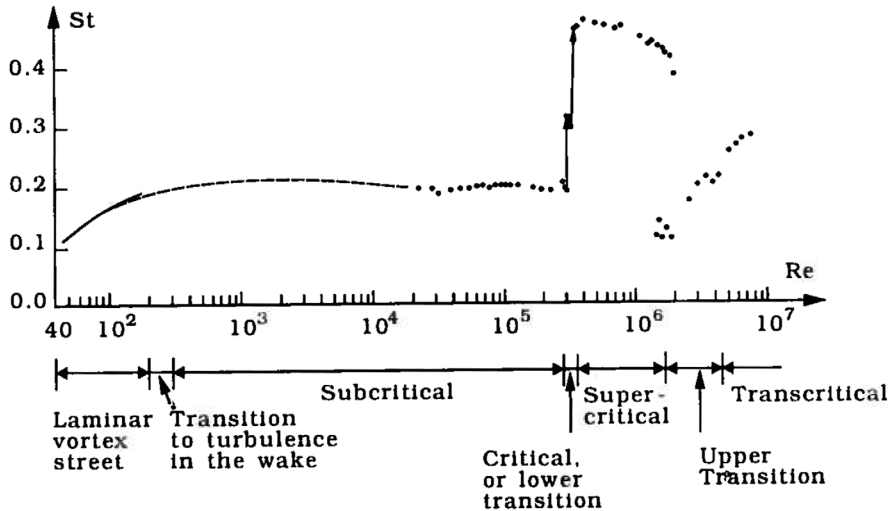


Figure 2.2. Strouhal number for a smooth circular cylinder, presented as a function of  $Re$  (reproduced from Sumer and Fredsøe (2006)).

## 2.2. Flow regimes around a smooth circular cylinder in a steady current

Even though the dominant characteristics of the vortex shedding are present, the flow behaviour undergoes dramatic changes as  $Re$  increases. Various flow regimes around smooth, circular cylinders are categorised by Sumer and Fredsøe (2006) and presented in Figure 2.3.

For low  $Re$ ,  $40 < Re < 200$ , the vortex street is laminar and uniform along the cylinder span. For  $Re < 300$ , the transition to turbulent flow takes place in the cylinder wake, and the transition region moves towards the cylinder as  $Re$  increases. At  $Re = 400$ , the vortices become turbulent at creation (Bloor, 1964). The boundary layer separation, on the other hand, remains laminar for a wide range of  $Re$ , in the entire subcritical regime ranging from  $Re = 300$  up to  $Re = 3 \times 10^5$  (see Figure 2.3). The free shear layer becomes turbulent in the near wake, before rolling up into turbulent eddies.



This regime is called the subcritical (Sumer and Fredsøe, 2006) or the transition-in-shear-layers flow regime (see TrSL in Zdravkovich, 1997).

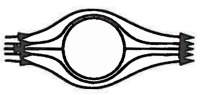
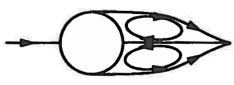


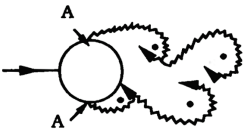
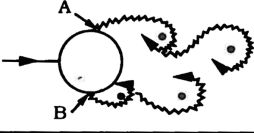
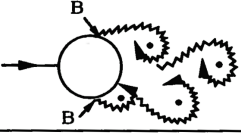
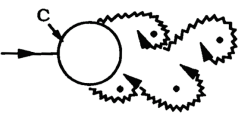
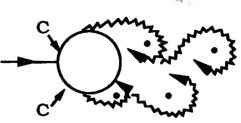
a)		No separation. Creeping flow	$Re < 5$
b)		A fixed pair of symmetric vortices	$5 < Re < 40$
c)		Laminar vortex street	$40 < Re < 200$
d)		Transition to turbulence in the wake	$200 < Re < 300$
e)		Wake completely turbulent. A: Laminar boundary layer separation	$300 < Re < 3 \times 10^5$  Subcritical
f)		A: Laminar boundary layer separation B: Turbulent boundary layer separation; but boundary layer laminar	$3 \times 10^5 < Re < 3.5 \times 10^5$ Critical (Lower transition)
g)		B: Turbulent boundary layer separation; the boundary layer partly laminar partly turbulent	$3.5 \times 10^5 < Re < 1.5 \times 10^6$  Supercritical
h)		C: Boundary layer comple- tely turbulent at one side	$1.5 \times 10^6 < Re < 4 \times 10^6$ Upper transition
i)		C: Boundary layer comple- tely turbulent at two sides	$4 \times 10^6 < Re$ Transcritical

Figure 2.3. Flow regimes around a smooth, circular cylinder in a steady current (taken from Sumer and Fredsøe (2006)).

The TrSL regime is characterised by the 3D vortex shedding; the vortices are shed in cells in the spanwise direction, creating the undulated separation line along the cylinder (Gerrard, 1978). The spanwise variations are illustrated in Figure 2.4, captured through PIV measurements by Parnaudeau et al. (2008) and LES from the present study. The capability to capture the complex, 3D flow, with separation occurring in undulated and fluctuating lines, pointed towards LES as the necessary tool for the present study.

A sub-category of the TrSL regime, called TrSL2, i.e. formation of transition eddies, is characterised by the shortening of the near-wake region and an increase in the drag force (Linke, 1931). Bloor (1964) set the initiation of the TrSL2 regime at  $Re = 1.3 \times 10^4$ , placing  $Re = 1.31 \times 10^4$ , the one of interest in the present study, within this flow regime.

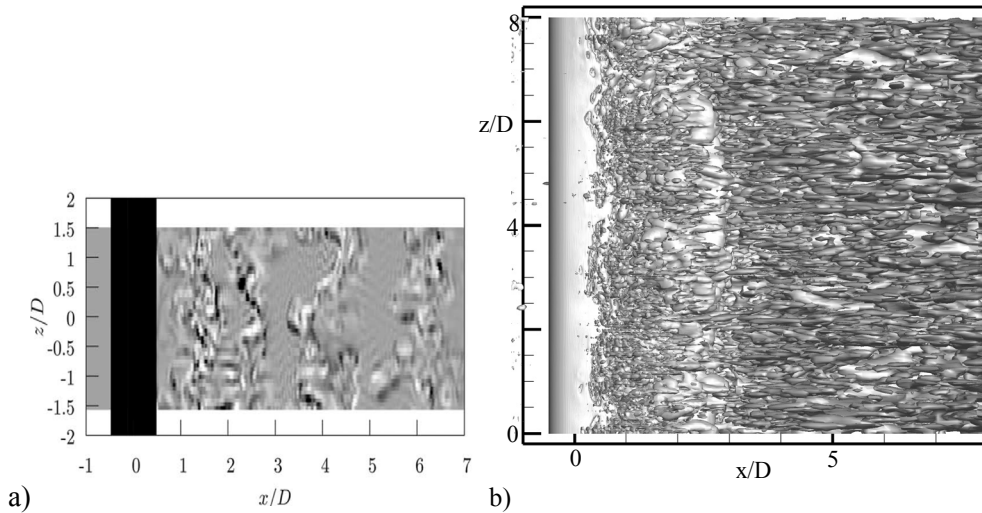
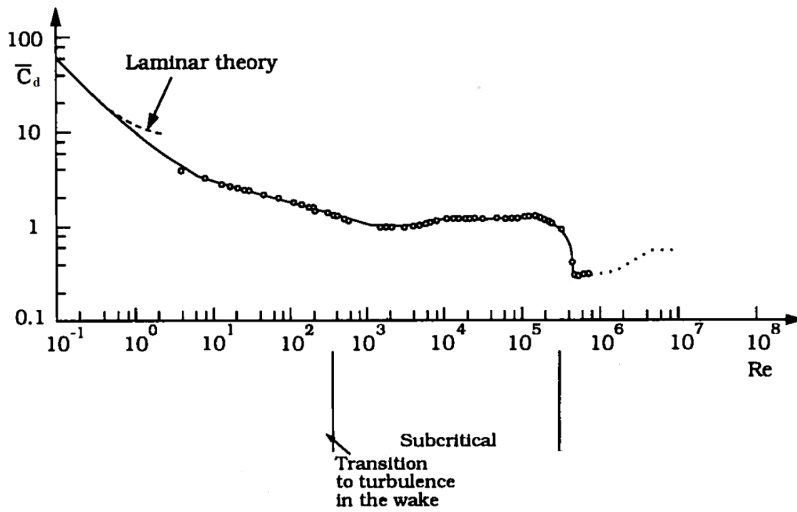


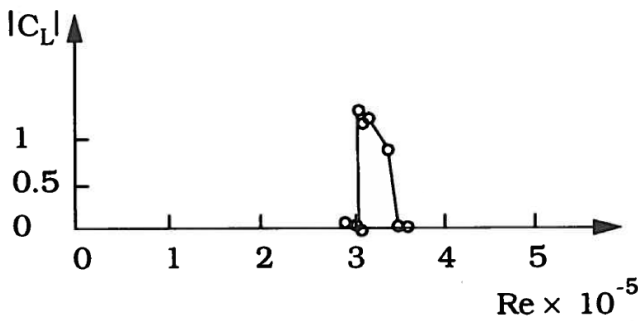
Figure 2.4. Spanwise variations of the flow around a cylinder in the infinite fluid.  
a) Normalized  $y$ -component of vorticity ( $\omega_y D/U$ ).  $L/D = 4$ ,  $Re = 3900$ . PIV measurements (taken from Parnaudeau et al. (2008)).  
b) Instantaneous  $Q = 1$  iso-surface.  $L/D = 8$ ,  $Re = 13100$ . (present study).

With a further increase of the  $Re$ , the transition region moves towards the separation points. For a narrow span of  $Re$ ,  $(3 - 3.4) \times 10^5 < Re < (3.8 - 4) \times 10^5$ , the transition to turbulence at the separation point occurs asymmetrically. The boundary layer at the separation point is turbulent at one side of the cylinder and laminar on the other (Schewe, 1983). This transient regime, also called the critical flow regime, is accompanied with a discontinuous drop in the drag force exerted on the cylinder (see Figure 2.5a) and with a non-zero mean lift force (Figure 2.5b).

Even higher  $Re$  causes the re-establishment of the regular vortex shedding, with transition to turbulence taking place in the boundary layers (Roshko, 1961). Ultimately, the boundary layer around the entire cylinder becomes turbulent, resulting in the transcritical flow regime. The behaviour of the time-averaged (mean) drag force exerted on the cylinder over various flow regimes, presented through the mean drag coefficient ( $\overline{C_d}$ ), is shown in Figure 2.5a. Here,  $C_d = F_d / (0.5\rho U_c^2 A)$  where  $F_d$  is the drag force exerted on the cylinder,  $\rho$  is the density of the fluid, and  $A$  is the projected area of the cylinder



a)



b)

Figure 2.5. a) Drag coefficient for a smooth circular cylinder as a function of  $Re$ . Experimental measurements presented in Schlichting (1979) and Schewe (1983);  
 b) Absolute mean lift coefficient versus  $Re$ . Experiments by Schewe (1983);  
 (reproduced from Sumer and Fredsøe (2006)).

## References

Benard, H. (1908) Formation of centres of gyration in liquids at the back of an object in motion. *Comptes Rendus Hebdomadaires des Seances de l'Academie des Sciences*, 147, 839-842.

Bloor, S. M. (1964) The transition to turbulence in the wake of a circular cylinder. *Journal of Fluid Mechanics*, 19, 290-309.

Coutanceau, M., Defaye, J-R. (1991) Circular cylinder wake configurations: A flow visualization survey. *Applied Mechanics Reviews*, 44, 6, 255-305.

Gerrard, H. (1978) The wakes of cylindrical bluff bodies at low Reynolds number. *Philosophical Transactions of the Royal Society of London A (Mathematical and Physical Sciences)*, 288, 1354, 351-82.

Kármán, T. von (1912) Resistance to motion of body in fluid. *Nachrichten von der Koniglicher Gesellschaft der Wissenschaften zu Göttingen, Mathematisch-Physikalische Klasse*, 5, 547-556.

Linke, W. (1931) New measurements on aerodynamics of cylinders, particularly their friction resistance. *Physikalische Zeitschrift*, 32, 900-914.

Parnaudeau, P., Carlier, J., Heitz, D., Lamballais, E. (2008) Experimental and numerical studies of the flow over a circular cylinder at Reynolds number 3900. *Physics of Fluids*, 20, 085101.

Reynolds, O. (1883) An experimental investigation of the circumstances which determine whether the motion of water shall be direct or sinuous, and the law of resistance in parallel channels. *Philosophical Transactions of the Royal Society of London*, 174, 935-82.

Roshko, A. (1961) Experiments on flow past circular cylinder at very high Reynolds number. *Journal of Fluid Mechanics*, 10, 3, 345-356.

Schewe, G. (1983) On the force fluctuations acting on a circular cylinder in crossflow from subcritical up to transcritical Reynolds numbers. *Journal of Fluid Mechanics*, 133, 265-285.

Schlichting, H. (1979) *Boundary Layer Theory*, 7<sup>th</sup> edition. McGraw-Hill Book Company, New York, USA.

Sumer, B. M., Fredsøe, J. (2006) *Hydrodynamics Around Cylindrical Structures, Revised Edition*. Advanced Series on Ocean Engineering, World Scientific Publishing, Singapore.

Zdravkovich, M. M. (1997). *Flow Around Circular Cylinders, Vol. 1: Fundamentals*. Oxford University Press, Oxford, UK.



## Chapter 3

### Circular cylinder in the vicinity of a plane wall

#### 3.1. Introduction

Assuming  $Re > 40$ , interaction of the shear layers shed from the top and the bottom half of the cylinder is the prerequisite for vortex shedding occurrence. The presence of a plane wall and its boundary layer may reduce or inhibit this interaction, and thus alter or prevent the vortex shedding. The key parameters influencing the flow around a circular cylinder in the vicinity of a wall are the gap ( $G$ ) to diameter ratio ( $G/D$ ) and the boundary layer thickness ( $\delta$ ) to diameter ratio ( $\delta/D$ ).

The presence of the wall influences the symmetry of the flow around the cylinder. The stagnation point changes its angular position towards the gap, the separation point on the upper half of the cylinder moves upstream, while the one on the lower half of the cylinder moves downstream (see Figure 3.1). This causes the asymmetry in the development of the vortices shed from the two sides of the cylinder, allowing the upper vortex to grow larger and stronger than the one shed from

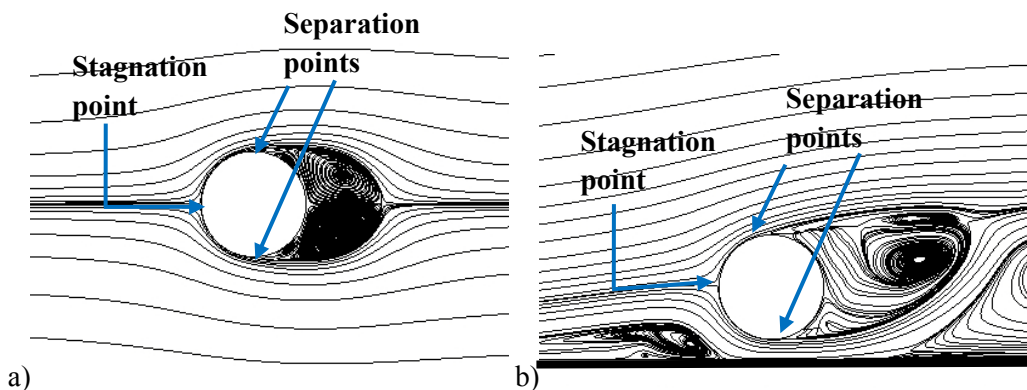


Figure 3.1. Time-averaged streamlines for the flow around a cylinder.  $Re = 13100$ .

a)  $G/D = 0.2$ .; b) cylinder in the infinite fluid (present study).

the bottom half. The difference in the strength between the two vortices reduces the interaction between them, weakening or completely disabling the vortex shedding. The described differences between the flow around a cylinder in an infinite fluid and a cylinder in the vicinity of the wall are presented in details in Sumer and Fredsøe (2006).

### 3.2. Flow regimes relative to the key parameters

#### 3.2.1. Influence of the gap to diameter ratio (G/D)

By analysing the power spectra of the hot wire signals placed in the wake of a circular cylinder at various G/D, Bearman and Zdravkovich (1978) were the first to recognize the clear limit for the vortex shedding suppression, i.e. the critical gap to diameter ratio  $(G/D)_c$ . While measuring within the subcritical regime, they noticed that the vortex shedding ceases to exist for G/D about 0.3. The vortex shedding suppression is clearly detectable through the attenuation of the fluctuating (root-mean-square) values of the lift coefficient ( $C_{l_{rms}}$ ). The lift coefficient is defined as  $C_l = F_l / (0.5\rho U_c^2 A)$ , where  $F_l$  is the lift force exerted on the cylinder, and  $C_{l_{rms}} = \overline{(C_l^2)}^{1/2}$ . Both experimental and numerical studies (Jensen et al., 1990; Lei et al., 1999; Zhao et al., 2007; Ong et al., 2010) show small to negligible oscillations for gaps smaller than the critical gap, and a sudden increase at G/D about 0.3 (Figure 3.2).

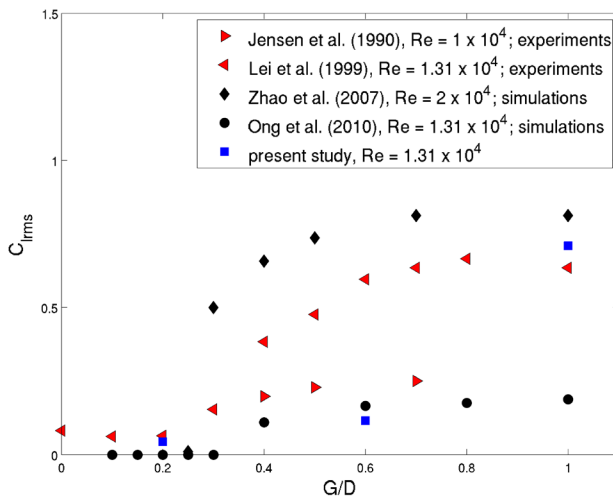


Figure 3.2. Fluctuating lift coefficient ( $C_{l_{rms}}$ ) versus the gap to diameter ratio (G/D) for subcritical Re (present study).

$(G/D)_C$  divides the flow around a circular cylinder in the vicinity of a plane wall into two distinct regimes: a narrow and a wide gap regime. While measuring in the subcritical flow regime ( $Re = 2.5 \times 10^4$ ), Bearman and Zdravkovich (1978) presented photographs of the flow patterns for various  $G/D$ , spanning from  $G/D = 0$  to  $G/D = 2$ . The photographs were obtained by smoke tunnel experiments, where the smoke filaments were injected at the inlet of the tunnel and through a slot in the cylinder. Here,  $G/D = 0.2$  and  $1.2$ , as shown in Figure 3.3a and 3.3b, are chosen as representative cases for the narrow and the wide gap regime.

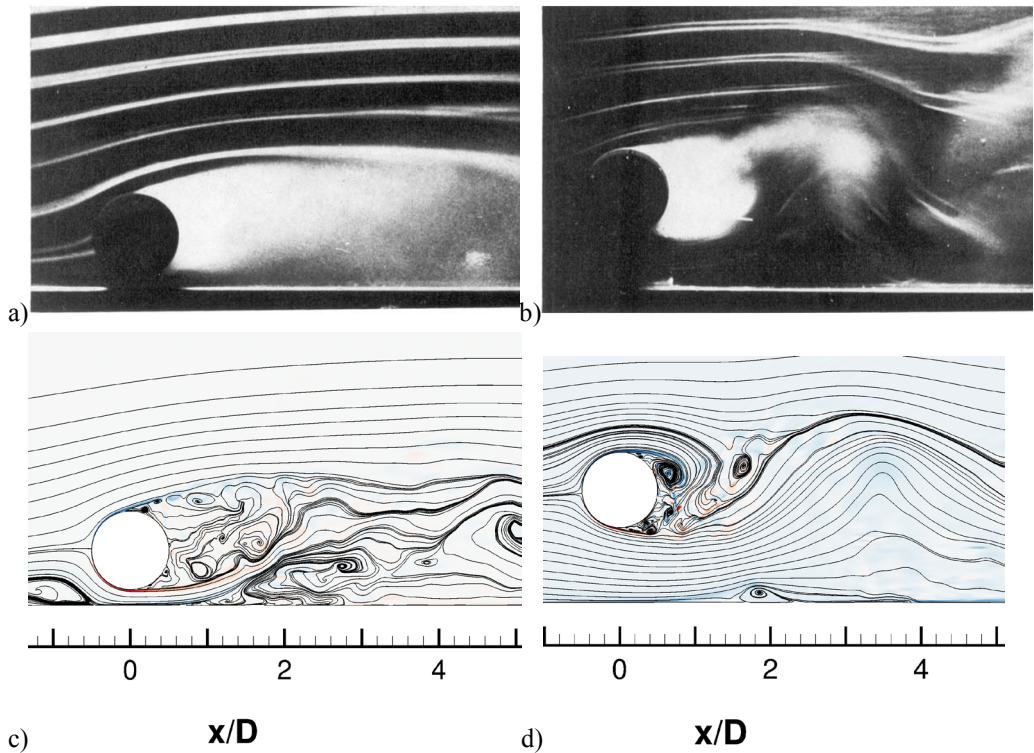


Figure 3.3. Instantaneous flow patterns.

- a)  $G/D = 0.2$ ;
- b)  $G/D = 1.2$ . The smoke tunnel measurements are performed for  $Re = 2.5 \times 10^4$  (figures a and b taken from Bearman and Zdravkovich (1978)).
- c)  $G/D = 0.2$ ;
- d)  $G/D = 1$ . Figures c and d are simulated by LES for  $Re = 1.31 \times 10^4$ . Instantaneous streamlines at the cylinder mid-plane (present study).



The narrow gap regime takes place at  $0 < G/D < (G/D)_c$ . Along with the absence of the vortex shedding, it is characterised by strong asymmetric, upwards deflected wake (see Figure 3.3a and 3.3c). Lei et al. (1999) experimentally analysed the asymmetry of the flow through the displacement of the front stagnation point towards the gap (Figure 3.4). By measuring for various thicknesses of the boundary layer, the results show similar behaviour: the most prominent deflection at small  $G/D$  ratios, and the angle between the horizontal mid-section of the cylinder and the stagnation point ( $\theta_s$ ) approaching 0 for  $G/D > 2$ . The dependency on the boundary layer thickness will be discussed in the following section.

In the narrow gap regime, the separation regions are present both upstream and downstream of the cylinder. The upstream region appears as a separation bubble on the bottom wall, while the downstream one forms an elongated recirculation region, separating the wake from the upwards deflected boundary layer (see Figure 3.3a and 3.3c).

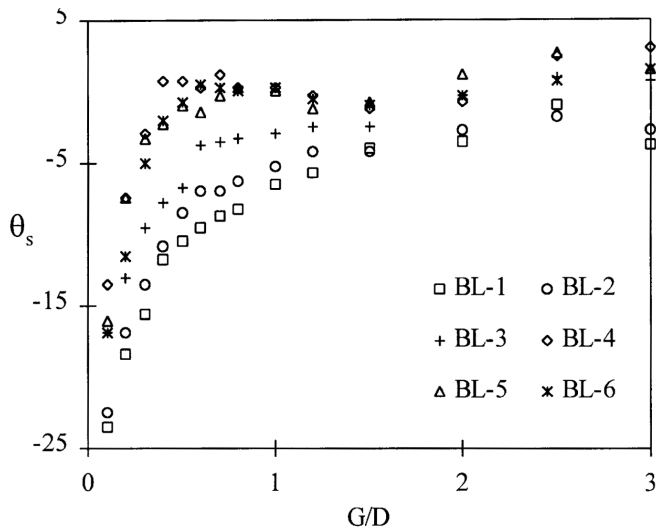


Figure 3.4. Variation of the stagnation point position ( $\theta_s$ ) versus  $G/D$ . BL-1 to BL-6 denote various thicknesses of the incoming boundary layer, varying from 0.14 to 2.89, respectively (taken from Lei et al. (1999)).

The regular, periodic vortex shedding in the cylinder wake is re-established in the wide gap regime. However, the asymmetry of the wake flow can be noticed until  $G/D > 2$ , where the effect of the boundary is negligible. Even though the influence of the wall is relatively mild for the wide gaps ( $G/D > 1$ ), and the vortices shed from the cylinder appear nearly symmetric in the near wake, attention needs to be paid to the far wake. The development of the wake vortices over one vortex shedding period and their interaction with the plane wall are presented in Figure 3.5.

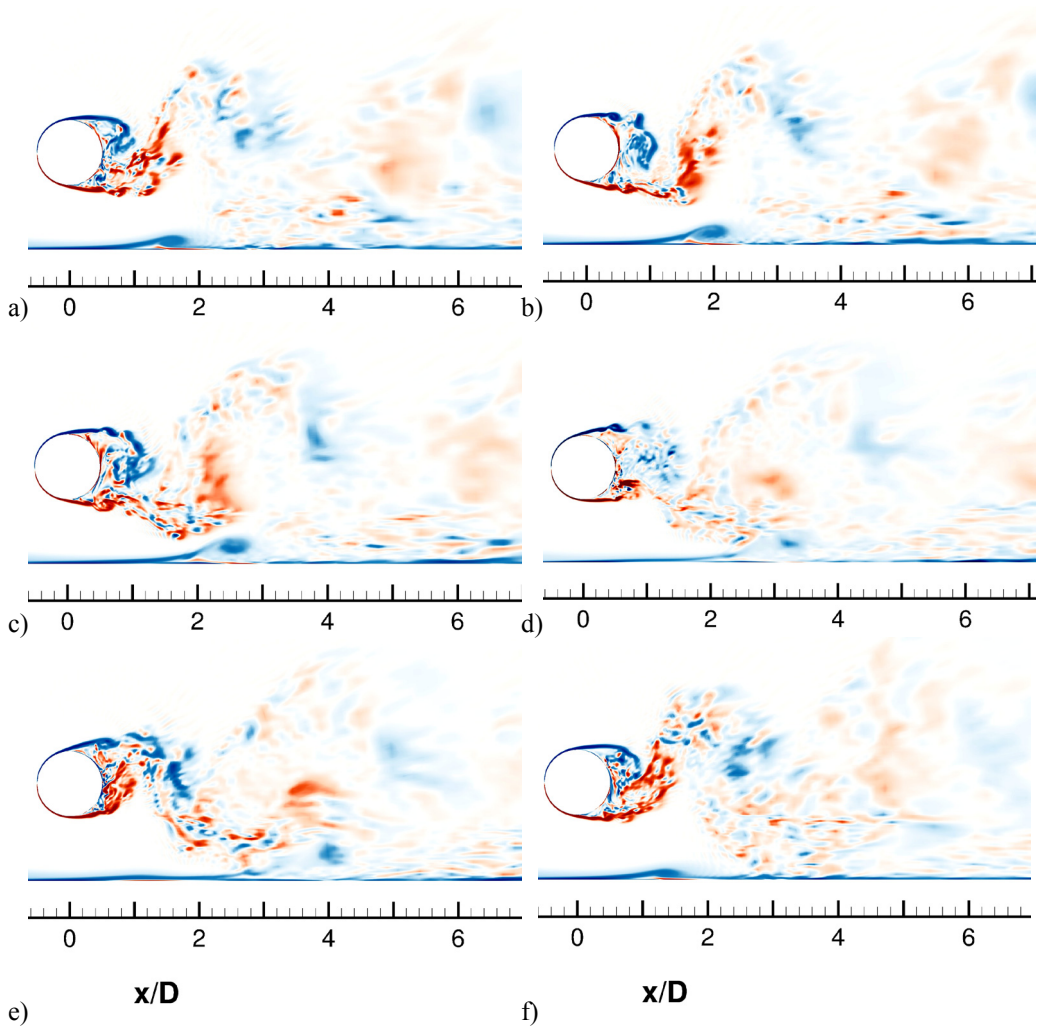


Figure 3.5. Development of the instantaneous spanwise vorticity  $\omega_z$  through one vortex shedding period ( $T$ ). Vertical cross-section at  $z/D = 2$ .  $Re = 1.31 \times 10^4$ ,  $G/D = 1$ ;  $\delta/D = 1.6$ . The figures correspond to  $t = 0T$  (a),  $1/6T$  (b),  $1/3T$  (c),  $1/2T$  (d),  $2/3T$  (e),  $5/6T$  (f). Red colour denotes positive and blue negative  $\omega_z$  (present study).

Strong eddies rolling up in the vicinity of the plane wall periodically disturb the bottom boundary layer, they get distorted and reduce speed in the process. This behaviour is important for the phenomenon of scour under subsea pipelines as well as for understanding the forces exerted on any objects placed in the wake of a circular cylinder in the vicinity of a rigid wall.

The wider gap allows the fluid to flow more freely between the cylinder and the wall, leading to the weakening and eventual disappearance of the upstream separation bubble (present at  $x/D < -0.4$  for the narrow gap regime, see Figure 3.3c).

As shown in Figure 3.3b and 3.3d, the downstream region is characterised by stronger and equally spaced eddies. The vortex shedding frequency does not undergo significant changes for  $G/D > (G/D)_C$ , as documented by experimental research of, amongst others, Price et al. (2002) and Wang and Tan (2008) in Figure 3.6.

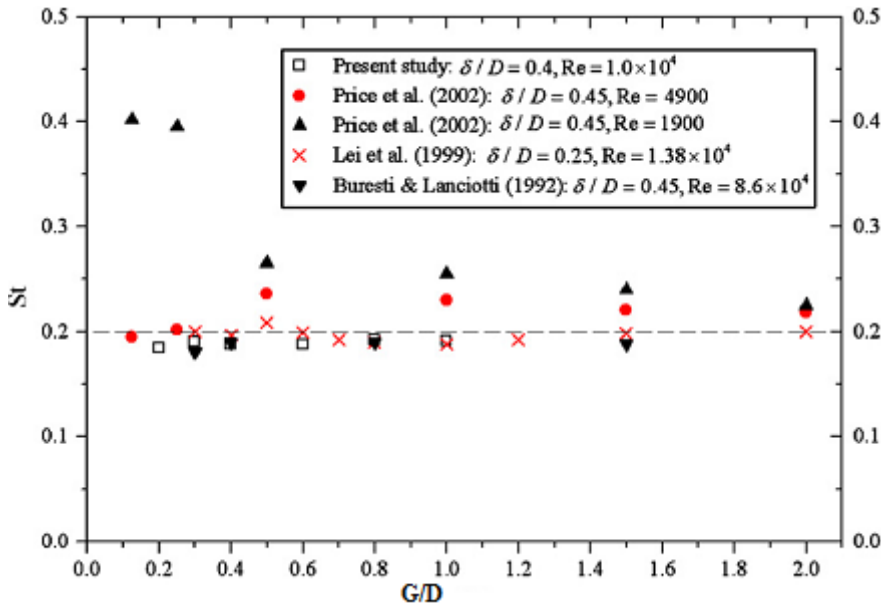


Figure 3.6. Variation of the Strouhal number ( $St$ ) versus the gap-to-diameter ratio ( $G/D$ ) (reproduced from Wang and Tan (2008)).

### 3.2.2. Influence of the boundary layer thickness to diameter ratio ( $\delta/D$ )

According to Zdravkovich (2009), another parameter governing the flow around a circular cylinder in the vicinity of a plane wall is the ratio of the wall boundary layer thickness and the cylinder diameter ( $\delta/D$ ). The influence of  $\delta/D$  can be detected through the behaviour of  $\overline{C_d}$  versus  $G/D$ . Contrary to the behaviour of  $C_{l,rms}$ , which experiences a sudden increase as  $G/D$  exceeds the critical value;  $\overline{C_d}$  continues to increase as  $G/D$  increases, up to a value between 1 and 2, and it remains nearly constant afterwards. This trend is reported by Lei et al. (1999) for the subcritical  $Re$  between  $1.3 \times 10^4$  and  $1.38 \times 10^4$  for various boundary layer thicknesses (see Figure 3.7a).

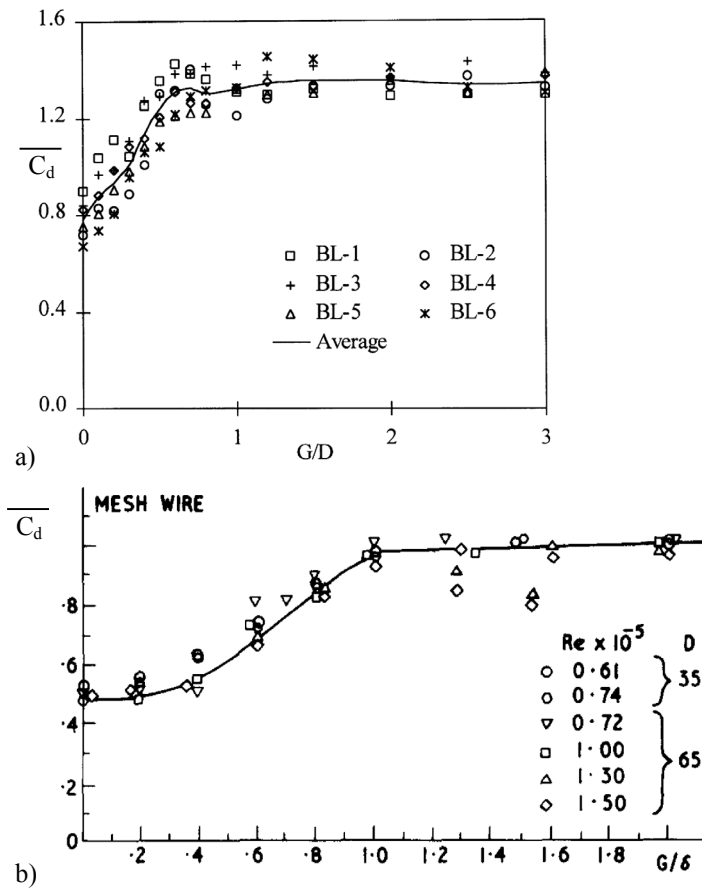


Figure 3.7. Mean drag coefficient ( $\overline{C_d}$ ) for a circular cylinder in the vicinity of a wall.

- a)  $\overline{C_d}$  versus  $G/D$ . BL-1 to BL-6 denote various thicknesses of the incoming boundary layer, spanning from 0.14 to 2.89, respectively (reproduced from Lei et al. (1999)).
- b)  $\overline{C_d}$  versus  $G/\delta$  (reproduced from Zdravkovich (1985)).

Zdravkovich (1985) accounted such prolonged increase of  $\overline{C_d}$  to the presence of the wall boundary layer. Contrary to the commonly used  $G/D$ , a new parameter,  $G/\delta$  was introduced, combining the governing influences on the flow around a circular cylinder in the vicinity of a wall. A series of experiments for subcritical  $Re$  between  $6.1 \times 10^4$  and  $1.5 \times 10^5$  show similar behaviour (Zdravkovich, 1985). An increase of  $\overline{C_d}$  is measured for  $G/\delta < 1$ . As  $G/\delta$  exceeds 1, the cylinder is not longer immersed within the boundary layer, resulting in a nearly constant  $\overline{C_d}$  for all  $G/\delta > 1$  (Figure 3.7b).

Another approach to understand the influence of the cylinder immersion into the shear flow was presented by Fredsøe et al. (1985). By focusing on the narrow gap regime, two sets of experiments were performed for each  $G/D$ . First, the cylinder was towed at a constant speed in otherwise still water, obtaining the subcritical  $Re$ . Second, the same  $Re$  was obtained by exposing the same cylinder (kept fixed) to a steady current. The boundary layer was developed on the wall ( $\delta/D = 5$ ), exposing the steady cylinder to a shear flow. The results are shown in Figure 3.8. The first set of experiments yielded the mean lift coefficient ( $\bar{C}_l$ ) corresponding to the modified potential theory (Fredsøe and Hansen, 1987). When the cylinder was exposed to the shear in the incoming flow, large variations of  $\bar{C}_l$  were obtained within the narrow gap regime.

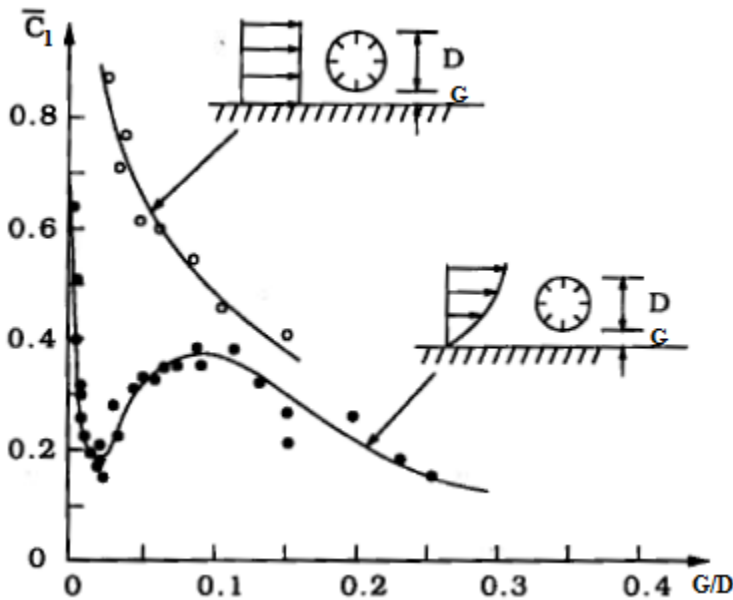


Figure 3.8. Mean lift coefficient ( $\bar{C}_l$ ) versus  $G/D$ . Empty symbols – shear free flow, full symbols – shear flow with boundary layer thickness to diameter ratio  $\delta/D = 5$  (reproduced from Fredsøe et al. (1985)).

## References

- Bearman, P. W., Zdravkovich, M. M., 1978. Flow around a circular cylinder near a plane boundary. *Journal of Fluid Mechanics*, 89, 33-47.
- Fredsøe, J., Sumer, B. M., Andersen, J., Hansen, E. A. (1985) Transverse vibrations of a cylinder very close to a plane wall. *Transcripts of the ASME, Journal of Offshore Mechanics and Arctic Engineering*, 109, 52-60.
- Fredsøe, J., Hansen, E. A. (1987) Lift forces on pipelines in steady flow. *Journal of Waterway, Port, Coastal and Ocean Engineering, ASCE*, 113, 2, 139-155.
- Jensen, B. L., Sumer, B. M., Jensen, H. R., Fredsøe, J. (1990) Flow Around and Forces on a Pipeline Near a Scoured Bed in Steady Current. *ASME Journal of Offshore Mechanics and Arctic Engineering*, 112, 206-213.
- Lei, C., Cheng, L., Kavanagh, K. (1999) Re-examination of the effect of a plane boundary on force and vortex shedding of a circular cylinder. *Journal of Wind Engineering and Industrial Aerodynamics*, 80, 263-286.
- Ong, M. C., Utnes, T., Holmedal, L. E., Myrhaug, D., Pettersen, B. (2010) Numerical simulation of flow around a circular cylinder close to a flat seabed at high Reynolds numbers using a k- $\epsilon$  model. *Coastal Engineering*, 57, 10, 931-947.
- Price, S. J., Sumner, D., Smith, J. G., Leong, K., Paidoussis, M. P. (2002) Flow visualization around a circular cylinder near to a plane wall. *Journal of Fluids and Structures*, 16(2), 175-191.
- Sumer, B. M., Fredsøe, J. (2006) *Hydrodynamics Around Cylindrical Structures, Revised Edition*. Advanced Series on Ocean Engineering, World Scientific Publishing, Singapore.
- Wang, X. K., Tan, S. K. (2008) Comparison of flow patterns in the near wake of a circular cylinder and a square cylinder placed near a plane wall. *Ocean Engineering*, 35, 458-472.
- Zdravkovich, M. M. (1985) Forces on a circular cylinder near a plane wall. *Applied Ocean Research*, 7, 4, 197-201.
- Zdravkovich M. M. (2009) *Flow Around Circular Cylinders, Vol 2: Applications*. Oxford University Press, Oxford, UK.
- Zhao, M., Cheng, L., Teng, B. (2007) Numerical modeling of flow and hydrodynamic forces around a piggyback pipeline near the seabed. *Journal of Waterway, Port, Coastal and Ocean Engineering*, 133, 4, 286-295.



## Chapter 4

### Circular cylinders arranged in tandem configuration

#### 4.1. *Flow around two circular cylinders in close proximity*

In marine structures, circular cylinders often appear in pairs or bundles. The modifications of the flow around each cylinder, due to the presence of the other cylinder(s), might vary from mild to dramatic, depending on  $Re$ , the distance between the cylinders, and the incident angle of the incoming flow. The flow interference between two or more cylinders in close proximity may cause significant changes to the flow patterns, the vortex shedding and, consequently, the forces exerted on each of the cylinders.

Basic categorisation of the arrangement of two cylinders in close proximity was proposed by Zdravkovich (1977). Assuming a uniform incoming flow, pairs of cylinders are divided in three categories according to their orientation relative to the incident flow (see Figure 4.1). Two cylinders placed one behind the other, relative to the free stream, are called the tandem arrangement. The governing parameter in this case is the longitudinal spacing ratio, defined as the normalized distance between the centres of the cylinders ( $L/D$ ).

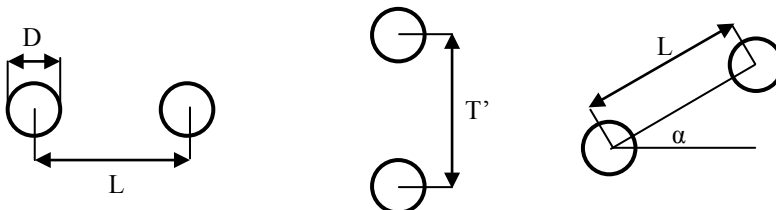


Figure 4.1. Definition sketch of tandem, side-by-side and staggered arrangements.



In the side-by-side arrangement, the two cylinders are positioned transverse to the flow, both facing the incoming free stream and allowing the wakes to interact on each side of the spacing. Here, the key interference parameter is the transverse spacing ratio ( $T'/D$ ). The most general category is called the staggered arrangement. In addition to the distance between the cylinders centres ( $L/D$ ), the angle between the cylinders' centres and the free stream ( $\alpha$ ) governs the flow interaction. In this arrangement, the downstream cylinder can be exposed to the free stream, or shielded by the upstream cylinder.

The tandem and the side-by-side arrangements from the study by Zdravkovich (1977) present the idealised cases where the oncoming flow encounters a pair of cylinders either perpendicular or in parallel to the cylinders' axis. The third arrangement, the staggered cylinders, is the one most often encountered in engineering practice. However, the extra parameter  $\alpha$  allows for various combinations of arrangements, making the flow around staggered cylinders difficult to categorise. Due to its applicability to the pair of cylinders in the vicinity of a wall (such as tandem pipelines near the seabed), and the availability of previously published data, the present study focuses on two cylinders arranged in a tandem.

Following the above categorisation of the cylinders' arrangements, Zdravkovich (1987) identified three basic types of flow interference: wake interference, proximity interference, and the combined proximity and wake interference. Outside of these regions, the flow is expected to behave as around a single cylinder in an infinite fluid (see Figure 4.2).

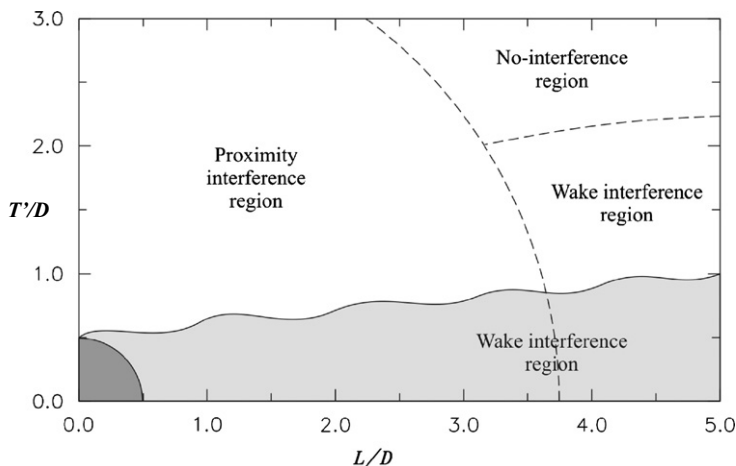


Figure 4.2. Schematic overview over the basic types of flow interference, dependent on the position of the downstream cylinder relative to the upstream cylinder. The scheme is based on definitions by Zdravkovich (1987) (taken from Sumner (2010)).

In the wake interference region, the downstream cylinder is affected by the wake of the upstream cylinder. Depending on the distance between the cylinder centres, several sub-categories are presented in Zdravkovich (1987). The proximity interference, due to small spacing between the cylinders, might result in a single eddy street, where the two cylinders act as one bluff body; or cause an interaction between the wakes of the two cylinders. The combined proximity and wake interference occurs for various staggered arrangements of the two cylinders, causing the narrowing of the upstream cylinder wake and widening of the wake shed from the downstream cylinder.

Alongside the above described basic classification, three other approaches were used to understand and classify the complex flow around two circular cylinders in steady current. First, classification through classic, single-value experimental data, such as vortex shedding frequencies and mean drag and lift coefficients, offered precisely quantifiable values, useful for engineering practice. However, the measurement-only approach, based on time-averaged values, did not explain the complex fluid behaviour.

The second approach, based on flow visualisation, was therefore developed. By focusing mostly on circular cylinders in tandem arrangement, Igarashi (1981) initiated this approach. Followed by Ljungkrona et al. (1991), more precise classification of the flow patterns was developed. This is further described in Section 4.2. According to Sumner (2010), the third approach – numerical simulations, has been less popular and successful. The advances in the large data processing and the numerical modelling led to recent increased interest and advances in the topic, also giving the motivation for the present study.

## ***4.2. Classification of flow regimes around tandem circular cylinders***

As the downstream cylinder in the tandem arrangement is shielded behind the upstream cylinder, the wake behind the upstream cylinder is determining the incoming flow for the downstream one. On the other hand, the presence of the second cylinder affects the wake flow and the vortex formation of the upstream cylinder. In addition to  $Re$ ,  $L/D$  is thus the key factor governing the flow around tandem circular cylinders.

The critical longitudinal spacing ratio  $(L/D)_c$ , is often used for a coarse classification of the flow. At spacing ratios smaller than the critical, the vortex shedding from the upstream cylinder is suppressed (see Figure 4.3a), while  $L/D > (L/D)_c$  allow the development of the vortex street (Figure 4.3b). The changes in the

nature of the flow are reflected on the various experimentally measured parameters. Igarashi (1981, 1984) analysed the pressure coefficient around the downstream cylinder ( $C_{p2}$ ) for the tandem arrangement in the subcritical flow regime, and noticed a change in the  $C_{p2}$  curves at  $L/D > 3.82$ . Here,  $C_{p2} = (p_2' - p_\infty) / (0.5\rho U_c^2)$  where  $p_2'$  is the pressure at the sampling point at the downstream cylinder and  $p_\infty$  is the pressure in the undisturbed flow. The mean drag coefficients exhibit even stronger discontinuities in the same  $L/D$  region (see Figure 4.4). Hiwada et al. (1982) reported a similar jump in the vortex shedding frequency of the downstream cylinder. For  $Re = 5 \times 10^4$ , the discontinuity in their study occurred at  $3.3 < L/D < 4$ .

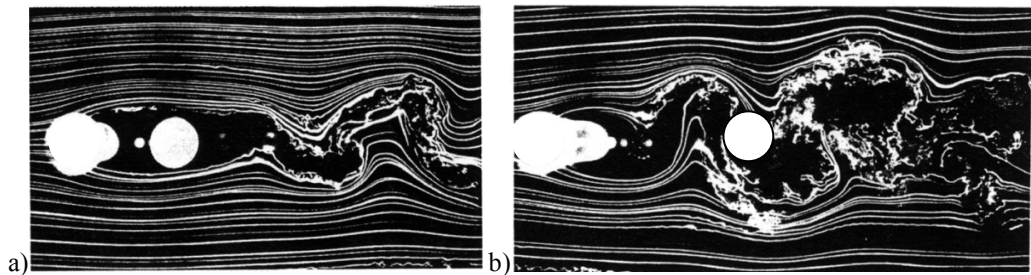


Figure 4.3. Visualisation of the flow around tandem cylinders in the infinite fluid:

- a)  $L/D = 2$ ;
- b)  $L/D = 5$ . Wind tunnel experiments,  $Re = 1.2 \times 10^4$  (reproduced from Ljungkrona and Sunden (1993)).

Following the classification approach of the flow visualisation, more detailed characteristics of the flow were analysed, leading to a refined categorisation of the flow behaviour by Igarashi (1981). Depending on  $L/D$  and  $Re$ , seven categories were recognised, including several unstable or transient regimes (see Figure 4.5). As the key or the categorisation, Igarashi (1981) used the behaviour of the shear layers shed from the upstream cylinder (which may either cease to, or reattach to the downstream cylinder, or roll up intermittently or completely in front of the downstream cylinder). A new, simplified classification was suggested by Zhou and Yiu (2006). Three basic flow regimes are recognized: the extended body, the reattachment and the co-shedding regime (see Figure 4.6).

Placed in very close proximity,  $1 < L/D < 1.2 - 2$  (Zdravkovich, 1987, Zhou and Yiu, 2006), tandem cylinders behave as a single, elongated body. The shear layers shed from the upstream cylinder wrap around the downstream cylinder and develop alternating vortices in its wake (Figure 4.6a). The created vortices are more elongated and shed at a slightly higher frequency compared to the case of a single cylinder.

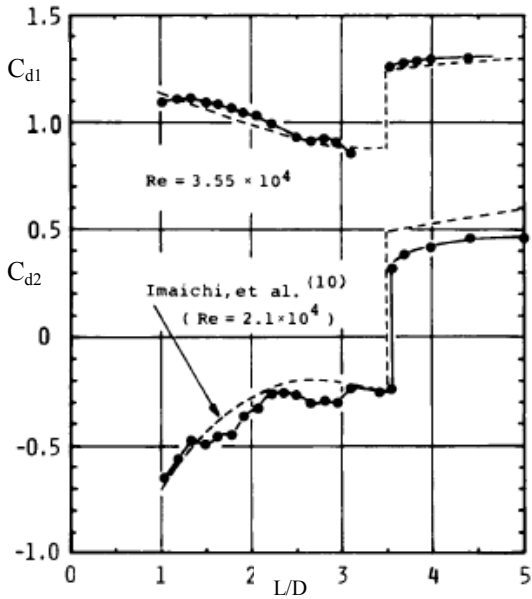


Figure 4.4. Mean drag coefficient for the upstream ( $C_{d1}$ ) and the downstream cylinder ( $C_{d2}$ ) versus  $L/D$ .  $Re = 3.55 \times 10^4$  (taken from Igarashi (1981)).

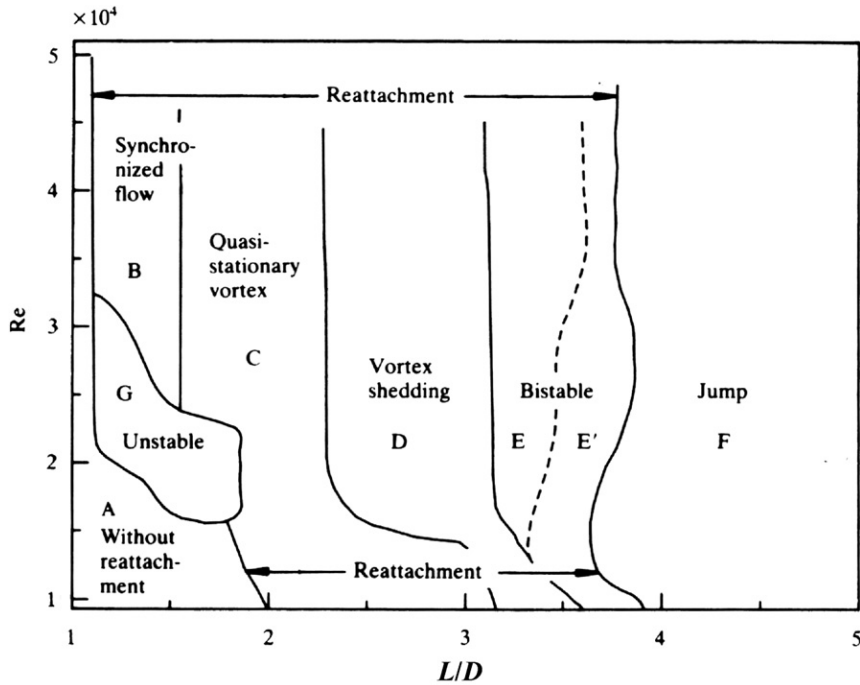


Figure 4.5. Schematic overview over flow patterns past tandem circular cylinders in an infinite fluid for various  $L/D$  and various  $Re$  within the subcritical flow regime (reproduced from Igarashi (1984)).

For  $L/D$  range beginning at 1.2 – 1.8 (Zdravkovich, 1987) or 2 (Zhou and Yiu, 2006) and up to 5, the reattachment regime occurs. Here, the upstream cylinder shear layers reattach on the surface of the downstream cylinder. The reattachment may alternately take place on the front side of the downstream cylinder for smaller  $L/D$ . The intermediate spacing ratios allow nearly continuous reattachment at the back side of the downstream cylinder (Figure 4.6b1), and almost steady reattachment at the front half for higher  $L/D$  within the reattachment regime (Figure 4.6b2). The vortex shedding from the upstream cylinder is suppressed, while the vortices behind the downstream cylinder may be weakened due to the interference of the downstream cylinder boundary layer and the reattached shear layers from the upstream cylinder.

At even higher  $L/D$  a vortex street develops behind the upstream cylinder. Placed sufficiently far in the wake ( $L/D > 5$ ), the downstream cylinder ceases to affect the flow around the upstream cylinder, which gradually acquires the behaviour of a single cylinder in an infinite fluid. The downstream cylinder, on the other hand, experiences a strong influence of the upstream cylinder wake flow. It is immersed in the flow of high vorticity, where the vortices shed from the upstream cylinder impinge periodically on the downstream cylinder (Figure 4.6c).

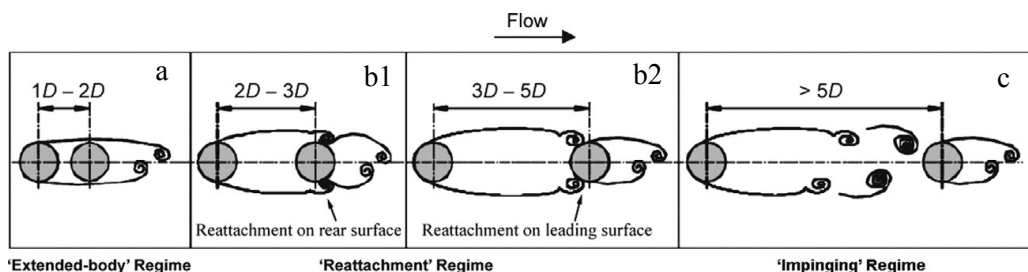


Figure 4.6. Simplified classification scheme of the flow (reproduced from Zhou and Yiu (2006)).

### 4.3. Influence of the wall proximity

Placed in the vicinity of a plane wall, two circular cylinders are subjected to a very complex flow. Similar as in the case of tandem cylinders in an infinite fluid, the nature of the flow highly depends on  $L/D$ . The presence of the second cylinder may allow or completely suppress the vortex shedding from the upstream cylinder, and modify the wake of the downstream cylinder. Similarly, the proximity of the plane wall and the immersion in the wall boundary layer may restrict the vortex shedding and distort the wake flow behind the cylinders. Combinations of these two effects result in

a complex interaction between the boundary and the shear layers, the wake flow and the vortices. To exemplify the variety of the flow types, the experimental and numerical results of the flow around tandem cylinders at  $L/D = 2$  and  $5$  and  $G/D = 0.6$  are shown in Figure 4.7. Comparison to the flow around a single cylinder (Figure 3.3) and tandem cylinders in an infinite fluid (Figure 4.3) indicates that the flow behaviour is strongly altered due to the combined effects of the plane wall and the tandem cylinders.

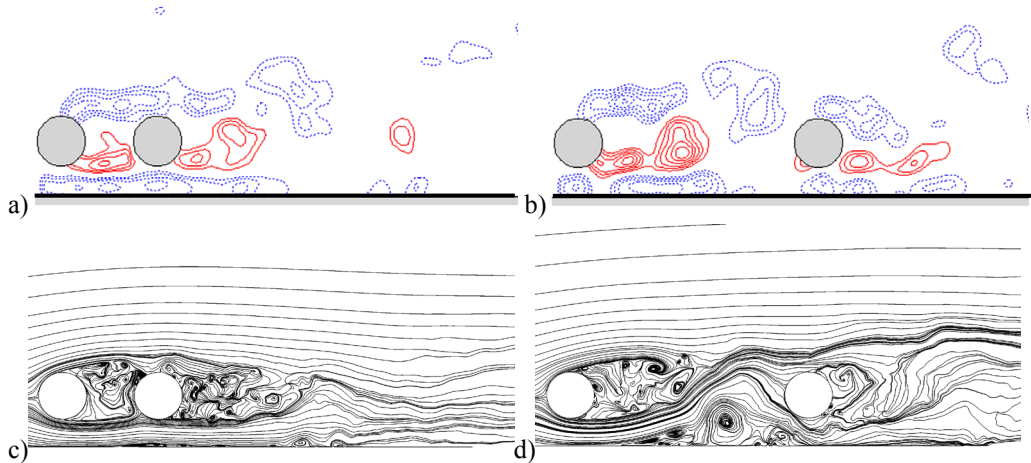


Figure 4.7. Visualisation of the flow around tandem tandem cylinders close to a plane wall:

- a)  $L/D = 2, G/D = 0.6$ ;
- b)  $L/D = 5, G/D = 0.6$ .  $Re = 6.3 \times 10^3$ , circulating channel experiments, PIV measurements (figures a and b are taken from Wang et al. (2015)).
- c)  $L/D = 2, G/D = 0.6$ ;
- d)  $L/D = 5, G/D = 0.6$ . LES,  $Re = 1.31 \times 10^4$  (figures c and d are from the present study).

Despite its importance to engineering, very little research has been published about the configuration of two tandem circular cylinders in the vicinity of a plane wall. The flow at low  $Re = 200$  was explored by Bhattacharyya and Dhinakaran (2008) and at  $Re = 100$  and  $200$  by Harichandan and Roy (2012). At subcritical  $Re = 6.3 \times 10^4$ , Wang et al. (2015) conducted a series of experiments of the flow around tandem circular cylinders for  $L/D$  between  $1.5$  and  $7$ , and  $G/D$  between  $0.15$  and  $2$ . Based on the instantaneous vorticity, extracted from the PIV flow visualization, they proposed a map of basic flow types. They discerned three categories for  $L/D$ : the close, the moderate and the wide spacing, as well as three categories for  $G/D$ : the small, the intermediate and the wide gap regime. A schematic overview of the principal behaviour of the shear layers shed from the upstream and the downstream cylinder, as well as the interaction with the wall boundary layer is shown in Figure 4.8.

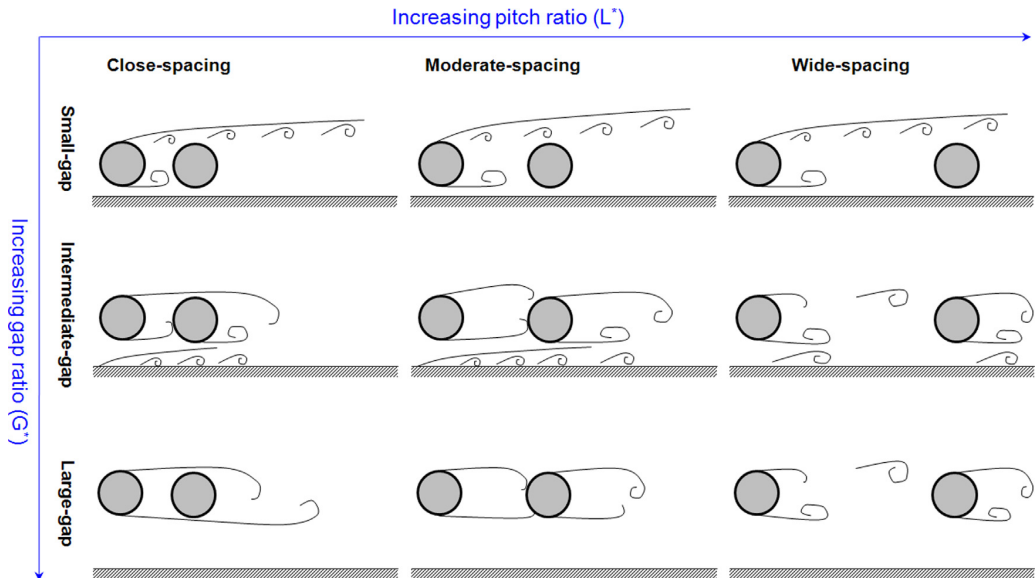


Figure 4.8. Schematic overview over flow patterns for tandem circular cylinders in the vicinity of a plane wall, with respect to  $L/D$  and  $G/D$ .  $Re = 6.3 \times 10^3$ . The categorization is based on PIV measurements (taken from Wang et al. (2015)).

It is, however, difficult to categorize the combined influences of  $L/D$  and  $G/D$ , because both cover a wide range of values, causing dramatic changes in the flow patterns. However, it is possible to identify the limiting cases, where previous well known theories can be applied, and discrepancies recognized. This approach is used as the idea for the present study. A detailed numerical investigation of the flow around tandem cylinders at several combinations of  $L/D$  and  $G/D$ , including the combinations that approach the limiting cases, is presented in Chapter 10.

According to Zhao and Yiu (2006), the influence of the downstream cylinder on the flow around the upstream cylinder in tandem arrangement in an infinite fluid, becomes negligible for large  $L/D$ . The flow around the upstream cylinder in a wide spaced tandem arrangement in the vicinity of a wall can thus be compared to the flow around a single cylinder near a plane wall. On the other hand, analysis of the flow around a single cylinder close to a wall (Bearman and Zdravkovich, 1978) shows that the influence of the wall diminishes as  $G/D$  increases, and becomes negligible for  $G/D > 2$ . The flow around tandem circular cylinders, with a relatively large distance from the plane wall, can be compared to the tandem cylinders in an infinite fluid. Ultimately, the behavior of the flow around the upstream cylinder in tandem arrangement close to a plane wall, with large  $L/D$  and  $G/D$ , approaches the case of a single cylinder in an infinite fluid and uniform incoming flow. An overview of the combinations of  $L/D$  and  $G/D$ , including the limiting cases, is presented in Figure 4.9.

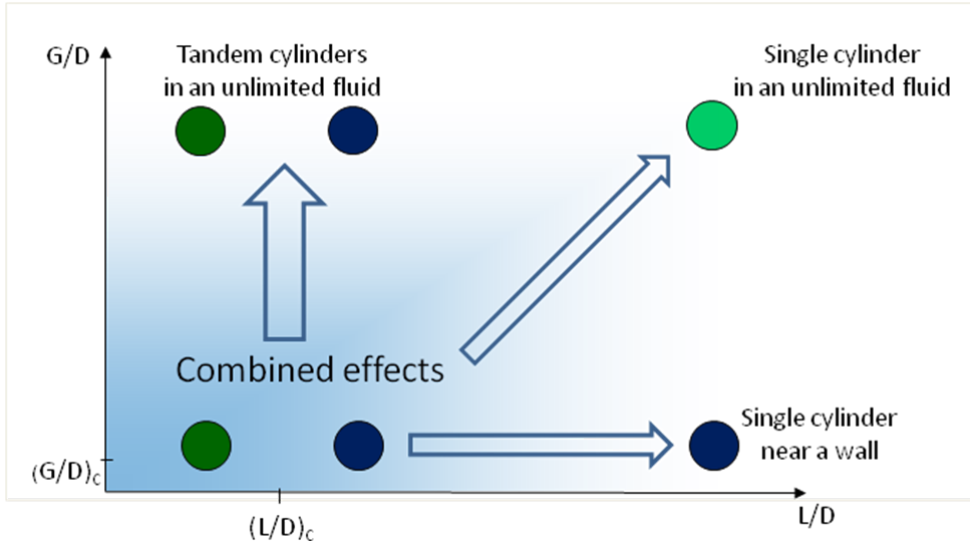


Figure 4.9. Schematic overview of the combinations of  $L/D$  and  $G/D$ , including the limiting cases (present study).



## References

Bearman, P. W., Zdravkovich, M. M. (1978) Flow around a circular cylinder near a plane boundary. *Journal of Fluid Mechanics*, 89, 33-47.

Bhattacharyya, S., Dhinakaran, S. (2008) Vortex shedding in shear flow past tandem square cylinders in the vicinity of a plane wall. *Journal of Fluids and Structures*, 24,400-417.

Harichandan, A. B., Roy, B. (2012) Numerical investigation of flow past single and tandem cylindrical bodies in the vicinity of a plane wall. *Journal of Fluids and Structures*, 33, 19-43.

Hiwada, M., Mabuchi, I., Yanagihara, I. (1982) Fluid flow and heat transfer around two circular cylinders. *Bulletin of JSME*, 25, 1737-1745.

Igarashi, T. (1981) Characteristics of the flow around two circular cylinders arranged in tandem (1<sup>st</sup> report). *Bulletin of the JSME*, 24, 232-331.

Igarashi, T. (1984) Characteristics of the flow around two circular cylinders arranged in tandem (2<sup>nd</sup> report, unique phenomenon at small spacing). *Bulletin of the JSME*, 27, 2380-2387.

Ljungkrona, L., Norberg, C. H., Sunden, B. (1991) Free-stream turbulence and tube spacing effects on surface pressure fluctuations for two tubes in an in-line arrangement. *Journal of Fluids and Structures*, 5:701-727.

Ljungkrona, L., Sunden, B. (1993) Flow visualization and surface pressure measurement on two tubes in an inline arrangement. *Experimental Thermal and Fluid Science*, 6, 15-27.

Sumner, D. (2010) Two circular cylinders in cross-flow: A review. *Journal of Fluids and Structures*, 26, 849-899.

Wang, X. K., Zhang, J.-X., Hao, Z., Zhou, B., Tan, S. K. (2015) Influence of wall proximity on flow around two tandem circular cylinders. *Ocean Engineering*, 94, 36-50.

Zdravkovich M. M. (1977) Review of flow interference between two circular cylinders in various arrangements. *ASME Journal of Fluids Engineering*, 99, 618-633.

Zdravkovich, M. M. (1987) The effects of interference between circular cylinders in cross flow. *Journal of Fluids and Structures*, 1, 239-261.

Zhou, W., Yiu, M. W. (2006) Flow structure, momentum and heat transport in a two-tandem-cylinder wake. *Journal of Fluid Mechanics*, 548, 17-48.

## Chapter 5

### Computational method

#### *5.1. Modelling of turbulent flows*

The theory of ideal (inviscid) fluid is well developed and applicable in some cases of real flow. However, it reaches its limits when applied to the flow around bluff bodies, where generation of vorticity, flow separation and viscous forces are of importance. Furthermore, offshore structures are exposed to high Reynolds numbers. The wakes and the boundary layers are mostly turbulent, and thus unsteady, three-dimensional and characterised by high vorticity.

Traditionally, such complex flow was investigated experimentally, requiring very precise and detailed measurements, often very costly and technically challenging. Numerical methods are often employed to complement or compensate the experiments. Under the broad topic of Computational Fluid Dynamics, covering various methods for solving of the partial differential equations, there are several classes of turbulence models. Detailed description of the approaches to turbulence modelling is given in Ferziger and Peric (2002). A comprehensive overview over various aspects of the numerical models, such as discretization method, interpolation and differentiation schemes and approaches to grid generation can be found in Patankar (1980), Versteeg and Malalasekera (1995) as well as in Ferziger and Peric (2002). A short overview over the three main approaches is given below.

Direct Numerical Simulations (DNS) offer the most accurate and conceptually the simplest approach to solve the Navier-Stokes equations. Using no approximations, DNS resolve flow structures of all sizes, i.e. all turbulence length scales. The error is controllable, originating only from the numerical discretization. Such a valuable tool comes with a cost: a huge number of degrees of freedom. Even though the development of the numerical techniques and the computational resources progress at increasing rate, the high demands of DNS still classify it as a research tool, not as an engineering tool.

A reduction in the number of grid points is possible by use of LES. At large scales, it behaves as a type of DNS, yielding precise instantaneous and statistical data about the three-dimensional flow.

Reynolds-Averaged Navier-Stokes equations (RANS) are often the answer to the needs of engineering today: quick and efficient solutions, offering a few quantitative properties of the turbulent flow. In RANS, all of the unsteadiness is regarded as part of the turbulence, yielding time-averaged equations of motion. Using various turbulence models, RANS offers good engineering approximations in various Re ranges. Recently, various hybrid models, for example unsteady RANS and Delayed Detached Eddy Simulations (DDES), are developed to utilize the better capabilities of the models and save computation time. An overview over the hybrid models' properties is given by Sagaut (2006). However, as stated by Ferziger and Peric (2002), one has to bear in mind that the numerical results are always approximate. The choice of the appropriate turbulence model can be challenging and the use has to be justified through the model's limitations, accuracy and applicability to the targeted flow types.

## ***5.2. LES with Smagorinsky subgrid scale model***

The development of LES started in the 1960s, with the introduction of the Smagorinsky subgrid scale closure (Smagorinsky, 1963; Lilly, 1967). It came to early use in the meteorological publications in the 1970s, but the applicability of this method became obvious around 2000, due to the development of the computational resources (Lesieur et al., 2005). Today, it is incorporated in commercially available fluid dynamics codes. LES has an important role in aerodynamics research, in combustion and geophysical sciences. Applied to hydrodynamics, LES provides a powerful tool for distinguishing the turbulent vortical structures and precise determination of the viscous separation points. A comprehensive overview over LES for incompressible and compressible fluids is given by Lesieur et al. (2005), while Sagaut (2006) focus on incompressible flow.

The large scale motions generally contain much more energy than the small scale motions. The conserved properties are thus transported much more effectively by the large scale motions, demanding their accurate prediction. This is achieved in LES, where the motions larger than the cut-off scale  $\Delta$  are explicitly calculated, while the subgrid scale motions are filtered out and modelled. Details about the filtering operation can be found in Pope (2000).

For incompressible fluid, the flow is governed by conservation of mass and momentum. Further, by assuming Newtonian fluid and uniform viscosity, and applying low-pass filtering, the Navier-Stokes equations can be written as:

$$\frac{\partial \bar{u}_i}{\partial x_i} = 0 \quad (5.1)$$

$$\frac{\partial \bar{u}_i}{\partial t} + \frac{\partial (\bar{u}_i \bar{u}_j)}{\partial x_j} = -\frac{1}{\rho} \frac{\partial \bar{p}}{\partial x_i} + \nu \frac{\partial}{\partial x_j} \left( \frac{\partial \bar{u}_i}{\partial x_j} + \frac{\partial \bar{u}_j}{\partial x_i} \right) \quad (5.2)$$

where  $u_i$ ,  $i = 1, 2, 3$ , is the filtered velocity component in the x-, y- and z- direction respectively,  $x_i$  is assigned to the respective directions and  $p$  the filtered pressure. The nonlinear filtered advection can be written as:

$$\overline{u_i u_j} = \bar{u}_i \bar{u}_j + \tau_{ij} \quad (5.3)$$

where  $\tau_{ij}$  is the non-resolvable subgrid stress, transforming Equation (5.2) to:

$$\frac{\partial \bar{u}_i}{\partial t} + \frac{\partial (\bar{u}_i \bar{u}_j)}{\partial x_j} = -\frac{1}{\rho} \frac{\partial \bar{p}}{\partial x_i} + 2\nu \frac{\partial \bar{S}_{ij}}{\partial x_j} - \frac{\partial \tau_{ij}}{\partial x_j} \quad (5.4)$$

Here  $S_{ij}$  is the large scale strain tensor, defined as:

$$\bar{S}_{ij} = \frac{1}{2} \left( \frac{\partial \bar{u}_i}{\partial x_j} + \frac{\partial \bar{u}_j}{\partial x_i} \right) \quad (5.5)$$

The sub-grid stress is most commonly modelled by the eddy-viscosity model proposed by Smagorinsky (1963). It assumes that the subgrid stresses behave in a similar manner as the large scale strain:

$$\tau_{ij} - \frac{1}{3} \delta_{ij} \tau_{kk} = -2\nu_t \bar{S}_{ij} \quad (5.6)$$

where  $\delta_{ij}$  is the Kronecker delta, and  $\nu_t$  is the subgrid scale eddy viscosity.  $\nu_t$  is assumed to be proportional to the subgrid scale characteristic length  $l$  and the strain rate tensor, given as:

$$\nu_t = l^2 \left| \bar{S}_{ij} \right| \quad (5.7)$$

$$l = C_s \bar{\Delta} = C_s (\Delta x \Delta y \Delta z)^{1/3} \quad (5.8)$$

$$\left| \bar{S}_{ij} \right| = \sqrt{2 \bar{S}_{ij} \bar{S}_{ij}} \quad (5.9)$$

Here  $C_s$  is the Smagorinsky's constant. For isotropic turbulence  $C_s \approx 0.18$  (Lilly, 1967), and in the present study it is set to the commonly used value  $C_s = 0.2$ .

### **5.3. *OpenFOAM computational package***

All simulations in the present study were performed using OpenFOAM, an open source computational package. Containing over 80 solvers, its field of application extends to incompressible and compressible fluid dynamics, combustion, fluid-structure interaction etc. Within turbulence modelling, it contains solvers covering all three general approaches.

OpenFOAM is a finite volume solver (for details about the finite volume method, see Versteeg and Malalasekera, 1995). The flow variables are defined on a collocated grid with possibility of use of structured and unstructured polyhedral grids with non-equidistant cell spacing. In the present study, body-fitted, structured hexahedron meshes are used for all cases. The details about the meshes, the procedure of mesh refinement and the resolution requirements are given in Chapters 6 – 10 for the specific simulations. The chosen discretization schemes, with discussion of their influence, are given in Chapter 7. The pressure-velocity coupling is done by the Pressure Implicit with Splitting of Operators (PISO) algorithm. Details of the procedure are given by Versteeg and Malalasekera (1995).

Message Passing Interface (MPI) is utilised for parallel computing, making it suitable for large, massively parallelized simulations. Using the Preconditioned Conjugate Gradient method (PCG) for solving of the discretized equations, the code scalability is nearly ideal up to 200-300 MPI processes (Robertson et al., 2015). Tested on the HPC supercomputer Vilje ([www.hpc.ntnu.no](http://www.hpc.ntnu.no)) on several benchmark cases, the scalability has proven to be good up to  $10^3$  parallel processes. In the present study, the supercomputer Vilje is used for parallel simulations on up to 512 processors.

## ***References***

Ferziger, J. H., Peric, M. (2002) *Computational Methods for Fluid Dynamics*. 3rd Edition. Springer-Verlag, Berlin, Germany.

Lesieur, M., Metais, O., Comte, P. (2005) *Large-Eddy Simulations of Turbulence*. Cambridge University Press, New York, NY, USA.

Lilly, D. K. (1967) The representation of small-scale turbulence in numerical simulation experiments. *Proceedings of IBM Scientific Computing Symposium on Environmental Sciences*, 320-1951, 195-210.

Patankar, S. V. (1980) Numerical Heat Transfer and Fluid Flow. *Hemisphere Publishing Series on Computational Methods in Mechanics and Thermal Science*, USA.

Pope, S. B. (2000) *Turbulent Flows*. Cambridge University Press, New York, NY, USA.

Robertson, E., Choudhury, V., Bhushan, S., Walters, D. K. (2015) Validation of OpenFOAM numerical methods and turbulence models for incompressible bluff body flows. *Computers and Fluids*, 123, 122-145.

Sagaut, P. (2006) *Large Eddy Simulation for Incompressible Flows (Third edition)*. Springer-Verlag, Berlin, Germany.

Smagorinsky, J. (1963) General circulation experiments with the primitive equations. *Monthly Weather Review*, 91-3, 99-164.

Versteeg, H. K., Malalasekera, W. (1995) An Introduction to Computational Fluid Dynamics. The Finite Volume Method. *Longman Scientific & Technical*, Essex, UK.



## **Chapter 6**

# **Large Eddy Simulations of three-dimensional flow around a pipeline in a uniform current**

Mia Prsic<sup>1</sup>, Muk Chen Ong<sup>1,2</sup>, Bjørnar Pettersen<sup>1</sup>, Dag Myrhaug<sup>1</sup>

<sup>1</sup>Department of Marine Technology,  
Norwegian University of Science and Technology, NO-7491 Trondheim, Norway

<sup>2</sup>Norwegian Marine Technology Research Institute (MARINTEK),  
NO-7450 Trondheim, Norway

Paper 1: Not included due to copyright.





## Chapter 7

# Large Eddy Simulations of flow around a smooth circular cylinder in a uniform current in the subcritical flow regime

Mia Abrahamsen Prsic <sup>a,\*</sup>, Muk Chen Ong <sup>b</sup>, Bjørnar Pettersen <sup>a</sup>, Dag Myrhaug <sup>a</sup>

<sup>a</sup> Department of Marine Technology, Norwegian University of Science and Technology, NO-7491 Trondheim, Norway

<sup>b</sup> Norwegian Marine Technology Research Institute (MARINTEK), NO-7450 Trondheim, Norway

### *Abstract*

Three-dimensional flow around a circular cylinder in a steady, uniform current at subcritical Reynolds numbers ( $Re$ ) is investigated. The flow is simulated using Large Eddy Simulations (LES) with Smagorinsky subgrid scale model. Influences of various numerical parameters are investigated through the statistical values of the drag and the lift coefficients, Strouhal number, pressure distribution and separation angles, as well as through the flow field in the cylinder near wake.

The main purpose of the paper is to study the flow around a circular cylinder at  $Re=13100$ , which is chosen due to its applicability to the flow around cylindrical offshore structures in operational conditions, and because it belongs to a not thoroughly studied  $Re$  range. However, first the flow around a cylinder in the free stream at  $Re=3900$  is investigated and the results are compared with numerous published results for validation of the chosen LES model. For the higher  $Re$ , the results are compared with the published experimental data and the numerical simulations for the similar flow regime. The chosen LES performs well. The results are in reasonably

good agreement with previous studies and are discussed through standard hydrodynamic parameters and details of the flow around the cylinder and in the wake.

Keywords: circular cylinder; Large Eddy Simulations; Smagorinsky turbulence model; wake flow; subcritical Re.

## 7.1. Introduction

Many offshore structures contain elements with cylindrical shape, such as jacket, jackup and tension-leg platforms, marine pipelines and bundles of marine risers. In the last 30 years, there has been a large increase in the use of such structures. Marine pipelines offer a sustainable and efficient way of oil and gas transportation. However, exposure to current and waves can cause the hazard of oil leakage. For safety issues it is important to broaden the understanding of the flow fields around such objects as well as the hydrodynamic loads exerted on them.

Pipelines at intermediate water depths are subjected to currents plus waves causing large variations in the velocities and thereby Reynolds number ( $Re = U_c D / \nu$ , where  $U_c$  is the free stream velocity,  $D$  is the diameter of the cylinder and  $\nu$  is the kinematic viscosity of the fluid), most often appearing in the range from  $10^3$  to  $10^7$ . It is therefore important to understand the flow around the circular cylinder in the actual Re range. In the present study, the moderate  $Re = 13100$  is chosen, corresponding to standard operational conditions of marine pipelines and risers. Most of the published VIV (Vortex Induced Vibrations) experiments belong to the Re range between 500 and 60000 (Diana et al., 2008), comparable to the present Re. Zhang and Dalton (1996) performed Large Eddy Simulations (LES) in order to investigate VIV of a circular cylinder in steady flow for  $Re = 13000$ , very close to the Re targeted here. Two-dimensional (2D) simulations were performed. Even though the flow is turbulent and thus three-dimensional (3D), the test case presented for a steady circular cylinder provides reasonable comparison with the experimental results, leading to the conclusion that LES is a promising tool for such simulations. However, VIV studies would benefit from more accurate and thorough investigation of the steady state flow situation, as presented in this paper.

This study focuses on 3D modelling of the flow around a smooth circular cylinder in a steady current in the subcritical flow regime ( $Re = 13100$ ). Validation of the code is done by comparing the results for the benchmark case of the flow around a

circular cylinder in the subcritical flow regime at  $Re = 3900$  with numerous published experimental and numerical results. For the  $Re = 13100$  case, details of the flow around, and in the near wake of the cylinder are analysed with respect to various numerical parameters, such as mesh resolution, time-step and computational domain size. The limitations of the measuring equipment used in some published experiments lead to difficulties in capturing the details of the flow, especially in the near wake. Therefore the present paper also focuses on describing the flow near the body surface and in the cylinder near wake.

Recently published numerical results are mainly based on LES. Breuer (1998 a, b) made a detailed analysis of the influence of the subgrid scale models, the grid resolution and the discretization schemes on the quality of the LES results. Tremblay et al. (2002) carried out a series of LES and compared them with the results of Direct Numerical Simulations (DNS). Wissink and Rodi (2008) used DNS and presented the details of the flow field in the near wake of a circular cylinder at  $Re = 3300$ . Parnaudeau et al. (2008) focused on the comparison of their LES results with the experimental results obtained by Particle Image Velocimetry (PIV). Krajnovic (2011) used LES with Smagorinsky subgrid scale model to simulate the flow around a vertical cylinder at  $Re = 20000$ . Lysenko et al. (2012) performed LES with standard Smagorinsky and k-equation eddy viscosity model for the compressible fluid at  $Re = 3900$  and low Mach number. Based on the previously mentioned research, LES is chosen as a promising numerical tool for simulating the flow behind a bluff body. In this paper, results are compared and discussed through the hydrodynamic quantities, such as drag and lift coefficients, Strouhal number, pressure and velocity distribution around the cylinder, and flow field in the near wake of the cylinder.

Experimental data for the flow around a fixed circular cylinder is available mostly for either very low or very high  $Re$  flows. Early measurements are documented by Linke (1931) and Thom (1928), mainly discussing the pressure distribution around the cylinder measured in a wind tunnel. Roshko (1961) focused on  $Re$  from  $10^6$  to  $10^7$ , as well as collecting and analysing data from many previous measurements considering subcritical  $Re$ . Schewe (1983) carried out a series of experiments in a pressurized wind tunnel, from subcritical to transcritical flow with  $Re$  from  $2.3 * 10^4$  to  $7.1 * 10^6$ . Cantwell and Coles (1983) studied experimentally the near wake flow field of a circular cylinder at  $Re = 1.4 * 10^5$ . Norberg (1994) focused on investigating the Strouhal number and the base suction coefficient behind the cylinder at  $Re$  between 50 and  $4 * 10^4$ . More experimental data was obtained by hot-wire and x-ray probe measurements of the near wake flow behind the circular cylinder by Ong and Wallace (1996) at  $Re = 3900$ .

The numerical research of the flow with comparable Re is limited, while the higher Re cases are studied in several publications. Fang and Han (2011) made a short discussion of the numerical results for the flow at three different moderate Re ( $5.6 * 10^3$ ,  $2.8 * 10^4$  and  $1.1 * 10^5$ ); Ouvrard et al. (2008) published hybrid RANS/LES data for  $Re = 1.4 * 10^5$ ; Breuer (2000) explored the influence of the various turbulence closure schemes and mesh refinements on the LES results for  $Re = 1.4 * 10^5$ ; Vaz et al. (2007) explored the influences of the numerical parameters and the different turbulence models in 2D and 3D simulations at  $Re = 9 * 10^4$  and  $5 * 10^6$ . In the higher Re range, Catalano et al. (2003) presented LES results with wall stress model for  $Re = 5 * 10^5$  and  $10^6$ ; Ong et al. (2009) used 2D Unsteady Reynolds-Averaged Navier-Stokes (URANS) equations with a  $k - \epsilon$  turbulence model for Re in the range  $10^6$  to  $3.6 * 10^6$ ; Lin et al. (2011) also used the  $k - \epsilon$  turbulence model to explore the influence of various advection schemes on the drag coefficient for  $Re = 10^6$ .

In this paper, a short overview of the chosen numerical method is presented in the following Section. Details of the numerical simulations are presented in Section 7.3. The results are discussed in Section 7.4, including the analysis procedure, the validation study for the  $Re = 3900$  flow, the convergence study for the  $Re = 13100$  cases and the comparison with previously published results.

## 7.2. Numerical Method

A LES model is chosen due to its capability of modelling the moderate high Re flow and resolving the 3D bluff body flow in a less numerically costly manner than DNS. In a LES model, the large scale turbulence is simulated directly and the subgrid scale turbulence, which is assumed to behave more case independent, is modelled.

In order to simulate the flow, the incompressible Navier-Stokes equations need to be solved. In the filtered form, the continuity and the momentum equations, disregarding the commutation error, can be written as:

$$\frac{\partial \bar{u}_i}{\partial x_i} = 0 \quad (1)$$

$$\frac{\partial \bar{u}_i}{\partial t} + \frac{\partial (\bar{u}_i \bar{u}_j)}{\partial x_j} = \frac{-1}{\rho} \frac{\partial \bar{p}}{\partial x_i} + \nu \frac{\partial^2 \bar{u}_i}{\partial x_j^2} - \frac{\partial \tau_{ij}}{\partial x_j} \quad (2)$$

where  $u_{i,j}$ ,  $i, j = 1, 2, 3$  denotes the filtered velocity component in streamwise ( $x$ ),

crossflow ( $y$ ) and spanwise ( $z$ ) direction respectively, see Figure 2.  $x_i$  is assigned to the respective directions,  $\rho$  is the density of the fluid,  $p$  is the filtered pressure and  $\tau_{ij}$  represents the non-resolvable subgrid stress, given by:

$$\tau_{ij} = \overline{u_i u_j} - \overline{u_i} \overline{u_j} \quad (3)$$

The commonly used Smagorinsky subgrid scale model (Smagorinsky, 1963) is based on the Boussinesq approximation, assuming that the turbulence stresses behave in the same manner as the large scale strain rate tensor  $S_{ij}$  :

$$\tau_{ij} - \frac{1}{3} \delta_{ij} \tau_{kk} = -2\nu_t \overline{S_{ij}} \quad (4)$$

where  $\delta_{ij}$  denotes the Kronecker delta and  $\nu_t$  is the subgrid scale eddy viscosity. The strain rate tensor  $S_{ij}$  in the resolved field can be written as:

$$\overline{S_{ij}} = 0.5 \left( \frac{\partial \overline{u_i}}{\partial x_j} + \frac{\partial \overline{u_j}}{\partial x_i} \right) \quad (5)$$

The subgrid scale eddy viscosity  $\nu_t$  is a function of the strain rate tensor and the subgrid length  $l$

$$\nu_t = l^2 \left| \overline{S_{ij}} \right| \quad (6)$$

$$l = C_s \overline{\Delta} \quad (7)$$

$$\left| \overline{S_{ij}} \right| = \sqrt{2 \overline{S_{ij} S_{ij}}} \quad (8)$$

The filter width  $\Delta$  is correlated to the typical grid spacing by the cube root of the cell volume.  $C_s$  is the Smagorinsky constant with a value of 0.2 in the present study. More sophisticated subgrid scale models have been developed, such as the dynamic Smagorinsky model (Germano et al. (1991), Lilly (1992)) in which  $C_s$  becomes a so called dynamic constant, a local, time-dependent variable determined from the resolved velocity field.

Breuer (1998 a, 2000), Tremblay et al. (2002) and Lysenko et al. (2012) discussed the advantages and the differences of various subgrid scale models. Breuer (1998 a) analysed the simulations performed with the same numerical set-up, but without any subgrid scale model, with standard and with dynamic Smagorinsky model. He concluded that, in comparison to relatively large influence of the various discretization schemes, the subgrid scale models have a relatively small influence. While the simulation without any subgrid scale model showed the shortest

recirculation length, the results obtained with Smagorinsky and dynamic Smagorinsky models were close to each other and showed better agreement with experimental results. Standard Smagorinsky model yielded a 2.5% larger drag coefficient, 0.2% larger primary separation angle and 1.25% smaller secondary separation angle compared with the dynamic Smagorinsky model. Through comparison of several flow parameters, Lysenko et al. (2012) discussed the differences between the standard Smagorinsky and the dynamic k-equation eddy viscosity (TKE) model. They concluded that the results obtained with Smagorinsky model compared well with the experimental results by Lourenco and Shih (1993), while the TKE results compared better with the results of Parnaudeau et al. (2008). Lysenko et al. (2012) also calculated the one-dimensional energy spectra of simulations with Smagorinsky and TKE model. Both sets of data showed good agreement with experimental results of both Ong and Wallace (1996) and Parnaudeau et al. (2008). The spectra obtained by Smagorinsky model showed to be less dissipative than those obtained by TKE. Taking these results into account, it can be concluded that, even though the dynamic models are less rigid, a standard Smagorinsky model gives comparable quality of the results. It is also commonly used in the established cases for the flow around the circular cylinder for  $Re = 3900$ . For the sake of simplicity and comparability, a standard Smagorinsky model is chosen in this work.

All the simulations are performed using the open source code OpenFOAM, a computational fluid dynamics solver with extensive libraries for turbulence modelling. It is a finite volume code written in C++ using object-oriented techniques (OpenFOAM, 2011). Advantages of LES modelling in OpenFOAM can be explored through an example similar to the topic discussed in this paper, i. e. flow around a square cylinder, made by the code creators (Weller et al., 1998).

The PISO algorithm (Pressure Implicit with Splitting of Operators), described by Ferziger and Peric (2001), is used to solve the Navier-Stokes equations. A preconditioned conjugate and bi-conjugate method with diagonal incomplete-Cholesky (for symmetric) and diagonal incomplete-LU (for asymmetric matrices) are used for solving linear systems (OpenFOAM, 2011). For the time integration, an implicit, backward differencing method of second order is chosen, also used by Lysenko et al. (2012). Spatial schemes for the convective term approximations and inviscid terms are Gauss linear and Gauss limited linear. Those are central differencing schemes with a standard finite volume discretization of Gaussian integration which requires the interpolation of values from the cell centres to the face centres. All of the above schemes are of second order accuracy, which is, as summarized by Krajnovic (2011), the most common in engineering applications of LES. Discussion of the influences of

the various numerical methods can be found in Breuer (1998 b). He compared various discretization schemes for the convective terms, such as a combination of upwind and a central differencing scheme, a central differencing scheme of second and fourth order, a hybrid linear/parabolic scheme and a parabolic second order approximation. It was shown that the central differencing schemes offered the best agreement with the experiments. Even though the fourth order schemes yielded slightly better results, the variations between the central schemes of second and fourth order were much smaller than among other schemes. Therefore it is considered that the second order discretization schemes offer a good option for LES.

### 7.3. Computational model

The size of the 3D computational domain for the majority of the cases is  $32D * 16D * 4D$  (x, y, z). The centre of the cylinder (and the origin of the coordinate system) is placed  $8D$  from the inlet boundary,  $8D$  away from the top and the bottom boundaries and  $24D$  away from the outlet boundary (Figure 1). Simulations with both  $4D$  and  $8D$  spanwise (z) domain width are made for  $Re = 13100$  to study the effect of the spanwise length.

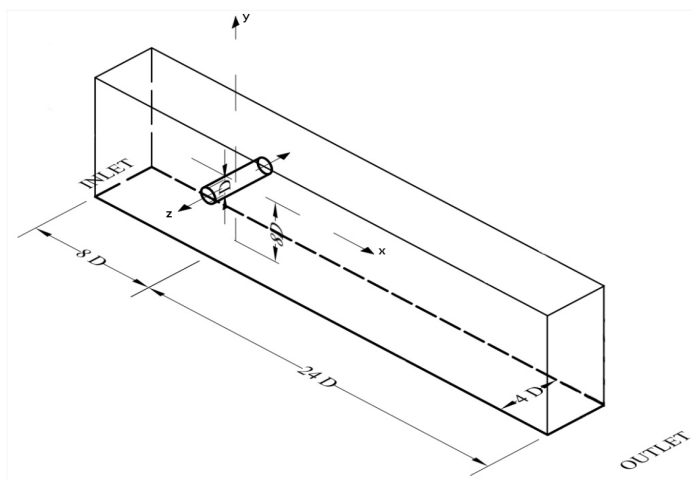


FIGURE 1: The computational domain.

For the simulations of the flow with  $Re = 3900$ , the domain size is chosen by comparison with the established standards for this benchmark case. Both Parnaudeau et



al. (2008) and Tremblay et al. (2002) extended their domains over the same area:  $20D$  in the streamwise ( $x$ ) and crossflow ( $y$ ) directions, while the centre of the cylinder was placed  $5D$  downstream from the inlet boundary. The spanwise length of the domains in the aforementioned papers was  $\pi D$ . Franke and Frank (2002) used a slightly larger domain extending over  $10D$  in front of the cylinder,  $20D$  behind and  $10D$  above and below the cylinder. Their domain also had a spanwise length of  $\pi D$ . Breuer (1998 b) used a circular domain with a radius of  $15D$  and  $\pi D$  spanwise length. Wissink and Rodi (2008) used a  $25D * 20D * 4D$  domain, Li (2011) used a smaller domain size of  $27D * 9D * 2.3D$ , while Heggernes (2005) used exactly the same domain size as chosen in the present paper. Considering the aforementioned dimensions, the chosen domain size is assumed to be sufficient to obtain results unaffected by the boundary conditions.

In the  $Re = 13100$  case, the same domain size is used. Since there is not many numerical simulations published at this  $Re$ , the domain size is compared with the higher  $Re$  simulations. Ong et al. (2009) simulated the flow at very high  $Re$ , using two-dimensional  $k-\epsilon$  URANS. Their domain spreaded over  $7D$  in front of, above and below the circular cylinder and  $20D$  behind the cylinder. Breuer (1998 b and 2000) used a cylindrical domain with a radius of  $15D$  and a somewhat smaller spanwise length of  $2D$  and  $\pi D$  for LES at both  $Re = 3900$  and  $140000$ . Fang and Han (2011) used a domain of  $28D * 8D * 10D$  for all their  $Re$ . Based on the fact that smaller domains have successfully been used for simulations of the flow at higher  $Re$ , the computational domain used in this work is considered to be sufficiently large.

In order to obtain results independent of the mesh, it is important to take shape, resolution and distribution of the elements into consideration. To avoid possible spurious oscillations and numerical instabilities, attention is paid to the smoothness of the transitions between adjacent mesh patches. In this case, a symmetric, body-fitted hexahedron mesh is divided into several zones. A small, O-shape zone of  $0.2D$  width (Zone 1) is created around the cylinder in order to provide easier control of the cell sizes in the immediate vicinity of the cylinder. A second zone of O-shape mesh (Zone 2) extends up to  $5D$  radially from the cylinder centre. The outermost part (Zone 3), between the outer edge of Zone 2 and the domain boundaries is filled with slightly radially stretched hexahedron elements. Finally, Zone 4 in the far wake of the cylinder consists of a coarser, rectangular mesh, slightly clustered towards the centre of the domain. Figure 2 presents the visualization of the entire domain, Zones 1- 4 and a more detailed view of Zones 1 and 2 near the cylinder. Meshes of the same distribution, i.e. the same shape of the elements in respective Zones, with different number of elements and mesh refinements are used in all the cases for both  $Re$ .

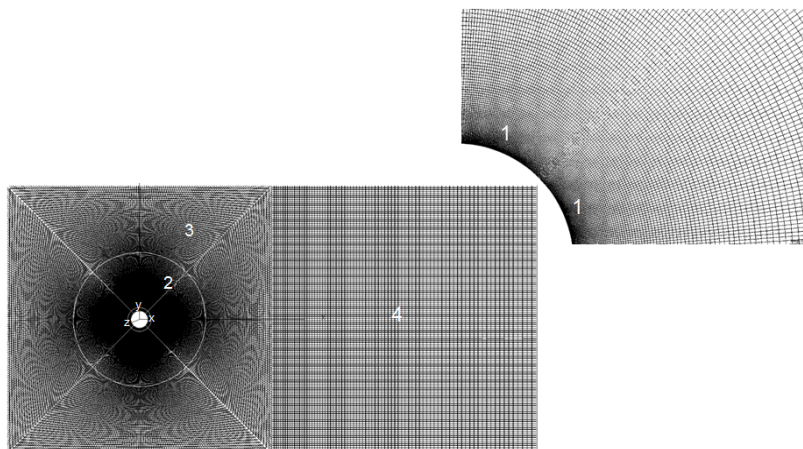


FIGURE 2: Visualization of the mesh – Zones 2, 3 and 4 and Zone 1 in the immediate vicinity of the cylinder. Zones and the coordinate system are shown.

The boundary conditions are kept the same throughout the entire study. At the inlet, a uniform and constant velocity is prescribed. At the outlet, the pressure and the normal gradient of the velocities are set to zero. The top, bottom and side boundaries are considered to be free-slip surfaces, utilizing a symmetry boundary condition, while a no-slip condition is applied on the cylinder surface. The influence of the boundary conditions is discussed in Section 7.4.

TABLE 1: Numerical set-up for the  $Re = 3900$  cases: the domain size is  $32D * 16D * 4D$ ; the number of elements spanwise is 150.

Case	Num. elem. (million)	Num. elem. circumf.	Boundary condition in the spanwise direction
3900_m1	5	340	free-slip
3900_m2	8	400	free-slip
3900_m3	11	480	free-slip
3900_m4	13.5	540	free-slip
3900_pbc	13.5	540	periodic

Five simulations are carried out at  $Re = 3900$ , with inlet velocity  $U_c = 0.39$  m/s. The dimensionless time-step  $\Delta t = 0.0008$  is chosen to keep the maximum Courant number below 0.6 (see Table 1, for other details of the simulations). The Courant number is defined as  $C = U_{abs} \Delta t / \Delta \delta$ , where  $U_{abs}$  is the magnitude of the velocity through the cell and  $\Delta \delta$  is the cell size in the direction of the velocity. In all the simulations the element size on the surface of the cylinder is kept the same and is chosen in such a manner that the maximum dimensionless wall distance  $\delta^+$  is kept

below 1. Here  $\delta^+$  is defined as  $\delta^+ = u_* \delta / \nu$ , where  $u_*$  denotes the friction velocity at the nearest wall, and  $\delta$  is the normal distance from the wall. The maximal values of dimensionless streamwise wall distance,  $x^+$ , are smaller than 2 for all simulations, in the cross-flow direction,  $y^+ < 4.5$  and in the spanwise direction,  $7 < z^+ < 26$ ;  $x^+$ ,  $y^+$  and  $z^+$  are defined according to Krajnovic (2011) as  $x^+ = u_* \xi / \nu$ ;  $y^+ = u_* \iota / \nu$ ;  $z^+ = u_* \zeta / \nu$ , where  $\xi$ ,  $\iota$  and  $\zeta$  are the distances from the wall in x, y and z direction, respectively.

TABLE 2: Numerical set-up for the Re = 13100 cases.

Case	Domain (*D)	Number elem. (million)	Num. elem. spanwise	Num. elem. circumf.	$\Delta t$ (s)
13100_m1	32 * 16 * 4	2	100	244	0.0001
13100_1	32 * 16 * 4	4.3	100	340	0.0001
13100_m2	32 * 16 * 4	7.7	100	480	0.0001
13100_m3	32 * 16 * 4	11	100	540	0.0001
13100_t2	32 * 16 * 4	4.3	100	340	0.0002
13100_t3	32 * 16 * 4	4.3	100	340	0.0004
13100_sm	32 * 16 * 4	6.5	150	340	0.0001
13100_sl	32 * 16 * 8	8.6	200	340	0.0001

The difference between four of the simulations for Re = 3900 is the mesh refinement, especially in the near wake of the cylinder (Zones 1 and 2). The mesh refinement is performed radially and along the circumference of the cylinder in order to keep the shape and ratios of the elements as constant as possible. The 3900\_m4 case is performed with the finest mesh of 13.5 million elements. In the 3900\_m3 case, the 3D computational domain contains approximately 11 million elements; in the 3900\_m2 case, 8 million elements are used; and in the 3900\_m1 case, 5 million elements are distributed over the computational domain. The fifth simulation, the 3900\_pbc case, is performed with the finest mesh, analogous to the 3900\_m4 case, but with periodic boundary condition on the side boundaries, in order to check the influence of the boundary condition on the results.

Eight simulations are carried out for the flow around the circular cylinder at Re = 13100 in order to explore the influence of the mesh refinement in the near wake zone, the domain size, the time-step and the spanwise mesh resolution (details are presented in Table 2). The results are discussed in the following Section.

## 7.4. Results and discussion

### 7.4.1. Analysis procedure

The details of the flow around the circular cylinder are presented with emphasis on the near-wake flow. The overall features of the flow are represented by the drag and lift coefficients and the Strouhal number. The details of the near-wake flow are explored through the velocity field in the wake, the recirculation length, the pressure coefficient distribution around the cylinder and the separation angles. Here, the drag coefficient is defined as  $C_d = F_d / (0.5\rho U_c^2 A)$ , where  $F_d$  is the drag force obtained by integrating over the cylinder surface.  $A$  is the frontal area of the cylinder. The lift coefficient is  $C_l = F_l / (0.5\rho U_c^2 A)$ , where  $F_l$  is the integrated lift force. The pressure coefficient is  $C_p = (p' - p_\infty) / (0.5\rho U_c^2)$  where  $p'$  is the pressure at the sampling point and  $p_\infty$  is the pressure in the undisturbed flow. Time-averaging is made for a fully developed flow. The  $Re = 3900$  cases are averaged over more than 50 vortex shedding cycles and the  $Re = 13100$  cases over between 130 and 190 vortex shedding cycles.

As mentioned before, a free-slip boundary condition is assigned to the lateral planes of the domain. It has been successfully used by Krajnovic (2011), but it implies a non-physical requirement of zero normal velocity at the boundary plane. Therefore it is presumed that a certain layer of the fluid in the vicinity of the lateral boundaries is influenced by this boundary condition and is thus excluded from the analysis. To check the influence of the boundary condition, the time-averages of the wall-normal velocity component are calculated at several cross sections in the cylinder wake,  $0.53D$ ,  $0.7D$ ,  $1D$  and  $2D$  from the cylinder centreline in the  $(x, y)$  plane. The absolute values of the time-averaged wall-normal velocities are further averaged along the cylinder, covering various spans from the cylinder centre towards the boundaries. The time-averaged wall-normal velocity is expected to be nearly constant and approaching zero along the boundary-unaaffected part of the cylinder. Therefore the flow is considered affected as soon as the space-averaged values begin to change when averaged over wider spans. Figure 3 shows the time-averaged wall-normal velocity component for the 13100\_1 case, indicating that the influence of the boundary condition is strongest in the immediate wake of the cylinder ( $x/D = 0.53$ ). It appears as an increase in the absolute value of the wall-normal velocity component in the vicinity of the boundaries (close to  $z/D = 0$  and  $4$ ). The analysis has been made for all  $Re = 3900$  and  $Re = 13100$  cases. It is concluded that the time- and space-averaged wall-normal velocities remain nearly constant for the central  $2.4D$  part of the  $4D$  long cylinder and for the  $6.4D$  of the  $8D$  long cylinder (the 13100\_sl case). Therefore, in the following analyses, space-averaging is made only along the central  $2.4D$  and  $6.4D$  of the cylinder.

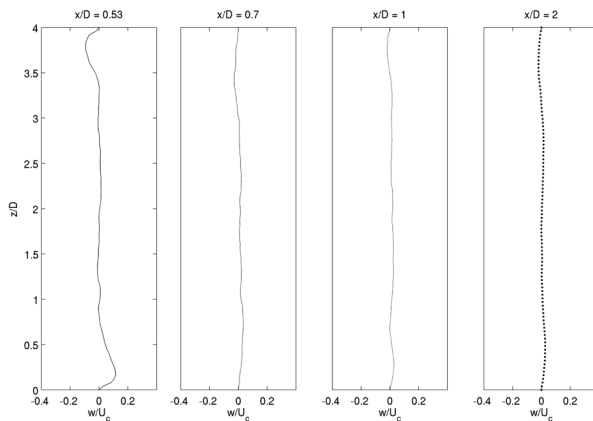


FIGURE 3: Time-averaged wall-normal velocity component ( $w$ ) at four cross sections in the cylinder wake, 13100\_1 case.

The influence of the alternative choice for boundary condition on the lateral boundaries is checked through two simulations for  $Re = 3900$ . While the 3900\_m4 case is performed with the free-slip boundary condition, the 3900\_pbc case is simulated using all numerical parameters the same except the periodic boundary condition on the lateral boundaries. The results are compared in Figure 4, through the time- and space-averaged streamwise velocity component, averaged in the above described manner for both simulations. Slight differences can be noticed between 3D and 6D in the cylinder wake, but they do not exceed 2%. It is therefore concluded that the free-slip boundary condition can be used for this kind of simulations, as long as attention is paid on the space-averaging.

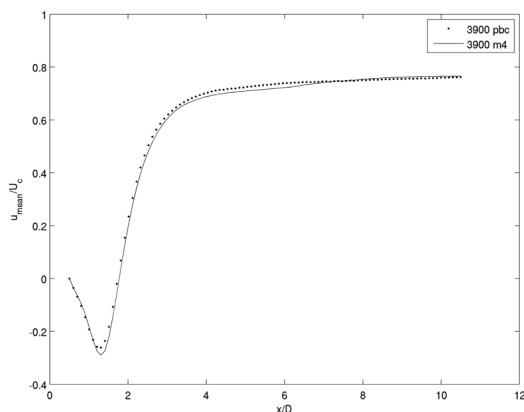


FIGURE 4: Time- and space-averaged streamwise velocity component ( $u$ ) profile in the cylinder wake, in the  $(x, z)$  plane,  $y = 0$  for the 3900\_m4 case with the free-slip boundary condition and 3900\_pbc case with the periodic boundary condition.

## 7.4.2. Validation study - Reynolds number 3900

### 7.4.2.1. Hydrodynamic quantities

A grid convergence study is performed for the flow at  $Re = 3900$  through four simulations, varying the number of the elements and by comparing with numerical results by Breuer (1998 a), Franke and Frank (2002), Tremblay et al. (2002) and Lysenko et al. (2012) and experimental results by Lourenco and Shih (1993), Ong and Wallace (1996) and Parnaudeau et al. (2008). The Strouhal number ( $St = fD/U_c$ , where  $f$  is the vortex shedding frequency) is obtained from the power spectra of the lift force fluctuations, following the procedure of Schewe (1983). As seen from Table 3,  $St = 0.2152$  for the two cases with the finest mesh (3900\_m4 and 3900\_m3), and that compares well with the results of the aforementioned authors. Figure 5 shows  $C_d$  (time- and space-averaged values of the drag coefficient) and  $C_{l\ rms}$  (the root-mean-square (rms) value of the lift coefficient). The results in Figure 5 are given for simulations using 5, 8, 11 and 13 million elements, respectively. Conclusions drawn from Figure 5, Table 3 and the good agreement of  $C_d$  and  $C_{l\ rms}$  of the 3900\_m4 case with the previously published results (Table 4) suggest that the convergence is approached.

TABLE 3: Mean flow parameters for the  $Re = 3900$  cases.

Case	$C_d$	$C_{l\ rms}$	St
3900_m1	1.2365	0.4490	0.2054
3900_m2	1.1483	0.2887	0.1956
3900_m3	1.0859	0.2163	0.2152
3900_m4	1.0784	0.1954	0.2152
3900_pbc	1.1102	0.2596	0.2152

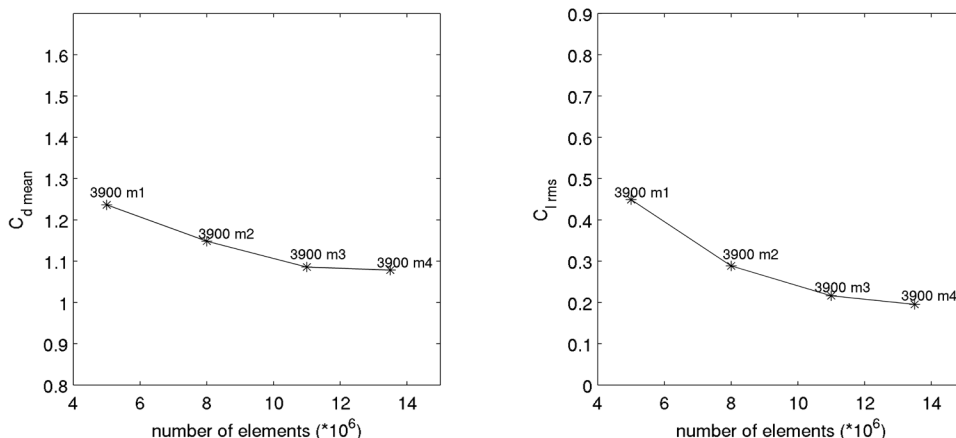


FIGURE 5:  $C_d$  and  $C_{l\ rms}$  versus the number of elements for  $Re = 3900$ . Cases: 3900\_m1; 3900\_m2; 3900\_m3; and 3900\_m4.

### 7.4.2.2. Flow in the cylinder wake

Further validation is made by analysing the details of the flow in the cylinder wake and comparing with previously published data. Several cross sections perpendicular to the cylinder axis are considered and the data is averaged in the spanwise ( $z$ ) direction and in time. The velocity field is sampled along the  $x$ -axis (see Figure 1) and over a vertical cross section parallel to the  $y$ -axis. In both cases, the velocity field is sampled over cross sections distributed evenly along the cylinder axis, excluding a length of  $0.8D$  from each end of the cylinder. For sampling along the  $x$ -axis, the sampling sections are located at the cylinder centreline, i. e. in the  $(x, z)$  plane starting from  $x/D = 0.5$ ,  $y/D = 0$  and covering eight diameters downstream. Figure 6 shows the time- and space-averaged values of the streamwise velocity component ( $u$ ) in the  $(x, z)$  symmetry plane of the cylinder wake for all four simulations. The 3900\_m4 and 3900\_m3 cases obtain the velocity minima positioned farthest away

from the cylinder, while 3900\_m1 and 3900\_m2 have shorter wake disturbances (see the region between  $x/D = 0.5$  and 3 in Figure 6). Even though the 3900\_m4 case obtains a somewhat less pronounced minimum, the velocity profiles in the wake, especially at  $x/D > 1.5$  show the smallest relative differences.

The mean dimensionless recirculation length ( $L_r$ ) is defined as the distance between the base of the cylinder and where the sign of the centreline mean streamwise velocity component changes, divided by  $D$ . For the coarsest mesh,  $L_r$  obtains value of 0.96, corresponding to 25% shorter recirculation length than for the finest mesh. As previously concluded from Figure 6, the finer meshes yield longer wakes, leading to  $L_r = 1.27$  for the 3900\_m4 case. The  $L_r$  difference for the two finest meshes is 6%.

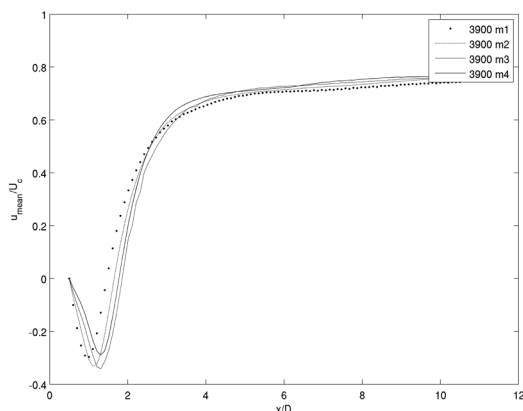


FIGURE 6: Time- and space-averaged streamwise velocity component ( $u$ ) profile in the cylinder wake, in the  $(x, z)$  plane at  $y/D = 0$ .

In Figure 7 a and b, the results of the 3900\_m4 case are compared with previously published numerical and experimental results, generally showing good agreement. The present mean streamwise velocity profiles in the cylinder mid-plane (Figure 7 a) compare very well with the experimental results of Lourenco and Shih (1993) and Ong and Wallace (1996); in the near wake also with the DNS results by Tremblay et al. (2000). However the results show more discrepancy from the results by Parnaudeau et al. (2008) and Lysenko et al. (2012) obtained with a TKE subgrid scale model. Similar behaviour is noticed by Lysenko et al. (2012) who, through comparison of several flow parameters, concluded that LES with Smagorinsky model yields results in good agreement with the PIV results of Lourenco and Shih (1993), while the TKE model leads to better agreement with the experiments of Parnaudeau et al. (2008). Figure 7 b shows the mean streamwise velocity component in the vertical  $(y, z)$  plane



in the near wake of the cylinder. A characteristic V-shaped velocity profile is observed; and the results are in good agreement with the numerical results of Tremblay et al. (2000) and the experiments of Lourenco and Shih (1993).

TABLE 4: Hydrodynamic quantities – present and previous studies for  $Re = 3900$ .

Case	$C_d$	$C_{l_{rms}}$	St	$L_r$
3900_m4	1.0784	0.1954	0.2152	1.27
Schlichting (1979)	1.0000		0.205–0.212	
Lourenco and Shih (1994)	0.99		0.22	1.19
Ong and Wallace (1996)	0.98±0.05		0.21	
Breuer (1998 a), Smagorinsky dynamic Smagorinsky	1.099 1.071		0.215±0.005	1.115, 1.197
Tremblay et al. (2002)	1.14		0.21	1.04
Franke and Frank (2002)	[0.978 – 1.005]		0.21	1.35
Dong et al. (2006)			0.2	1.36–1.47
Parnaudeau et al. (2008) PIV LES			0.208±0.001	1.51
Lysenko et al. (2012) TKE and Smagorinsky	0.97 1.17		0.209 0.19	1.67 0.9

There are significant differences in published values for the mean recirculation length at  $Re = 3900$  (Table 4). Parnaudeau et al. (2008) presented a detailed discussion about the sensitivity of  $L_r$  with respect to the time averaging interval. The conclusion was that the fully converged value of  $L_r$  could not be obtained for less than 250 vortex shedding cycles. The uncertainty associated with shorter averaging periods was roughly estimated to  $\pm 12\%$  for averaging over 52 shedding periods (corresponding to the present averaging period for the  $Re = 3900$  cases) and  $\pm 6\%$  for averaging over 120 periods (roughly corresponding to the number of periods that the  $Re = 13100$  cases are averaged over). Norberg (1994) also reported on the sensitivity of the experimentally obtained  $L_r$  values to the spanwise length of the cylinder below  $60D$ , while Lysenko et al. (2012) discussed the differences obtained by using Smagorinsky and TKE subgrid scale model in LES.

In the present study,  $L_r = 1.27$  for the 3900\_m4 case is in good agreement with previous LES of Breuer (1998 a), Franke and Frank (2002) and Tremblay (2002). Compared with the PIV measurements, the conclusions are similar to those drawn from velocity profiles in the cylinder wake. The present  $L_r$  values correspond better to the results of Lourenco and Shih (1993) and Dong et al. (2006) than to those of Parnaudeau et al. (2008).

Having in mind that the  $\delta^+$  value, i. e. the size of the smallest element at the cylinder surface, the time-step, the domain size, the cylinder length and the spanwise grid resolution are kept constant, the sole influence of the grid is examined. Considering the good agreement with both numerical and experimental results, it is concluded that convergence is achieved for the 3900\_m4 case, and that the chosen numerical model is suitable for simulating the flow in the subcritical regime.

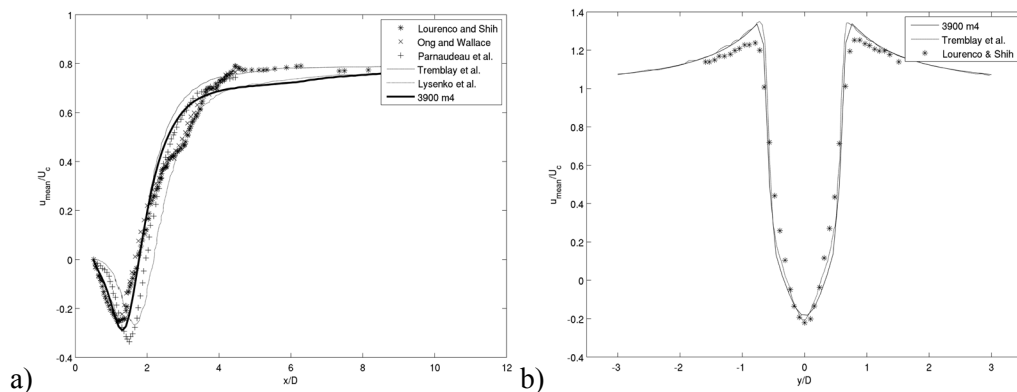


FIGURE 7: Time- and space-averaged streamwise velocity component ( $u$ ) profile in the cylinder wake.

a) in the  $(x, z)$  plane,  $y/D = 0$ . Experimental results by Lourenco and Shih (1993), Ong and Wallace (1996) and Parnaudeau et al. (2008), DNS simulation by Tremblay et al. (2000) and LES simulation by Lysenko et al. (2012), present study - 3900\_m4 case.

b) in the  $(y, z)$  plane,  $x/D = 1.06$ . Present study - 3900\_m4 case, DNS results by Tremblay et al. (2000), experimental results by Lourenco and Shih (1993).

### 7.4.3. Flow around the circular cylinder at $Re = 13100$

For the flow around the circular cylinder at  $Re = 13100$ , eight simulations are carried out. Similar to the previous cases, the overall mesh characteristics are unchanged for all the simulations; the mesh resolution at the cylinder surface is kept nearly constant with  $\delta^+ \leq 1$ ; and the boundary and the initial conditions are kept the same. Influences of several numerical parameters are investigated: the mesh refinement, the time-step, the domain width and the spanwise mesh resolution. The results are, after the convergence study, discussed through the integrated hydrodynamic quantities, the velocity profiles in the cylinder wake, the recirculation length, the pressure distribution and the behaviour of the flow separation.

### 7.4.3.1. Hydrodynamic quantities

In the grid convergence study, four cases: 13100\_m1, 13100\_1, 13100\_m2 and 13100\_m3 are simulated varying the mesh density, with special attention paid to the near wake (Zones 1 and 2, Figure 2) while keeping the  $\delta^+$  value nearly constant. The influence of the mesh refinement is first analysed through the values of  $C_d$ ,  $C_{1\text{rms}}$  and  $St$ . Table 5 shows  $C_d$  and  $C_{1\text{rms}}$  for the cases with varying mesh refinements. The mesh refinement from 7.6 million elements (13100\_m2 case) to 11 million elements (13100\_m3 case) results in less than 1% change of  $C_d$  and 6% change of  $C_{1\text{rms}}$ , while  $St$  obtains the same value for both simulations. This suggests that the finest mesh is sufficiently fine. To confirm that, further analysis of the mesh convergence study is presented in the following Section.

The influence of the time-step is also investigated through the  $C_d$ ,  $C_{1\text{rms}}$  and  $St$  values. The 13100\_1, 13100\_t2 and 13100\_t3 cases are simulated with the same mesh (corresponding to the 13100\_1 case), but by varying the time-step. Attention is paid to the Courant number, which mean value is always kept low and which maximum value (per mesh cell, per time-step) does not exceed 0.6. From Table 5, it is observed that the time-step variation does not have a strong influence on the results: the  $C_d$  variation is 1% between the cases with smallest and largest time-step, the  $C_{1\text{rms}}$  variation is 5% and the  $St$  variation 1.4%. The dimensionless time-step of  $0.001D/U_c$ , used in all the latter cases, is therefore considered to be sufficiently small.

### 7.4.3.2. Flow in the cylinder wake

Velocities are sampled over the cross sections coinciding with the x-axis (x, z plane) and at the vertical cross section in the near wake (y, z plane) – consistent with what is chosen in Section 7.4.2.2. The pressure and the velocities are also sampled at the cylinder surface in order to observe the variations of  $C_p$  and the separation angle. The data is averaged over time and space in the same manner as before.

By comparing the streamwise velocity profiles in the cylinder wake, sampled in the (x, z) plane,  $y/D = 0$  for the 13100\_m1, 13100\_1, 13100\_m2 and 13100\_m3 cases (Figure 8 a), it is found that the two simulations with the finest meshes give similar velocity values, while there are larger discrepancies for the 13100\_m1 and 13100\_1 cases. It can also be noticed that the finer meshes allow the cylinder wake to stretch farther in the wake region. That is supported by the fact that the coarsest mesh results in  $L_r = 0.57$ , while the other meshes yield larger values - 0.722 for the 13100\_1 and 13100\_m3 cases and a 6% longer  $L_r$  for the 13100\_m2 case than the 13100\_m3

case (see Figure 8 a). Similar effects are reported by Breuer (1998 b) and Tremblay et al. (2002); for the finer mesh cases, they describe farther propagating disturbances and better agreement with the experimental results (e. g. Lourenco and Shih, 1993).

TABLE 5: Mean flow parameters for the  $Re = 13100$  cases.

Case	$C_d$	$C_{l,rms}$	St
13100_1	1.3509	0.6236	0.2038
13100_m1	1.3703	0.6750	0.2069
13100_m2	1.3013	0.5105	0.2038
13100_m3	1.3132	0.5454	0.2038
13100_t2	1.3358	0.6001	0.2038
13100_t3	1.3364	0.5879	0.2009
13100_sm	1.3433	0.6257	0.1980
13100_sl	1.3517	0.5788	0.2038

A shorter wake, as simulated by the coarse mesh in the 13100\_m1 case, leads to smaller velocities in the part of the wake where other three simulations still successfully capture the recirculation flow. This behaviour is depicted in Figure 8 b, showing that the streamwise mean velocity profile in the vertical ( $y, z$ ) plane at  $x/D = 1.01$  obtains a significantly less pronounced minimum than for the simulations with finer meshes. The results for the time- and space averaged  $C_p$  ( $C_{p,mean}$ ) distributions, presented in Figure 8 c, also show good agreement for the cases with finer meshes while the 13100\_m1 case yields more negative values in the cylinder nape. Considering the aforementioned behaviour of several flow characteristics, it is concluded that the mesh used in the 13100\_m3 case has sufficiently fine grid resolution.

Other numerical effects are also investigated, such as the influence of the time-step, the spanwise mesh density and the spanwise length. Having in mind the large consumption of memory and CPU hours, simulations with even more mesh elements than the 13100\_m3 case or with twice as large computational domain, and thus exceeding 20 million grid points, are demanding for the currently available computational resources. Therefore the analysis is made by comparison of the 13100\_1 case to the cases with varying time-steps (13100\_t2 and 13100\_t3 cases), the spanwise refined mesh 13100\_sm case and the elongated cylinder 13100\_sl case (spanwise length 8D).

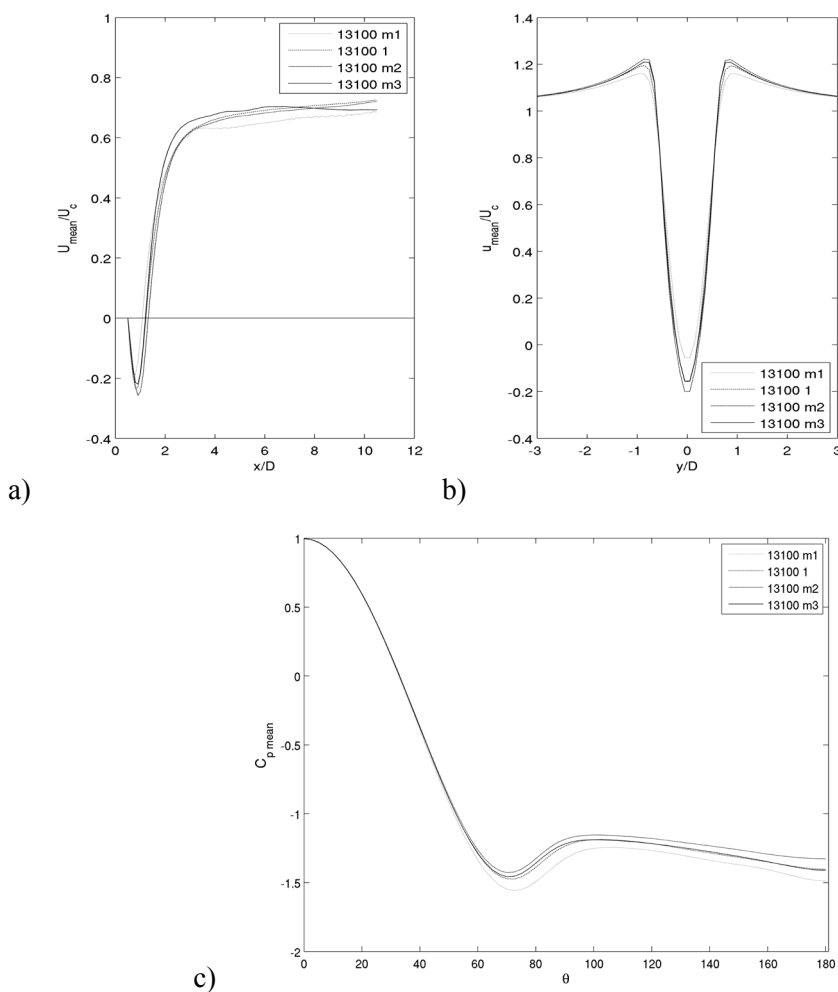


FIGURE 8: Time- and space-averaged flow properties for the  $Re = 13100$  cases with varying number of elements: a) streamwise velocity component ( $u$ ) profile in the cylinder wake, in the  $(x, z)$  plane,  $y/D = 0$ ; b) streamwise velocity component ( $u$ ) profile in the cylinder wake, in the  $(y, z)$  plane,  $y/D = 1.01$ ; c)  $C_{p, \text{mean}}$  distribution around the cylinder surface.  $\theta$  is measured from the cylinder front clockwise for the upper and anticlockwise for the lower half of the cylinder.

In Figure 9 a, the time- and space-averaged streamwise velocity component ( $u$ ) profiles in the  $(x, z)$  plane are shown for the three simulations with different time-steps. Along the comparison of the hydrodynamic quantities in Section 7.4.3.1, behaviour of the wake flow is compared for the 13100\_1, 13100\_t2 and 13100\_t3 cases. Figure 9 a leads to the conclusion that the time-steps used for these simulations are sufficiently small. A slight deviation in the streamwise mean velocity profile can be noticed

between  $x/D = 1.5$  and 3, but the difference is less than 3%.  $L_r$  for the three simulations obtains values between 0.674 and 0.722, which results in 3.5 % difference between the 13100\_t3 and 13100\_1 cases. The  $C_{p\text{ mean}}$  distributions for the cases with various time-steps are also calculated. Similar to the behaviour of the previously analysed flow parameters,  $C_{p\text{ mean}}$  distributions for all three simulations have differences smaller than 2%. Therefore it can be concluded that the dimensionless time-step of 0.00013, used in simulation 13100\_1 (and 13100\_m2, 13100\_m3, 13100\_sl, 13100\_sm) is sufficiently small.

Insufficient spanwise resolution could lead to large volumes of the individual elements and large aspect ratios of the element sides, which could cause numerical inaccuracies. In order to check the influence of the spanwise resolution, the 13100\_1 and 13100\_sm cases are simulated with the same (x, y) plane meshes, and changing the spanwise resolution from 100 to 150 elements per 4D cylinder length (Table 2). The results are: 0.5% difference in  $C_d$ , 3.7% difference in the  $C_{l\text{ rms}}$ , and 1.5% difference in  $St$ . A more thorough analysis is made by comparing the near-wake streamwise velocity (u) profiles in (x, z) plane (Figure 9 b) and  $L_r$ . The differences are negligible. Therefore the spanwise distribution of 100 elements per 4D length of the cylinder is considered to be sufficient.

Another numerical aspect examined is the influence of the spanwise length of the domain. Most of the previous studies used a domain width of  $\pi D$ . A slightly wider domain of 4D is used for the majority of the present simulations. Nevertheless the common use of a smaller spanwise length, the question arises whether the 3D effects of the flow are fully captured. Breuer (1998 b) noticed significant differences between 2D and 3D simulations, and slight differences in the results for the simulations with  $\pi D$  and  $2\pi D$  domain widths. Ouvrard et al. (2008) also discussed the importance of capturing the 3D effects of the flow, which was simulated fairly well even by using a relatively coarse mesh in the spanwise direction.

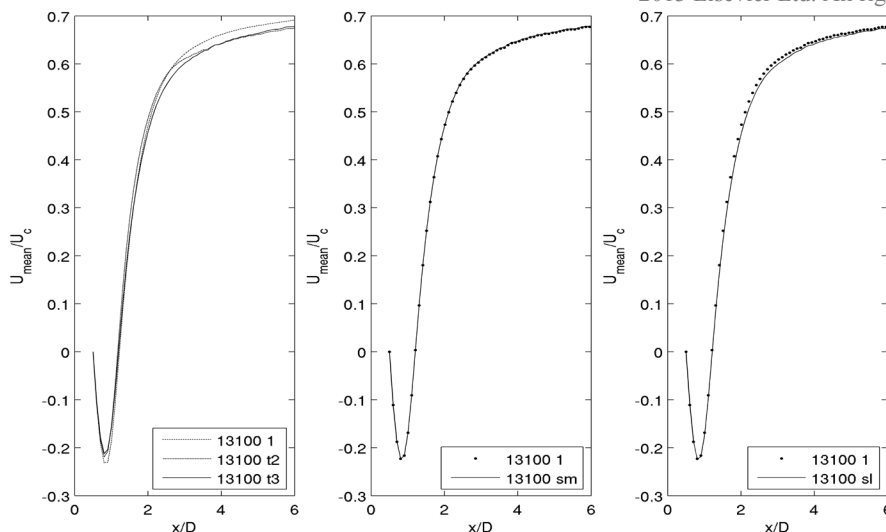


FIGURE 9: Time- and space-averaged streamwise velocity component ( $u$ ) profiles in the cylinder wake, in the  $(x, z)$  plane,  $y/D = 0$ .

a) versus the time-step; b) versus the mesh resolution in the spanwise direction; c) versus the cylinder spanwise length.

The 13100\_sl case is simulated with the spanwise length of  $8D$  with 200 elements in the  $z$  direction, keeping all the other numerical parameters the same as those used in the 13100\_1 case. The differences between the hydrodynamic quantities are again very small. Figure 9 c) shows the time- and space-averaged streamwise velocity component ( $u$ ) in the horizontal  $(x, z)$  plane behind the cylinder. In the region between  $x/D = 2$  and  $4$ , a somewhat longer propagation of the disturbance in the downstream direction is noticed for the 13100\_sl case. The differences in the mean velocity profiles and  $L_r$  are insignificant, and thus the simulations with the spanwise length of  $4D$  are considered acceptable.

### 7.4.3.3. Comparison with published experimental and numerical results

Following the conclusions from the convergence studies presented in the previous Sections, the 13100\_m3 case is chosen for further analysis, through hydrodynamic quantities and flow properties in the cylinder wake. Table 6 summarizes the present and the previously published studies of hydrodynamic quantities for the flow around a circular cylinder at comparable and higher  $Re$ . For  $Re$  similar to the

present study, published  $C_d$  values are between 1.0 (Cantwell and Coles, 1983) and 1.4 (Achenbach and Heinecke, 1981);  $St$  values between 0.188 (Fang and Han, 2011) and 0.215 (Cantwell and Coles, 1983). While there is limited published data for  $C_{l_{rms}}$ , the present values of  $C_d$  and  $St$  are within these intervals.

TABLE 6: Hydrodynamic quantities, primary ( $\Theta_1$ ) and secondary separation angle ( $\Theta_2$ ) – present results for  $Re = 13100$  and referred studies.

Case	$C_d$	$C_{l_{rms}}$	$St$	$\Theta_1$ (deg)	$\Theta_2$ (deg)
13100_m3	1.3132	0.5454	0.2038	87.6	106
Roshko (1961) $Re = 2.3 * 10^4$	1.1250		0.19 (Ribner, Etkin, 1959)		
Son and Hanratty (1969) $Re = 10^4, 2 * 10^4$				96 97	118 115
Ballengee and Chen (1971) $Re = 9.5 * 10^3, 1.7 * 10^4$				92 88.5	
Achenbach and Heinecke (1981), $Re = 2 * 10^4$ . (rough cylinder)	1.4		0.21		
Schewe (1983) $Re = 2.3 * 10^4$	1.1300	0.3200	0.1950		
Cantwell and Coles (1983) $Re \sim 1.3 * 10^4$	[1.0, 1.3]		[0.19-0.215]		
Norberg (1994) $Re = 13000$	0.98	0.04 – 0.15	0.20		
Breuer (1998 a) $Re = 3900$	[1.016-1.486]		0.22±0.005	[87.7- 95.2]	[111.3- 126]
Breuer (2000) $Re = 1.4 * 10^5$	[1.057-1.368]		[0.196-0.205]	[91.45- 96.6]	
Ouvrard et al. (2008) $Re = 1.4 * 10^5$	[0.54-0.62]			[108- 114]	
Ong et al. (2009) $Re = 3.6 * 10^6$	0.4574	0.0765	0.3052	114	
Fang and Han (2011) $Re = 5.6 * 10^3, 2.8 * 10^4$	[1.044-1.1] [1.029-1.127]		[0.188-0.195] [0.196-0.214]	[87-93] [98-105]	

The results of the 13100\_m3 case are examined through the details of the velocity and pressure fields in the vicinity of the cylinder. There are neither numerical nor experimental results of the wake flow details for this  $Re$ . Therefore a qualitative comparison is made between the 13100\_m3 case results and the previously published results for lower and higher  $Re$ . The comparison is made with the results for  $Re = 3900$



by Lourenco and Shih (1993), Norberg (1994), Tremblay et al. (2000) and Lysenko et al. (2012), with both the numerical and experimental results for  $Re = 140000$  by Breuer (2000), Cantwell and Coles (1983), and experimental studies with  $Re$  comparable with the present study by Thom (1928) and Lim and Lee (2002).

The velocity field in the cylinder wake is presented in Figure 10, through the time- and space-averaged streamwise velocity component ( $u$ ) sampled in the ( $x, z$ ) (Figure 10 a) and the ( $y, z$ ) plane (Figure 10 b). In Figure 10 a, the velocity profile between  $x/D = 0.5$  and  $x/D = 8$  in the cylinder wake is compared with the  $Re = 3900$  simulations of Tremblay et al. (2000) and Lysenko et al. (2012), the LES simulations of Breuer (2000) for  $Re = 140000$  and the experimental data of Cantwell and Coles (1983) for  $Re = 140000$ . It appears that qualitatively all the results show similar behaviour in the cylinder wake. As reported in the previous research (e.g. Zdravkovich (1990)), an increase in  $Re$  leads to a shorter recirculation length. That causes the velocity minimum being located closer to the cylinder. This behaviour can be noticed in Figure 10 a, where the minimum velocity for the 13100\_m3 case lies between the minima for the  $Re = 3900$  and  $Re = 140000$  simulations. This is also supported by comparison of the recirculation length.  $L_r$  for  $Re = 3900$  is reported to be between 1.19 and 1.67 (Table 4);  $L_r = 1.27$  for the 3900\_m4 case. For the present  $Re = 13100$ ,  $L_r$  is found to be 0.722 while for the higher  $Re$ , recirculation happens at about  $0.5D$  behind the cylinder base (Cantwell and Coles, 1983).

Figure 10 b shows the streamwise velocity component sampled along the vertical cross sections located  $1.01D$  behind the cylinder. Again, it appears that qualitatively the results are similar to the other numerical and experimental results, indicating the well-known V-shape velocity profile, similar to the one of the present  $Re = 3900$  cases. As expected, due to the longer recirculation bubble than for higher  $Re$ , the profiles with lower  $Re$  yield more pronounced velocity minima at the cylinder centreline at  $x/D = 1.06$ .

The results of the present study fall between the profiles for  $Re = 3900$  and  $140000$ , showing closer resemblance to the  $Re = 3900$  flow. That is in agreement with the theory of Zdravkovich (1990) which gathers the flows in the  $Re$  range 2000 to 20000 (thus including  $Re = 3900$  and  $Re = 13100$ ) in the flow class with the transition vortices in the free shear layers, while the  $Re = 140000$  flow falls into the next flow class with fully turbulent shear layers.

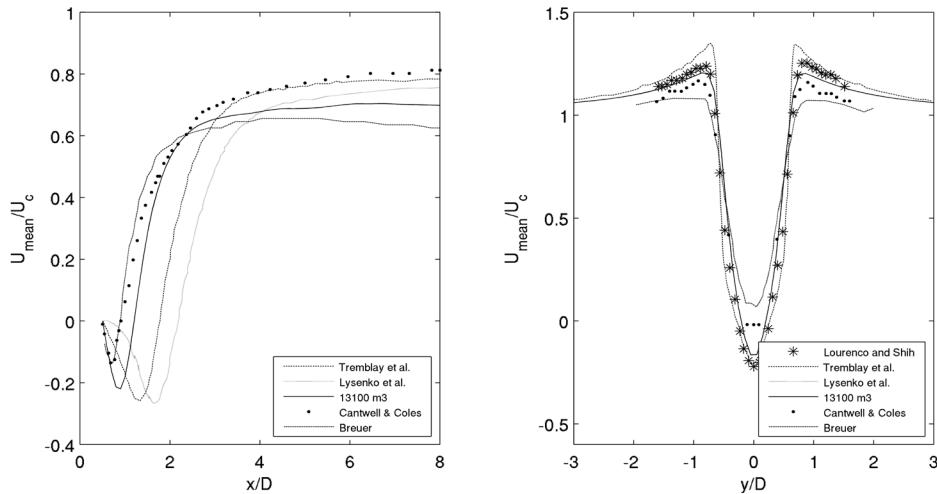


FIGURE 10: Time- and space-averaged streamwise velocity component ( $u$ ) profiles in the cylinder wake. Symbols:

$Re = 3900$ , \* Lourenco and Shih (1993); -.- Tremblay et al. (2000); ... Lysenko et al. (2012);

$Re = 13100$ , — 13100\_m3 case;

$Re = 140000$ , • Cantwell and Coles (1983); Breuer (2000).

a) in  $(x, z)$  plane,  $y/D = 0$ ;

b) in  $(y, z)$  plane,  $x/D = 1.06$ .

The  $C_{p, \text{mean}}$  distribution for the 13100\_m3 case is presented in Figure 11. For the similar  $Re$  as in the present study, it is compared with the experimental results of Thom (1929) and Lim and Lee (2002), to both numerical and experimental results for lower  $Re = 3900$  and to the experimental measurements for higher  $Re = 140000$ . Qualitatively, the pressure distribution follows the experimental and numerical results. Comparing the results for different  $Re$ , it can be noticed that with increasing  $Re$ , there is a trend of lower minima and more negative pressure at the lee side of the cylinder. Comparing the present results with  $Re = 3900$ , the trend has been captured. The absolute values of  $C_{p, \text{mean}}$  in the cylinder wake for the present study are, however, larger and the  $C_{p, \text{mean}}$  minimum is more pronounced than found by the investigations for both higher and lower  $Re$ . Krajnovic (2011), using LES of the flow around the finite cylinder at  $Re = 20000$ , and Lysenko et al. (2012) presenting the LES with Smagorinsky model for the compressible flow at  $Re = 3900$ , also report the lower  $C_{p, \text{mean}}$  minima than observed in the experiments by Norberg (1994). Based on these results, a more thorough analysis should be made to investigate the influence of the Smagorinsky subgrid scale model on the results.

Another flow parameter examined is the position of the separation point on the cylinder surface. Relying on the definition of the separation point as the point of zero

shear stress, it is calculated as a point of zero tangential velocity at the first mesh node next to the cylinder surface. The time-averaged velocity components in the streamwise ( $u$ ) and the crossflow ( $v$ ) direction are calculated and sampled at each mesh cell. The precision is therefore, for the 13100\_m3 case with 540 elements distributed circumferentially,  $0.67^\circ$ . The separation angle is analysed through its spanwise-averaged values.

Previously published results for the position of the separation point at comparable  $Re$  are scarce and the results are highly varying. Therefore the present results for  $Re = 3900$  are first compared with previous results for the same  $Re$ , while the  $Re = 13100$  results are compared with results from studies for both higher and lower  $Re$ . Two separation angles are detected. The smaller angle,  $\Theta_1$  (measured from the cylinder vertex clockwise for the upper and counter-clockwise for the lower half of the cylinder) determines the primary separation point. For the 3900\_m4 case,  $\Theta_1 = 86.4^\circ$ . That value compares very well with the PIV measurements of Lourenco and Shih (1993), as well as with the LES results of Breuer (1998 b), Parnaudeau et al. (2008) and Lysenko et al. (2012) for Smagorinsky and TKE model, reporting  $\Theta_1 = 86^\circ$ ;  $87^\circ$ ;  $86^\circ$ ;  $89^\circ$  and  $88^\circ$  respectively.

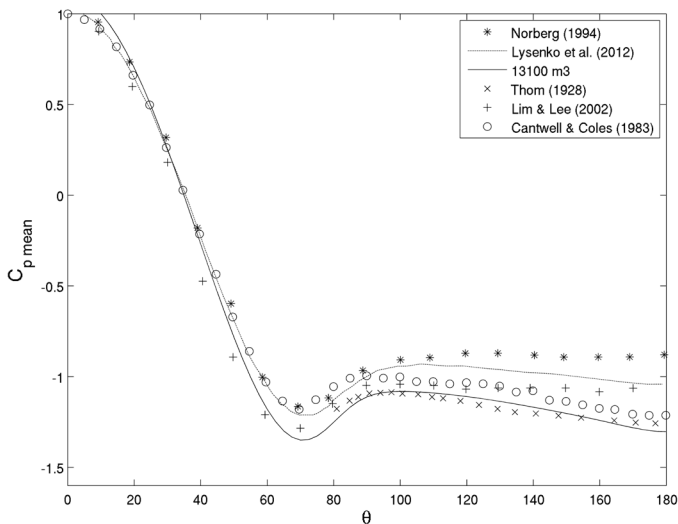


FIGURE 11: Time- and space-averaged  $C_{p \text{ mean}}$  distribution around the cylinder.

$Re = 3900$ , Norberg (1994) and Lysenko (2012);  $Re = 13100$ , case 13100\_m3;  $Re = 16700$ , Thom (1929);  $Re = 24000$ , Lim and Lee (2002);  $Re = 140000$ , Cantwell and Coles (1983).

Similarly, for the 13100\_m3 case, two separation points are present;  $\Theta_1 = 87.6^\circ$  and  $\Theta_2 = 106^\circ$ . For comparable  $Re$ , Ballengee and Chen (1971) presented  $\Theta_1 = 92^\circ$  for

$Re = 9.5 * 10^3$  and  $\Theta_1 = 88.5^\circ$  for  $Re = 1.7 * 10^4$ ; Fang and Han (2011) found  $\Theta_1$  between  $87^\circ$  and  $93^\circ$  for  $Re = 5.6 * 10^3$  and between  $98^\circ$  and  $105^\circ$  for  $Re = 2.8 * 10^4$ . According to Achenbach (1968), the position of the separation point depends on  $Re$ . For the subcritical flow, the separation point is expected to move downstream as  $Re$  increases, resulting in an increase of  $\Theta_1$ . The increase is relatively small, with  $\Theta_1$  varying between  $75^\circ$  and  $95^\circ$  in the subcritical flow regime, followed by a sudden jump due to transition to the critical flow, at  $Re$  about  $3*10^5$ , and a slight decrease in the supercritical flow regime, at  $Re$  about  $10^6$ . Accordingly, the present  $\Theta_1$  result ( $87.6^\circ$ ) is in good agreement with the theory, giving a slightly larger value than reported for  $Re = 3900$ , similar values as the aforementioned comparable  $Re$  and a smaller angle than obtained for higher  $Re$  (see Table 6).

Continuing downstream from the primary separation point, a small counter-rotating vortex is detected for both  $Re = 3900$  and  $Re = 13100$  simulations in the present studies. Figure 12 shows the time-averaged streamlines in the (x, y) plane, cross section at  $z/D = 2$  for the 13100\_m3 case. Small vortices are symmetrically located on both sides of the cylinder, extending over about  $18^\circ$  behind the primary separation point. Similar vortices were observed by Son and Hanratty (1969) for  $Re = 10^4$  and  $2 * 10^4$ , spanning over approximately  $25^\circ$ . Breuer (1998 a) and Lysenko et al. (2012) captured the secondary circulation by LES for  $Re = 3900$ , covering about  $25^\circ$  behind  $\Theta_1$ .

## 7.5. Conclusions

The flow around a circular cylinder in a uniform incoming flow for intermediate and moderately high Reynolds numbers is investigated using LES with Smagorinsky subgrid scale turbulence closure. The numerical code OpenFOAM is used for all simulations. The validation is carried out through the benchmark case of the flow around a circular cylinder at  $Re = 3900$ . The results are analysed through the hydrodynamic values of drag and lift coefficients and through the flow profiles in the near wake of the cylinder. Good agreement is obtained between the present results and the results from previously published studies, carried out with various numerical models, such as LES and DNS, as well as by experiments. The LES with Smagorinsky turbulence closure performs well in the studied subcritical flow regime.

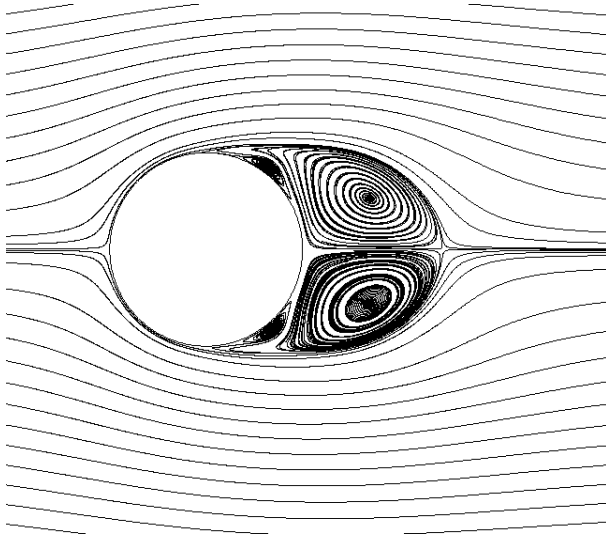


FIGURE 12: Time-averaged streamlines in the (x, y) plane, cross section at  $z/D = 2$ ; 13100\_m3 case. Primary and secondary separation can be seen.

The same numerical model is further used to simulate the flow at higher  $Re$  in the subcritical flow regime,  $Re = 13100$ . The influences of the different numerical parameters are investigated, such as mesh refinement, time-step, and cylinder spanwise length, with emphasis on the influences of the boundary conditions. The results are examined through the hydrodynamic quantities  $C_d$ ,  $C_{l_{rms}}$ , and  $St$ , the distribution of  $C_{p_{mean}}$  on the cylinder surface, the velocity distribution in the cylinder wake, the recirculation length and the separation angle. Since there are no publications of the flow details for the present  $Re$ , the results are compared qualitatively with published results for the same flow regime.

The main findings are:

- Even for the meshes with fine resolution on the cylinder surface ( $\delta^+ < 1$ ), the mesh resolution in the cylinder near wake has a significant effect on the results.
- Since the flow in the chosen regime is 3D, the domain, and thus the cylinder length, should be chosen such that it captures the 3D flow effects. It is concluded that a domain width of  $4D$  is sufficient.
- High spanwise mesh resolution does not change the results significantly.
- The results are not very sensitive to the choice of the time-step, as long as the Courant number is kept reasonably low.

- With increasing  $Re$ , the trend of shortening of the recirculation length is captured, as well as the trend of increasing separation angle.
- A small recirculation vortex is captured, extending over approximately  $20^\circ$  behind the primary separation point.

In general, the results for the flow parameters are in reasonably good agreement with previous research. The pressure and the velocity distributions on the cylinder surface and in the near wake show good agreement with the previous experimental results. Comparison with the previous numerical results for lower and higher  $Re$  shows good qualitative agreement, following the previously documented trends. Therefore it appears that LES are suitable for the flow in the chosen flow regime.

### *Acknowledgement*

This work has been supported by the Norwegian University of Science and Technology. Computing time, supported by NOTUR (the Norwegian Metacenter for Computational Science) is granted by the Norwegian Research Council and the Norwegian University of Science and Technology. This support is gratefully acknowledged. We are grateful to Tufan Arslan for technical support and valuable discussions.

## References

- Achenbach, E., 1968. Distribution of local pressure and skin friction in cross flow around a circular cylinder up to  $Re = 5 \times 10^6$ . *Journal of Fluid Mechanics*. 34, 625-39.
- Achenbach, E., Heinecke, E., 1981. On vortex shedding from smooth and rough cylinders in the range of Reynolds numbers  $6 \times 10^3$  to  $5 \times 10^6$ . *Journal of Fluid Mechanics*. 109, 239-251.
- Ballengee, D. W., Chen, C. F., 1971. Experimental determination of the separation point of flow around the circular cylinder. Published in Zdravkovich, M. M., 1997. *Flow Around Circular Cylinders, Vol 1: Fundamentals*. Oxford University Press, Oxford, UK.
- Breuer, M., 1998 a. Numerical and modeling influences on large eddy simulations for the flow past a circular cylinder. *International Journal of Heat and Fluid Flow*. 19, 512-521.
- Breuer, M., 1998 b. Large eddy simulation of the subcritical flow past a circular cylinder: numerical and modeling aspects. *International Journal for Numerical Methods in Fluids*. 28, 1280-1302.
- Breuer, M., 2000. A challenging case for large eddy simulation of high Reynolds number circular cylinder flow. *International Journal of Heat and Fluid Flow*. 21, 648-654.
- Cantwell, B., Coles, D., 1983. An experimental study of entrainment and transport in the turbulent near wake of a circular cylinder. *Journal of Fluid Mechanics*. 136, 321-374.
- Catalano, P., Wang, M., Iaccarino, G., Moin, P., 2003. Numerical simulation of the flow around a circular cylinder at high Reynolds numbers. *International Journal of Heat and Fluid Flow*. 24, 463-469.
- Diana, G., Belloli, M., Giappino, S., Muggiasca, S., 2008. Vortex induced vibrations at high Reynolds numbers. *BBAA VI International Colloquium on: Bluff Bodies Aerodynamics & Applications*, Milano, Italy.
- Fang, Y., Han, Z., 2011. Numerical experimental research on the hydrodynamic performance of flow around a three dimensional circular cylinder. *Applied Mechanics and Materials*. 90-93, 2778-2781.
- Ferziger, J. H., Peric, M., 2001. *Computational Methods for Fluid Dynamics*, 3rd Ed. Springer-Verlag, Berlin, Germany.
- Franke, J., Frank, W., 2002. Large eddy simulation of the flow past a circular cylinder at  $Re_D = 3900$ . *Journal of Wind Engineering and Industrial Aerodynamics*. 90, 1191-1206.
- Germano, M., Piomelli, U., Moin, P., Cabbot, W. H., 1991. A dynamic subgrid scale eddy viscosity model. *Physics of Fluids A*. 3 (7), 1760-1765.
- Heggernes, K., 2005. *Numerical Simulation of Three-dimensional Viscous Flow Around Marine Structures*, Doctoral Thesis. Norwegian University of Science and Technology. 2005:170.
- Krajnovic, S., 2011. Flow around a tall finite cylinder explored by large eddy simulation. *Journal of Fluid Mechanics*, 676, 294-317.
- Li, Y., 2011. Large eddy simulation of flow around a cylinder at  $Re=3900$  using a CFD code. *Applied Mechanics and Materials*. 94-96, 1707-1710.
- Lilly, D. K., 1992. A proposed modification of the Germano subgrid-scale closure method. *Physics of Fluids A*. 4 (3), 633 – 635.
- Lim, H. C., Lee, S. J., 2002. Flow control of circular cylinders with longitudinal grooved surfaces. *AIAA Journal*, 40, 10, 2027-2036.
- Lin, Z., Zhao, D., Song, J., 2011. The influence of advection schemes and turbulence closure models on drag coefficient calculation around a circular cylinder at high Reynolds

number. Journal of Ocean University of China (Oceanic and Coastal Sea Research). 10 3, 229-233.

Linke, W., 1931. New measurements on aerodynamics of cylinders, particularly their friction resistance (in German). *Physikalische Zeitschrift*. 32, 900 – 14. Published in Zdravkovich, M. M., 1997. *Flow Around Circular Cylinders, Vol 1: Fundamentals*. Oxford University Press, Oxford, UK.

Lourenco, L. M., Shih, C., 1993. Characteristics of the plane turbulent near wake of a circular cylinder, a particle image velocimetry study. Published in Beaudan, P., Moin, P., 1994. Numerical experiments on the flow past a circular cylinder at sub-critical Reynolds number. Report no. TF-62, Thermosciences Division, Department of Mechanical Engineering, Stanford University, USA.

Lysenko, D. A., Ertesvåg, I. E., Rian, K. E., 2012. Large-eddy simulation of the flow over a circular cylinder at Reynolds number 3900 using the OpenFOAM toolbox. *Flow Turbulence Combust.* 89:491-518.

Norberg, C., 1994. An experimental investigation of the flow around a circular cylinder: investigation of the aspect ratio. *Journal of Fluid Mechanics*. 258, 287-316.

Ong, L., Wallace, J., 1996. Velocity field of the turbulent very near wake of a circular cylinder. *Experiments in Fluids*. 20, 441-453.

Ong, M. C., Utnes, T., Holmedal, L. E., Myrhaug, D., Pettersen, B., 2009. Numerical simulation of flow around a smooth circular cylinder at very high Reynolds numbers. *Marine Structures*. 22, 142-153.

OpenFOAM, 2011. The open source CFD toolbox, programmer's guide, version 2.1.0. OpenFoam Foundation. Accessible 21.9.2012. on: <http://www.scribd.com/doc/80373296/UserGuide>.

Ouvrard, H., Koobus, B., Salvetti, M-V., Camarri, S., Dervieux, A., 2008. Variation multiscale LES and hybrid RANS/LES parallel simulation of complex unsteady flows. VECPAR 2008. Ed: Palma, J. M. L. M. et al. Springer-Verlag, Berlin. LNCS 5336, 465-478.

Parnaudeau, P., Carlier, J., Heitz, D., Lamballais, E., 2008. Experimental and numerical studies of the flow over a circular cylinder at Reynolds number 3900. *Physics of Fluids*. 20, 085101.

Ribner, H. S., Etkin, B., 1959. Noise research in Canada. Proceedings of the 1<sup>st</sup> International Congress of Aero. Sci, Madrid. Published by Pergamon Press, London, UK.

Roshko, A., 1961. Experiments on the flow past a circular cylinder at very high Reynolds numbers. *Journal of Fluid Mechanics*. 10, 345-356.

Schewe, G., 1983. On the force fluctuations on a circular cylinder in crossflow from subcritical up to transcritical Reynolds numbers. *Journal of Fluid Mechanics*. 133, 265-285.

Schlichting, H., 1979. *Boundary Layer Theory*. McGraw Hill Inc, USA.

Smagorinsky, J., 1963. General circulation experiments with the primitive equations. *Monthly Weather Review*. 91-3, 99-164.

Son, J. S., Hanratty, T. J., 1969. Velocity gradients at the wall for flow around a cylinder at Reynolds numbers from 5k to 100k. *Journal of Fluid Mechanics*. 35, 353-68.

Thom, A., 1928. An investigation of fluid flow in two-dimensions. Aeronautical Research Council, Reports & Memoranda 1194 (Th. Numerical Calc.).

Tremblay, F., Manhart, M., Friedrich, R., 2000. DNS of flow around the circular cylinder at subcritical Reynolds number with Cartesian grids. Proceedings of the 8<sup>th</sup> European Turbulence Conference, EUROMECH, Barcelona, Spain. 659-662.

Tremblay, F., Manhart, M., Friedrich, R., 2002. LES of flow around a circular cylinder at a subcritical Reynolds number with Cartesian grids. *Advances in LES of Complex Flows*.



Kluwer Academic Publishers, Netherlands. 133-150.

Vaz, G., Mabilat, C., van der Wal, R., Gallagher, P., 2007. Viscous flow computations on smooth cylinders, a detailed numerical study with validation. Proceedings of the 26<sup>th</sup> International Conference on Offshore Mechanics and Arctic Engineering, San Diego, California. OMAE2007-29275.

Weller, H. G., Tabor, G., Jasak, H., Fureby, C., 1998. A tensorial approach to computational fluid continuum mechanics using object-oriented techniques. Computers in Physics. 12-6, 620-631.

Wissink, J. G., Rodi, W., 2008. Large-scale computations of flow around a circular cylinder. Published in Resch, M., Roller, S., Lammers, P., Furui, T., Galle, M., Bez, W. 2008. High Performance Computing on Vector Systems. Springer-Verlag, Berlin Heidelberg, Germany.

Zdravkovich, M. M., 1990. Conceptual overview of laminar and turbulent flows past smooth and rough circular cylinders. Journal of Wind Engineering and Industrial Aerodynamics. 33, 53-62.

Zhang, J., Dalton, C., 1996. Interactions of vortex-induced vibrations of a circular cylinder and a steady approach flow at a Reynolds number of 13,000. Computers and Fluids. 25-3, 283-294.



## Chapter 8

# Large Eddy Simulations of flow around a circular cylinder close to a flat seabed

*Mia Abrahamsen Prsic\**, *Muk Chen Ong<sup>#</sup>*, *Bjørnar Pettersen\**, *Dag Myrhaug\**

*\* Department of Marine Technology, Norwegian University of Science and Technology, NO-7491 Trondheim, Norway*

*<sup>#</sup> Department of Mechanical and Structural Engineering and Materials Science, University of Stavanger, NO-4036 Stavanger, Norway*

### ***Abstract***

Large Eddy Simulations (LES) with Smagorinsky subgrid scale model are used to study the turbulent flow and wake dynamics behind a circular cylinder close to a horizontal, plane wall at subcritical Reynolds number. The focus is on investigating the details of the flow around the cylinder placed at different distances from the wall and immersed in boundary layers of various thicknesses.

The Reynolds number is  $Re = 13100$ . The simulations with gap to diameter ratios ( $G/D$ ) of 0.2, 0.6 and 1 are carried out in order to investigate the changes of the flow field and the vortex shedding due to the presence of the plane wall. The influence of the incoming boundary layer profile is investigated through simulations with logarithmic boundary layer inlet profile of thickness  $0.48D$  and  $1.6D$ , and compared with a uniform inlet flow profile. 2D and 3D simulations are performed for  $Re$  ranging from 100 to 13100, to explore the importance of the flow three-dimensionality. The flow field in the cylinder wake, as well as the mean flow values, the spectral analysis and the pressure distribution on the cylinder surface are computed to study the flow physics due to the influences of the wall.

Keywords: LES; circular cylinder; plane wall interaction; boundary layer flow.

## 8.1. Introduction

Circular, cylindrical structures appear in many practical situations in the marine technology environment, subsea pipelines being one of them. The flow around a circular cylinder in an infinite fluid is governed by the Reynolds number ( $Re = U_c D / \nu$ , where  $U_c$  is the free stream velocity,  $D$  is the cylinder diameter and  $\nu$  is the kinematic viscosity of the fluid). The wake, whether laminar or turbulent, is symmetric and for  $Re > 40$ , vortices are shed periodically from the two sides of the cylinder. Proximity of the sea bottom significantly changes the flow around the pipeline and its wake. The key parameters affecting the flow, besides from  $Re$ , are the gap between the pipeline and the seabed, and the boundary layer profile of the incoming flow. In various combinations, they result in wake flow in the range from regular vortex shedding, to reattached flow with completely suppressed vortex shedding.

LES are utilized to simulate the three-dimensional (3D) flow around a circular cylinder in the vicinity of a rigid, plane wall. The simulations are made for the intermediate  $Re = 13100$ . In the North Sea, at the water depth of about 100 m, the pipelines are usually exposed to current of between 0.02 m/s and 0.5 m/s [5]. The diameter of a pipeline can vary from as much as 1.066 m (44''), through commonly used 0.76 m (30'') and 0.404 m (16'') to as small as 0.05 m (2'') [6]. The chosen  $Re$  thus covers a variety of combinations of operational conditions for subsea pipelines.

Several detailed experimental studies were carried out at subcritical  $Re = O(10^4)$ . In this  $Re$  range, the vortex shedding is relatively insensitive to  $Re$  variation, allowing data comparison for studies conducted at slightly different  $Re$ . Particle Image Velocimetry (PIV) measurements were performed in [7] for  $Re$  between 1200 and 4960; [8] for  $Re = 840, 4150$  and 9500. [9] measured the flow features for  $Re = 12000$ . Point measurements of pressure and velocity in the flow fields for comparable  $Re$  are presented at [10], [11] and [12].

LES have proven to be a successful model for detailed simulations of the flow around a circular cylinder in an infinite fluid and uniform inflow in the subcritical flow regime. Breuer [1] presented an extensive analysis of the influence of the subgrid scale models, the grid resolution and the discretization schemes on the quality of the LES results. Tremblay et al. [2] carried out a series of LES and compared them with the results from Direct Numerical Simulations (DNS). Parnaudeau et al. [3] focused on the comparison of their LES results of the near wake flow with the experimental results obtained by PIV. Abrahamsen Prsic et al. [4] investigated the influence of the numerical parameters on LES and discussed the details of the near wake flow for the same  $Re$  as chosen in this study.

For the cylinder in the vicinity of a wall, several researchers performed two-dimensional (2D) simulations using Reynolds – Averaged Navier–Stokes (RANS) models. At a comparable Re, [13] and [14] performed the simulations with URANS  $k-\epsilon$  model. Even though the model provided a good qualitative agreement with the experimental results, RANS showed significant limitations. Modelling of the intrinsically 3D flow with 2D simulations led to the under-prediction of the drag and the lift forces. A three-dimensional LES model is therefore utilized in the present study. LES were also used to simulate the flow around a square cylinder in the vicinity of a plane wall, at a comparable Re = 22000; [16] and [17] provided promising results and good comparison to the experimental research. Based on these references, LES are considered to be an appropriate tool for performing the simulations of the flow around a circular cylinder in the vicinity of a plane wall at intermediate Re.

## 8.2. Numerical method

### 8.2.1. Governing equations

In the present study, the incompressible Navier-Stokes equations are solved by LES. In the filtered form, the continuity and the momentum equations can be written:

$$\frac{\partial \bar{u}_i}{\partial x_i} = 0 \quad (1)$$

$$\frac{\partial \bar{u}_i}{\partial t} + \frac{\partial (\bar{u}_i \bar{u}_j)}{\partial x_j} = -\frac{1}{\rho} \frac{\partial \bar{p}}{\partial x_i} + \nu \frac{\partial^2 \bar{u}_i}{\partial x_j^2} - \frac{\partial \tau_{ij}}{\partial x_j} \quad (2)$$

where  $u_i$ ,  $i = 1, 2, 3$  denotes the filtered velocity component in streamwise ( $x$ ), crossflow ( $y$ ) and spanwise ( $z$ ) direction respectively ( $x_i$  is assigned to the respective directions),  $\rho$  is the density of the fluid and  $p$  is the filtered pressure.  $\tau_{ij}$  represents the non-resolvable subgrid stress, given by:

$$\tau_{ij} = \overline{u_i u_j} - \bar{u}_i \bar{u}_j \quad (3)$$

Here,  $\tau_{ij}$  describes the influence of the small scale structures on the large eddies. LES is in detail presented in [20]. The subgrid scale motions are modelled by a commonly used Smagorinsky model proposed in [18]. It assumes that the eddy viscosity is proportional to the subgrid scale characteristic length and to the characteristic subgrid scale velocity. The Smagorinsky constant is fixed;  $C_s = 0.2$  in the present study. Several studies compared the performance of various LES subgrid scale models for the case of a cylinder in an unlimited fluid at Re = 3900. [1], [2], [15] and [19] showed that

the standard Smagorinsky model performs well in comparison to the more complex subgrid scale models for the type of flow similar to the present study.

All the simulations are performed using the open source code OpenFOAM. The PISO algorithm (Pressure Implicit with Splitting of Operators, see [20]) is used to solve the Navier-Stokes equations. For the time integration, an implicit, backward differencing method of second order is used. Spatial schemes for the gradient terms are Gauss linear and Gauss limited linear. All of the above schemes are of second order accuracy, most commonly used in engineering applications of LES, [21]. Discussion of the influences of the various numerical parameters can be found in [1], confirming the validity of the choice of central differencing schemes for the convective terms.

### 8.2.2. Computational setup

The LES are performed on a 3D rectangular computational domain extending from  $10D$  in front of the cylinder to  $30D$  in the wake. In the crossflow direction, it extends from the rigid wall at  $G$  clearance to  $10D$  above the cylinder centre (Figure 1). The spanwise length of the domain is  $4D$  (and  $8D$  for one case). The chosen domain is larger than the domains successfully used in several studies of the flow with comparable and higher  $Re$ , amongst others [4], [22] and [23]. It is therefore believed that the domain boundaries have negligible influence on the flow close to the pipeline in the present study. Detailed discussion of the domain sizes is given in [4].

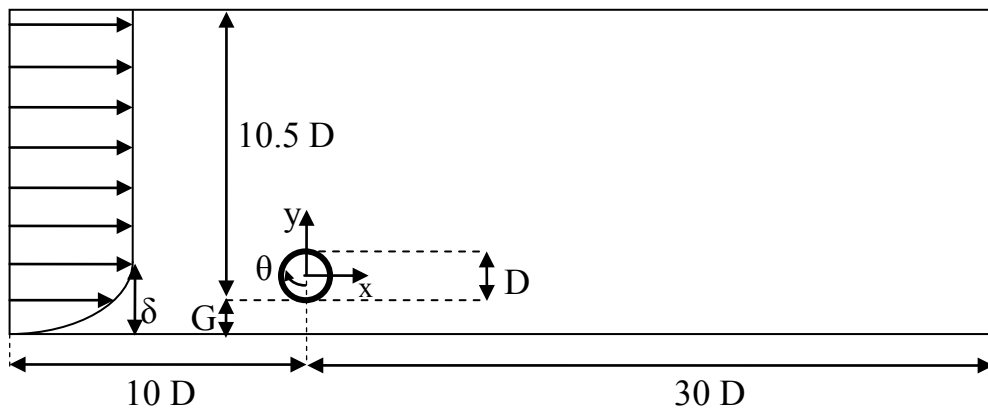


Figure1. Definition sketch for the cylinder in the vicinity of a plane wall. Coordinate system origin is in the centre of the cylinder,  $z/D = 0$ ,  $z/D = 0$ , 4. In the present study, gap to diameter ratio  $G/D = 0.2, 0.6$  and  $1$ ; boundary layer thickness  $\delta/D = 0, 0.48$  and  $1.6$ .

A body-fitted, structured O-mesh is used. The details of the mesh are presented in Figure 2. In all simulations, the size of the elements near the cylinder and the horizontal bottom wall is chosen such that the maximum dimensionless wall distance  $\eta^+$  is kept below 1. Here  $\eta^+$  is defined as  $\eta^+ = u_* \eta'/\nu$ , where  $u_*$  denotes the friction velocity near the wall, and  $\eta'$  is the normal distance from the wall. Detailed grid convergence studies are presented in Section 8.3.2.

The boundary conditions are kept the same through the entire study. A boundary layer flow is specified by imposing a logarithmic profile at the inlet. Several boundary layer thicknesses are used (see Table 1 and 3). The incoming free stream velocity outside the boundary layer is constant. At the outlet, the pressure and the normal gradient of the velocity are set to zero. The upper boundary is defined as a symmetry boundary condition. The boundaries normal to the cylinder axis have the periodic boundary conditions, while the no-slip condition is applied on the fixed cylinder surface and the bottom wall.

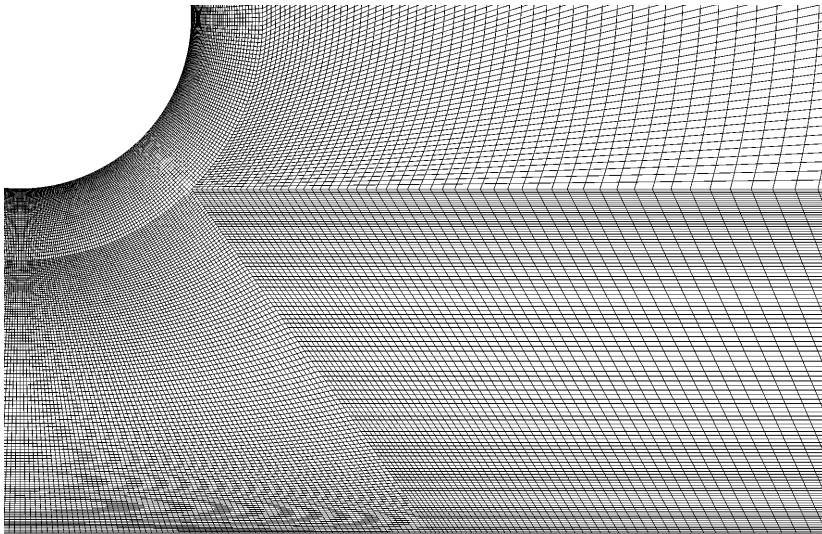


Figure 2. Details of the mesh – zones in the vicinity of the cylinder, the wall and in the near wake region. Gap to diameter ratio,  $G/D = 1$ .

### 8.3. Code validation and convergence studies

#### 8.3.1. Cylinder in an infinite fluid at Re = 13100 – code validation

The OpenFOAM LES code is validated through a simpler and thoroughly investigated case – the flow around a circular cylinder in an infinite fluid, subjected to a uniform inflow. The validation was performed in [4] for the benchmark case of Re = 3900 and a higher Re = 13100 case. Details of the simulations, the convergence studies and the thorough analysis of the results are presented in [4]. The code is validated by comparing the LES results to numerical and experimental results available. The results are analysed through the time- and spanwise-averaged drag and lift coefficients, the velocity profiles in the cylinder wake, the mean recirculation length ( $L_r$ ) and the time-averaged streamlines in the cylinder wake. The results, in details discussed in [4], compare well to the previously published research. It is thus confirmed that LES with the Smagorinsky model, performed by using the OpenFOAM code, are suitable for simulating the flow in the subcritical flow regime.

#### 8.3.2. Cylinder in the vicinity of a wall - convergence studies

To mimic a fully developed boundary layer profile that free spanning pipelines close to the seabed encounter in the natural environment, the inlet flow is simulated with a logarithmic profile in the vicinity of the wall. Vertically dependant streamwise velocity  $u(y)$  is defined as:

$$u(y) = \min \left\{ \frac{u_*}{\kappa} \ln \left( \frac{y}{z_w} \right), U_c \right\} \quad (4)$$

$$u_* = \frac{\kappa U_c}{\ln(\delta / z_w)} \quad (5)$$

Here  $U_c$  is the free stream velocity,  $\kappa = 0.41$  is the von Karman constant,  $z_w = 1 \times 10^{-6}$  m is the seabed roughness, and  $\delta$  is the dimensional boundary layer thickness. The dimensionless boundary layer thickness ( $\delta/D = 1.6$  and  $0.48$ ) is imposed on the domain inlet,  $10D$  upstream from the cylinder. To check the behaviour of the profile when it approaches the cylinder, the following simulation is performed. Keeping the same domain size, the cylinder is removed and an orthogonal mesh is created with the same resolution in the vicinity of the wall (see Table 1 – boundary layer). The streamwise velocity is averaged in time for the fully developed flow and sampled on several vertical cross-sections between the inlet and the position of the cylinder, indicated in Figure 3a. Comparison of the velocity profiles at these cross-



sections (Figure 3b) shows only negligible changes of the profile along the wall in front of the cylinder. This leads to the conclusion that the cylinder is exposed to a fully developed boundary layer profile with the chosen  $\delta/D$ .

The flow around the cylinder in the vicinity of a wall is divided into two distinctive categories – the narrow and the wide gap flow. Due to the intrinsic differences in the flow behaviour, a grid convergence study is performed for both flow regimes.  $G/D = 0.2$  and  $0.6$  represent the narrow and the wide gap flow regime, respectively. The boundary layer thickness,  $\delta/D = 1.6$ , is kept the same in both cases. Following the ASME Standard for Verification and Validation [24], three meshes are created for each grid study. The size of the elements at the cylinder and the bottom wall surface is kept constant for these simulations. In the grid refinement sequence, the grid cells are geometrically similar, with constant refinement factor in all directions, [24]. The elements in the gap and close to the cylinder maintain the same shape and overall distribution. Details about the cases can be found in Table 1 - mesh.

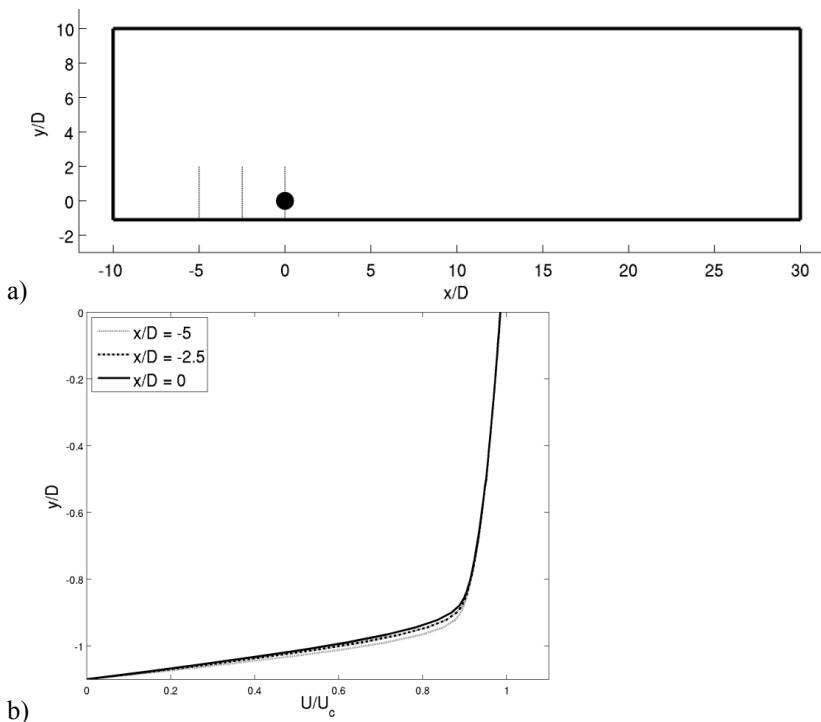


Figure 3. a) Schematic representation of the computational domain slice in  $(x, y)$  plane,  $z/D = 2$ . Positions of the velocity sampling cross-sections are indicated with dotted lines.

b) time-averaged and normalized streamwise velocity component ( $U/U_c$ ) profile at three cross-sections.  $\delta/D = 1.6$ , case wall00.

TABLE 1: Numerical set-up for all convergence study cases.  $\delta/D = 1.6$ .

Case	Key parameter	Re	G/D	Computational domain (x D)	Total number of elements (million)	Number of elements circumf.	Time-step $\Delta t$ (s)
G06 m1	Mesh	13100	0.6	40 x 11.1 x	7.5	360	0.0001
G06 l	Gap	13100	0.6	40 x 11.1 x 4	9.5	410	0.0001
G06 m2	Mesh	13100	0.6	40 x 11.1 x 4	12.5	440	0.0001
G06 t1	Time-step	13100	0.6	40 x 11.1 x 4	9.5	410	0.00025
G06 t2	Time-step	13100	0.6	40 x 11.1 x 4	9.5	410	0.0005
2D Re100	3D effects	100	0.6	40 x 11.1 (2D)	0.02	200	0.0001
Re100 4D	3D effects	100	0.6	40 x 11.1 x 4	2	200	0.0001
2D Re500	3D effects	500	0.6	40 x 11.1 (2D)	0.023	215	0.0001
Re500 4D	3D effects	500	0.6	40 x 11.1 x 4	2.3	215	0.0001
2D Re1000	3D effects	1000	0.6	40 x 11.1 (2D)	0.5	320	0.0001
Re1000 4D	3D effects	1000	0.6	40 x 11.1 x 4	5	320	0.0001
2D Re3900	3D effects	3900	0.6	40 x 11.1 (2D)	0.75	360	0.0001
Re3900 4D	3D effects	3900	0.6	40 x 11.1 x 4	7.5	360	0.0001
2D Re7800	3D effects	7800	0.6	40 x 11.1 (2D)	0.75	360	0.0001
Re7800 4D	3D effects	7800	0.6	40 x 11.1 x 4	7.5	360	0.0001
G06 L8	Spanwise length	13100	0.6	40 x 11.1 x 8	19	410	0.0001
G02 m1	Mesh	13100	0.2	40 x 10.6 x 4	5.2	360	0.0001
G02 m2	Mesh	13100	0.2	40 x 10.6 x 4	7.2	410	0.0001
G02 l	Gap	13100	0.2	40 x 10.6 x 4	9.5	460	0.0001
wall00	Boundary layer	13100	No cyl.	40 x 11.1 x 4	7.2	No cylinder	0.0001

The influence of the mesh and the time-step is first analysed through the time- and spanwise-averaged (mean) drag coefficient ( $\overline{C_d}$ ), the mean lift coefficient ( $\overline{C_l}$ ), the root-mean-square of the lift coefficient ( $C_{l_{rms}} = \overline{(C_l^2)}^{1/2}$ ) and the Strouhal number (St), see Table 2. The aforementioned drag ( $C_d$ ) and lift ( $C_l$ ) coefficients are defined as:  $C_d = F_d / (0.5\rho U_c^2 A)$  where  $F_d$  is the drag force exerted on the entire cylinder, and  $A$  is the projected area of the cylinder;  $C_l = F_l / (0.5\rho U_c^2 A)$ , where  $F_l$  is the integrated lift

force. The Strouhal number is defined as  $St = f D/U_c$ , where  $f$  is the vortex shedding frequency.

TABLE 2: Mean flow parameters for all convergence study cases.  $G/D = 0.2$  and  $0.6$ ;  $\delta/D = 1.6$ .

Case	Key parameter	$\overline{C_d}$	$\overline{C_l}$	$C_{lrms}$	St
G06 m1	Mesh	1.061	0.070	0.106	0.273
G06 1	Gap	1.060	0.083	0.115	0.278
G06 m2	Mesh	1.049	0.083	0.099	0.287
G06 t1	Time-step	1.099	0.092	0.171	0.253
G06 t2	Time-step	1.109	0.081	0.179	0.259
Re100 0D	3D effects	1.257	0.049	0.049	
Re100 4D	3D effects	1.256	0.049	0.049	
Re500 0D	3D effects	1.299	0.040	0.676	
Re500 4D	3D effects	1.296	0.038	0.685	
Re1000 0D	3D effects	1.321	0.019	0.883	
Re1000 4D	3D effects	1.139	0.050	0.366	
Re3900 0D	3D effects	1.629	0.253	1.320	
Re3900 4D	3D effects	1.221	0.043	0.385	
Re7800 0D	3D effects	1.657	0.183	1.383	
Re7800 4D	3D effects	1.087	0.079	0.138	
G06 L0	Spanwise length	1.695	0.123	1.400	
G06 L8	Spanwise length	1.080	0.091	0.126	0.271
G02 m1	Mesh	0.885	0.040	0.041	-
G02 m2	Mesh	0.887	0.043	0.043	-
G02 1	Gap	0.889	0.045	0.044	-

At  $G/D = 0.6$ , the results for different meshes (see Table 2) suggest that convergence is achieved. The mesh refinement leads to a slight decrease in  $\overline{C_d}$ , but the difference in the values between the finest and the coarsest mesh is only 1.1%.  $\overline{C_l}$  increases 15% between the cases with the coarsest and the intermediate mesh, while further mesh refinement leads to a decrease of only 0.6%. The variations in  $C_{lrms}$  are less than 7% from the finest to the coarsest mesh. St increases 2% between the coarse and the intermediate mesh and 3% for the further refinement. These results suggest that the mesh with 9.5 million elements (case G06 1) provides sufficient refinement.

The grid convergence study for  $G/D = 0.2$  is shown in Table 2.  $\overline{C_d}$  varies only 0.5% between the cases with the coarse and the fine mesh. The mesh refinement from 5.2 to 7.2 million elements leads to 7.7% increase in  $\overline{C_l}$  and 6% increase in  $C_{lrms}$ . Further mesh refinement to 9.5 million elements results in 4.8% increase of  $\overline{C_l}$  and

2.5% of  $C_{l_{rms}}$ . Since there is no periodic oscillations due to cease of vortex shedding,  $St$  is not investigated. These results suggest that the finest mesh (G02 1 case) is fine enough for the further analysis.

The velocity field is analysed over several vertical cross-sections ( $y, z$  plane). They are positioned from  $x/D = 0$  (at the centre of the cylinder) to 8.5, with more focus on the near wake. The mean streamwise velocity ( $U$ ) is sampled at several cross-sections distributed evenly along the cylinder span ( $z$ -axis direction) and spanwise-averaged for each  $x/D$ . Such mean velocity profiles for  $G/D = 0.6$  are presented in Figure 4a. Close to the cylinder, simulations with all three meshes yield profiles with no significant differences. Due to the mesh stretching, slight discrepancies develop for  $x/D \geq 1.5$ . The differences between all three cases are, however, small along the cylinder wake. Very similar behaviour is observed for  $G/D = 0.2$ , presented in Figure 4b. Combined with the results of the mean flow values, this leads to the conclusion that cases G06 1 and G02 1 have sufficient grid resolution to resolve the details of the flow.

The grid convergence study is not carried out for the third case of interest, i.e. for  $G/D = 1$  in order to avoid unnecessary high computational cost. The flow at  $G/D = 1$  belongs to the wide gap regime, the same as for  $G/D = 0.6$ . The sensitive interaction between the cylinder and the wall boundary layer subsides at large gaps, and the flow resembles the one around a cylinder in an infinite fluid, [7]. Therefore, both the previous experience of simulations with a cylinder in an infinite fluid at the same  $Re$ , [4], and the convergence study for the present  $G/D = 0.6$  case, are utilized to create the mesh for  $G/D = 1$ . A total of 9.8 million elements is distributed in the same manner as in the G06 1 case. The element size at the bottom wall and at the cylinder surface is kept the same as in all the previous cases, and additional elements are added in the gap between the cylinder and the wall.

Results for the convergence study of the time-step ( $\Delta t$ ) are presented in Table 2. It can be concluded that the refinement of the time-step does not lead to significant changes in  $St$  or the integrated forces on the cylinder.  $\overline{C_d}$  varies less than 5% between the smallest and the largest time-step,  $\overline{C_l}$  is changing about 10%, and  $St$  increases by 6% between the largest and the smallest time-step.

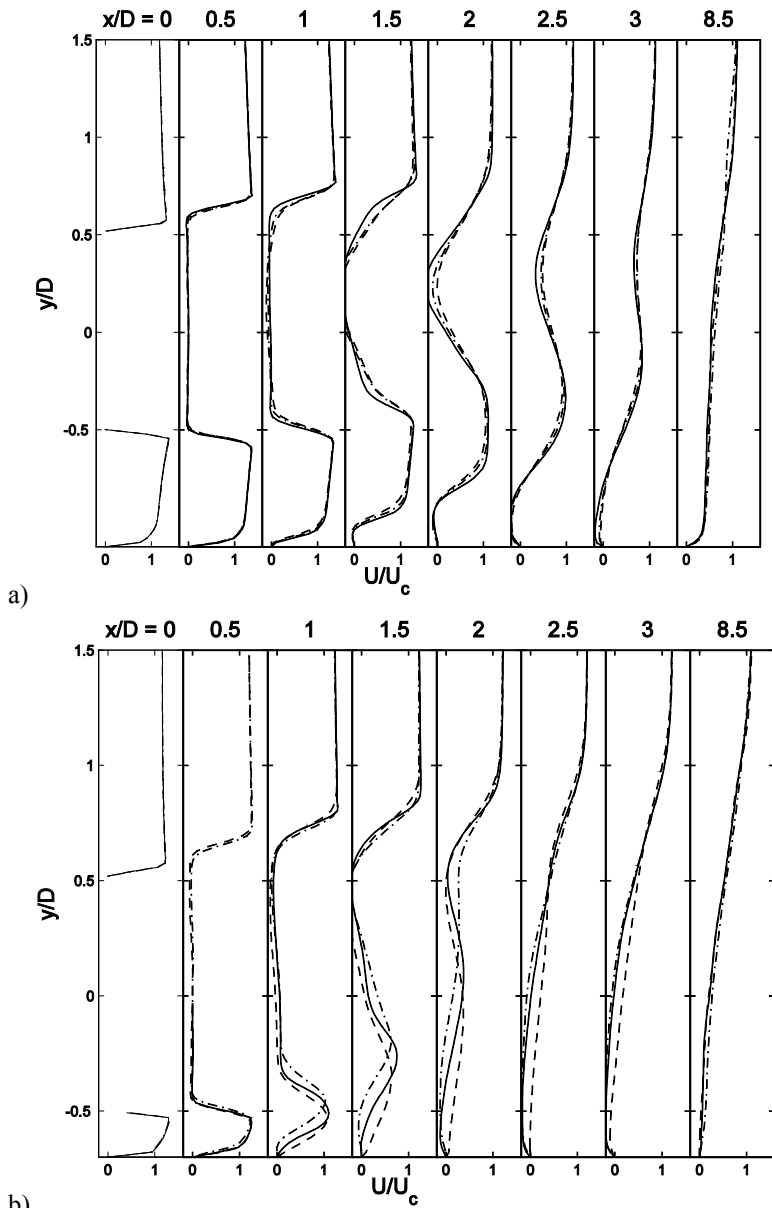


Figure 4.  $U/U_c$  across vertical cross-sections in the  $(y, z)$  plane of the cylinder wake. Grid convergence study.

- a)  $G/D = 0.6$ , symbols: --- G06 m1 (coarse), -.- G06 1, — G06 m2 (fine);
- b)  $G/D = 0.2$ , --- G02 m1 (coarse), -.- G02 m2, — G02 1 (fine).

The influence of the time-step is further investigated through the velocity profiles in the cylinder wake. The velocity field is sampled in the  $(x, z)$  plane, and averaged in the spanwise direction. Figure 5 shows that the differences between the

cases are small. It is therefore concluded that a time-step of 0.0001s is sufficient for the further analysis. Based on the current results and the previous experience published in [4], the results are not showing high sensitivity on the choice of time step. Therefore, we conclude that the time-step used in the G06 1 case is also fine enough for the cases with  $G/D = 0.2$  and 1.

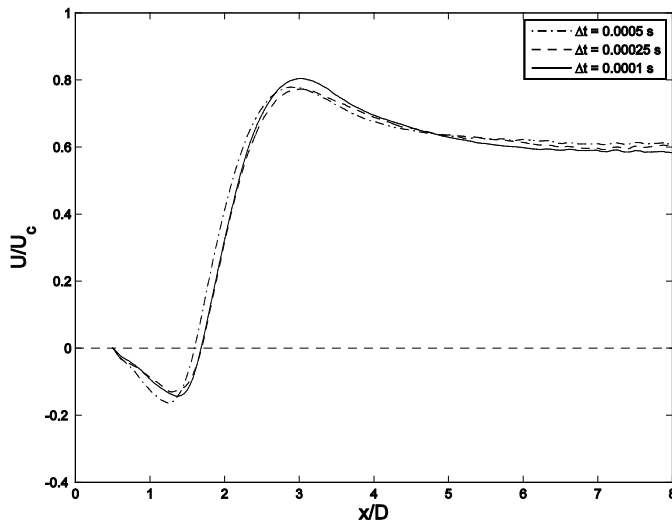


Figure 5.  $U/U_c$  in the cylinder wake, in the  $(x, z)$  plane,  $y/D = 0$  versus the time-step.  $G/D = 0.6$ ,  $\delta/D = 1.6$ .

Another computational parameter of importance for the 3D simulations is the spanwise ( $z$ ) width of the computational domain. For the case of the cylinder in an infinite fluid, the wake in the subcritical regime is varying along the cylinder span [25]. It forms cells, leading to the variations of the forces exerted on the cylinder. For a smooth cylinder with  $Re$  between 11000 and 45000, the cell length is measured to be between 3D and 6D, [25]. [26] conducted experiments at  $Re = 19000$  (comparable to the present study) and found the cell length to be approximately 3D, indicating the minimum domain width for the numerical simulations.

However, most of the previously performed numerical simulations of the flow in the vicinity of a plane wall were made with 2D models, see e.g. [22], [23]. In order to check the importance of the 3D effects at various  $Re$ , several simulations are performed with both two- and the three-dimensional domains. The simulations are performed at  $Re = 100, 500, 1000, 3900, 7800$  and 13100 for  $G/D = 0.6$ , using the same computational parameters and the criteria for the numerical mesh as described in Section 8.2. Details of the simulations are presented in Table 1.

For both  $Re = 100$  and  $500$ ,  $\overline{C_d}$  and  $C_{l_{rms}}$  of the 2D and 3D simulations differ with less than 1%, see Figure 6. This is in good agreement with the nature of the wake flow for such low  $Re$ , where  $Re < 300$  represents the laminar wake regime and  $Re = 500$  belongs to the very low subcritical regime, with negligible spanwise variability in both cases, see [25].

The 2D simulations, however, are shown not to be suitable for the flow at higher  $Re$  ( $Re \geq 1000$ ), where the flow is turbulent and 3D. While the 3D simulations capture decreasing  $\overline{C_d}$  for increasing  $Re$ ,  $\overline{C_d}$  obtained by the 2D simulations increase with increasing  $Re$  (see Figure 6a), progressively deviating from the 3D results. While the attenuation of the lift oscillations due to the presence of the wall is captured by the 3D simulations, the 2D cases give very high  $C_{l_{rms}}$  at high  $Re$  (Figure 6b). For  $Re = 13100$  (the highest in this study) the 3D simulations yield  $\overline{C_d} = 1.059$  and  $C_{l_{rms}} = 0.115$ , which are in good agreement with the previously published numerical and experimental results (see Section 8.4.1). However,  $\overline{C_d} = 1.695$  and  $C_{l_{rms}} = 1.408$  for the 2D simulations do not agree with the previous results. It is thus concluded that the 3D effects are crucial for the turbulent flow around the cylinder in the vicinity of the wall. 3D simulations also allow the analysis of the flow through the spatial distributions of the velocity and pressure fields, making them more comparable to the experimental studies (which are intrinsically 3D).

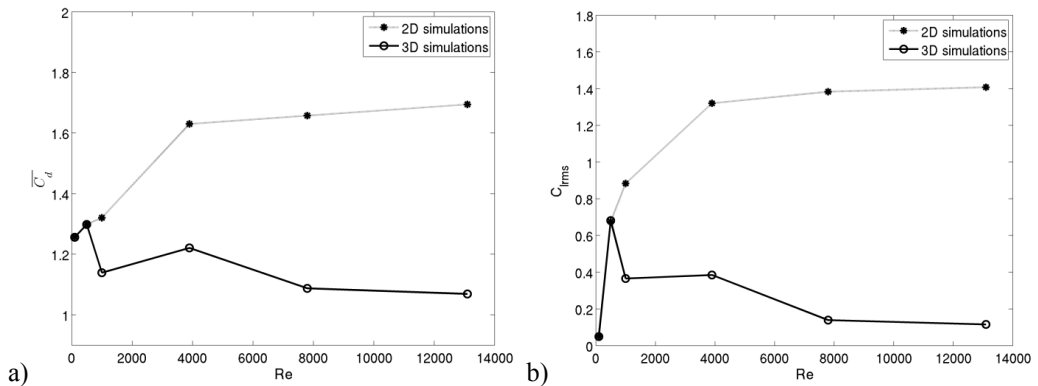


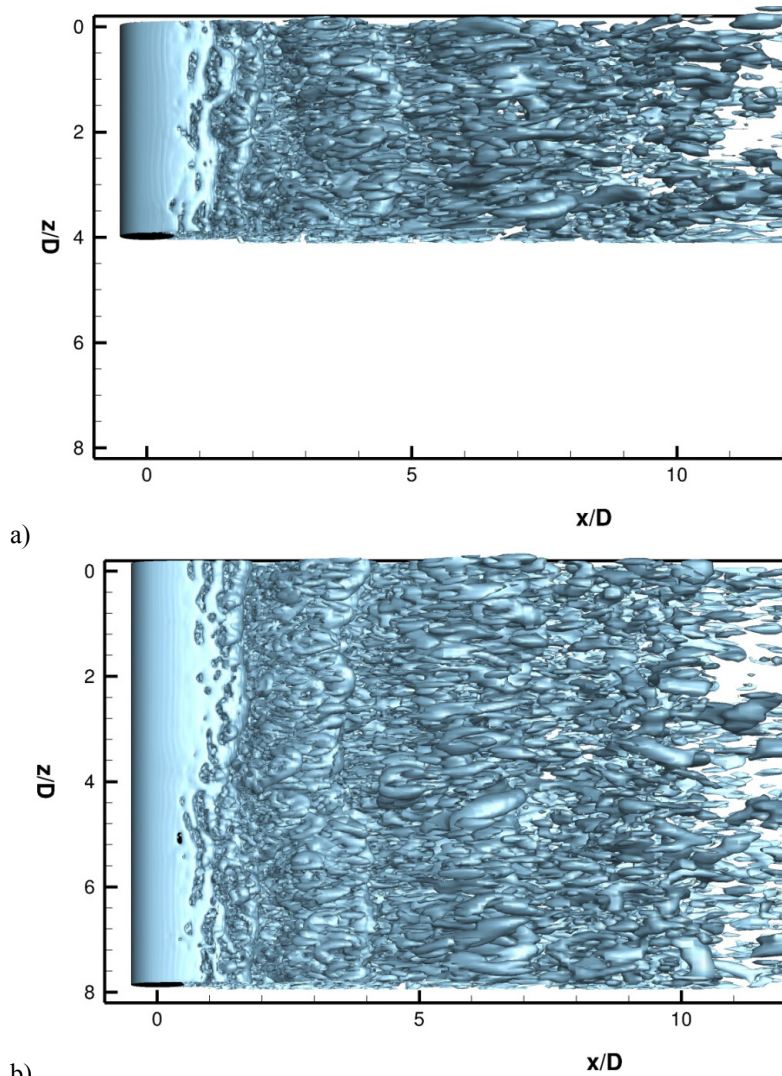
Figure 6.  $\overline{C_d}$  and  $C_{l_{rms}}$  versus  $Re$  – a comparison of 2D and 3D simulations.

By using a 3D LES, similar flow was successfully modelled in [27] with a three diameter wide domain in spanwise direction. The study was, however, done for the lower Re of 1400. Due to the limited numerical studies of this problem, the present domain width is chosen with reference to the previously published work for the case of the cylinder in an infinite fluid with same Re, [4]. In [4], the domain extended over 4D spanwise. For a comparable Re, [28] used a domain of 4D spanwise width, while a  $\pi D$  wide domain was used by [2], [3] and [19]. Thus the domain spanning over 4D is chosen here.

To check how well the spanwise structures are captured in the present case, the simulations were performed for 4D and 8D domain widths. The other numerical parameters are kept the same as for the converged case for  $G/D = 0.6$ , see Table 1. The visualization of the flow is done through the Q-criterion, a tool capable of depicting the coherent spanwise structures, [29]. In the 4D wide domain, cells of 3-4D length can be clearly detected (Figure 7a). This type of structures, of approximately same length, shows up also in the wider domain case, repeating twice over the cylinder span (Figure 7b). The flow around the cylinder in an infinite fluid [4] and in the vicinity of the wall show similar behaviour in the spanwise direction. Since the cells in both cases are approximately 3D long, the domain of 4D spanwise length is considered to be sufficient.

The time-averaged values, such as mean drag and lift coefficients are confirming the previous conclusion.  $\overline{C_d}$  differs for less than 2% between the 4D and the 8D cases, and St is almost identical for both cases. The lift coefficient also shows good resemblance in both mean and RMS values. It is therefore concluded that the spanwise length of 4D is wide enough for capturing the three-dimensional effects.





b)  
Figure 7. Examples of the instantaneous  $Q = 1$  iso-surfaces for the cylinders of different spanwise lengths.  $G/D = 0.6$ ,  $\delta/D = 1.6$ . a)  $L/D = 4$ , case G06 1; b)  $L/D = 8$ , case G06 L8. (Point of view is from above the cylinders.)

## 8.4. Results for the cylinder in the vicinity of a plane wall at

**$Re = 13100$**

The effect of  $G/D$  on the forces exerted on the cylinder, and the properties of the flow in the wake, are explored by choosing  $G/D = 0.2, 0.6$  and  $1$  (see Table 3).  $G/D = 0.2$  and  $1$  are chosen within the typical values for the narrow and the wide gap flow regime, while  $G/D = 0.6$  approaches the transient regime, [30]. In this way, the main types of flow around the cylinder in the vicinity of a plane wall are addressed.

The influence of  $\delta/D$  is investigated by choosing the values  $\delta/D = 0, 0.48$  and  $1.6$ , see Table 3. Here,  $\delta/D = 0$  corresponds to a uniform inlet velocity profile which, when approaching the cylinder, develops into a thin boundary layer with  $\delta/D < 0.2D$ . These  $\delta/D$  values are chosen to mimic the conditions at the seabed - a very thin boundary layer, the fully developed one, and a thick boundary layer caused by, for example, a bluff body obstacle, [11].

TABLE 3: Numerical set-up. Cylinder close to the wall at various  $G/D$  and  $\delta/D$ .  $\Delta t = 0.0001$ .

Case	$G/D$	$\delta/D$	Computational domain (x D)	Total number of elements (million)
G02 1	0.2	1.6	40 x 10.7 x 4	9.0
G06 1	0.6	1.6	40 x 11.1 x 4	9.5
G1 1	1	1.6	40 x 11.5 x 4	9.8
G06 i1	0.6	0	40 x 11.1 x 4	9.5
G06 i2	0.6	0.48	40 x 11.1 x 4	9.5

### 8.4.1. Influence of the gap ( $G/D$ )

Figure 8, presenting  $\overline{C_d}$  and  $C_{l_{rms}}$  for various  $G/D$ , agrees with both experimental and numerical results that recorded a decrease in  $\overline{C_d}$  as  $G/D$  narrows ([30]; [27]). [30] summarized that the wall proximity maintains its strong influence for small  $G/D$  ratios, leading to the complete disappearance of vortex shedding for the narrowest gaps. As  $G/D$  exceeds 1, this influence becomes insignificant and thus the flow behaves similar to the case of a cylinder in an infinite fluid.

TABLE 4: Cylinder close to the wall at various  $G/D$  and  $\delta/D$ . Mean flow parameters.

Key parameter	Case	$\overline{C_d}$	$\overline{C_l}$	$C_{lrms}$	St
$G/D$	G02 1	0.889	0.045	0.044	-
$G/D$	G06 1	1.060	0.083	0.115	0.278
$G/D$	G1 1	1.441	0.060	0.710	0.219
$\delta/D$	G06 i1	1.437	0.135	0.614	0.234
$\delta/D$	G06 i2	1.161	0.118	0.163	0.275

In Table 4 and Figure 8, the results are compared to the measurements of [11] who reported  $\overline{C_d} = 0.9$  at  $G/D = 0.2$ ,  $\overline{C_d} = 1.36$  at  $G/D = 0.6$  and  $\overline{C_d} = 1.42$  at  $G/D = 1$ . Comparison of the results for the narrow and the wide gap show very good agreement, within 5%. The differences in the  $G/D = 0.6$  case might be attributed to the different structures of the boundary layers. To obtain the boundary layer thickness of  $1.64D$ , [11] used rod-generated boundary layer. There, the velocity gradient closer to the wall was larger than in the naturally developed logarithmic profile. In [11], the variation of the mean drag coefficients showed sensitivity on the boundary layer structure. This influence can also be seen in the results for the widest gap,  $G/D = 1$ . For the case of a thinner, but naturally developed boundary layer, Lei et al. [11] measured  $\overline{C_d} = 1.43$ , very close to the present  $\overline{C_d} = 1.44$ . On the other hand,  $\overline{C_d} = 1.32$  from the rod-generated boundary layer agrees very well with  $\overline{C_d} = 1.31$  for the present study of the cylinder in the unbounded flow (Figure 8a). A very similar effect can be noticed on  $C_{lrms}$  in Figure 8b. Results for the small gap are again in good agreement while the widest gap results in [11] compare very well to the  $C_{lrms}$  values for the cylinder in an infinite fluid [4].

Zdravkovich [31] performed a series of experiments varying  $G/D$  in the wind tunnel, at  $Re = 61000$ . As presented in Figure 8a, the results show a similar trend as present, but with significantly lower values. According to [31], the measured drag coefficient was lower “presumably due to the small aspect ratio of the cylinders” used in the experiments.

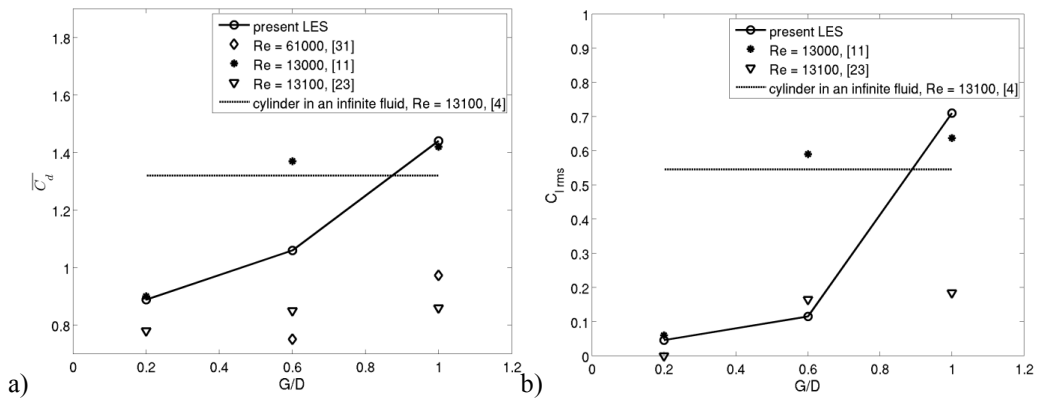


Figure 8.  $\overline{C_d}$  and  $C_{l,rms}$  versus  $G/D$ .

By comparing the present results to the previous ones from the numerical simulations, the significance of the 3D LES simulations becomes clear. The decrease in  $\overline{C_d}$  with the narrowing of the gap is almost completely absent in 2D RANS simulations with a  $k-\varepsilon$  model, [23], for the same  $Re$  (Figure 8a). At  $G/D = 0.2$ , the 2D and 3D results show reasonable agreement. Increasing the gap,  $\overline{C_d}$  in the 2D simulations remains low, 20% lower than the LES results at  $G/D = 0.6$  and 38% lower for  $G/D = 1$ . [32] faced similar shortcomings, using a  $k-\omega$  model and  $Re = 9000$ . On the other hand, [27] performed LES for  $G/D = 0.2$  and 1, for a lower  $Re = 1440$ . The flow at  $Re = 1440$  falls between two regimes, TRSL1 (Transition in shear layers – development of transition waves) and TRSL2 (Transition in shear layers – formation of transition eddies), while  $Re = 13100$  belongs to the latter one, [33]. Both  $Re$ , however, belong to the subcritical flow regime, with a fully turbulent wake and a laminar boundary layer separation, [25]. The results are in very good agreement with the present study.

$C_{l,rms}$  is a good indicator of the changes in the flow amplitude and regularity. Vortex shedding is significantly suppressed for  $G/D < 0.3$ , [30]. This is confirmed in the present study through a very low  $C_{l,rms}$  at  $G/D = 0.2$ . The present  $C_{l,rms}$  results are compared to the 2D RANS results by [23]. For  $G/D = 0.2$ , both models predict suppression of the regular vortex shedding. However, due to the very fine mesh resolution in the vicinity of the cylinder, LES are capturing the small  $C_l$  variations where the coarser RANS model does not capture any fluctuations at all ( $C_{l,rms} = 0$ , [23]). The results of the two models are in reasonable agreement for  $G/D = 0.6$ , while the largest discrepancies emerge at  $G/D = 1$  ([23] report  $C_{l,rms}$  at only 25% of the present value). The 2D simulations do not capture the strong increase in  $C_{l,rms}$  value at the larger gaps, confirmed by both the experiments and the present 3D simulations.

In agreement with [11], the fluctuations of the lift coefficient at  $G/D = 0.2$  confirm the existence of weak oscillations in the cylinder wake. The vortex shedding is, however, suppressed making the discussion of the Strouhal number for the smallest gap redundant. On the other hand, for  $G/D > 1$ , [30] expected that the  $St$  is unaffected by the presence of the wall ( $St \approx 0.21$ ). This compares well to the present study where  $St = 0.219$  for  $G/D = 1$ . In the wide gap regime, experimental results by [7], [9] and [11], as well as the numerical results of [23] and [27], show very good agreement with this study. For the narrower gaps, the  $St$  discrepancy is large. PIV measurements by [7] for  $Re = 4900$  and LES by [27] for low  $Re = 1440$  captured a decrease of  $St$  with increasing gap, similar to the present study. [11] also noticed an increase in the  $St$  for transient  $G/D$  around 0.5, however, with  $St < 0.2$  for any gap. On the other hand, for  $Re = 12000$ , [9] noticed almost no variation of  $St$  for  $G/D$  between 0.1 and 2, while [23] reported an increasing  $St$  with increasing  $G/D$ . To explore the origin of the discrepancy, the influence of the  $\delta/D$  ratio is discussed in Section 8.4.2.

Physical behaviour of the flow can be further explored by analysing the velocity profiles in the cylinder wake. The mean velocity profiles for all three  $G/D$  ratios are presented in Figure 9a. Within the first  $0.5D$  downstream from the cylinder centre, the flow behaviour is similar for all gaps. At  $x/D = 1$ , the profiles for the two wider gaps are nearly symmetric around the cylinder axis. The noticeable difference occurs in the area directly overshadowed by the cylinder ( $y/D$  between  $-0.5$  and  $0.5$ ). For  $G/D = 0.6$ , the velocities are still very low at the height of the cylinder, forming an 'u-profile' (see [15]) and pointing towards an elongated wake. On the other hand, the velocity profile for  $G/D = 1$  already resembles the classical 'v-profile' of the cylinder in an infinite fluid.

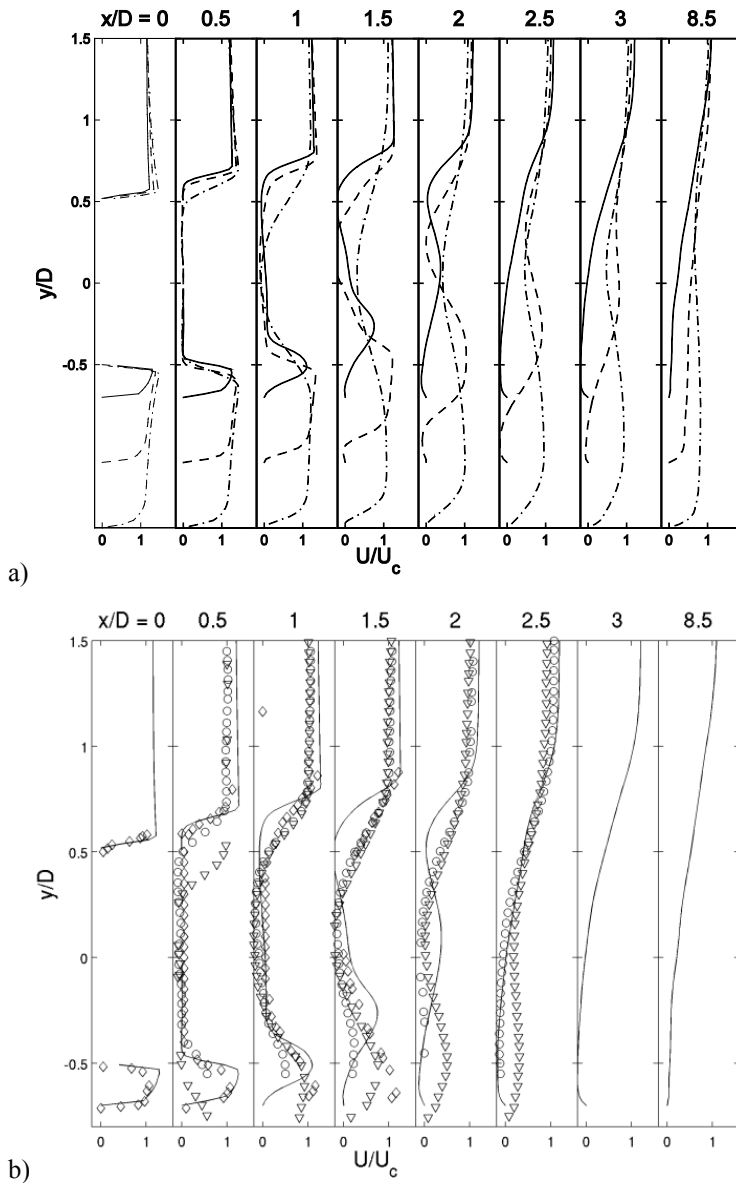


Figure 9.  $U/U_c$  profile in the cylinder wake, in the  $(y, z)$  plane.

a) —  $G/D = 0.2$ , - -  $G/D = 0.6$ , -·-  $G/D = 1$  (present).

b) —  $G/D = 0.2$  (present);

o  $G/D = 0.1$ ,  $\delta/D = 0.4$ ,  $Re = 1.2 \times 10^4$ , Wang and Tan [9];  $\diamond$   $G/D = 0.2$ ,  $\delta/D = 1.4$ ,  $Re = 0.95 \times 10^4$ , Alper Oner et al. [8];  $\nabla$   $G/D = 0.3$ ,  $\delta/D = 0.4$ ,  $Re = 1.2 \times 10^4$ , Wang and Tan [9].

Farther downstream in the wake, the velocity profiles for  $G/D = 1$  retain symmetry. This behaviour is documented in previous studies, [8], [9]. The bottom boundary layer eventually assumes its original shape, while the velocities in the area overshadowed by the cylinder continue to form the 'v-profile' far back in the wake. At  $G/D = 0.6$ , the velocities at  $-0.5 < y/D < 0.5$  develop the 'v-profile' at  $x/D = 1.5$  and retain a relatively symmetric profile. [9] documented a very similar wake behaviour measured by PIV. A significant difference between the flow at  $G/D = 0.6$  and 1 is the recirculation area developed for the smaller gap. While relatively thin, it extends between  $x/D = 1.5$  and 3 (see Figure 9a). As the gap becomes even smaller, the recirculation area becomes more prominent, covering a significantly longer and thicker layer. Time-averaged streamlines shown in Figure 10 give a confirmation of these zones, revealing that the one for  $G/D = 0.2$  extends more than  $6D$  downstream in the wake. The downstream wall boundary layer is forced to separate because the streamlines in the inner shear layer become deflected away from the wall. [9] captured the recirculation only for a gap as narrow as  $0.1D$ . Also measured by PIV, [8] reported such wall separation for  $G/D \leq 0.6$ , while LES results in [27] showed this behaviour for  $G/D = 0.25$  and  $0.5$ .

In Figure 9b, the present results are compared to the measurements of [8] for  $G/D = 0.2$  and [9] for two comparable gaps,  $G/D = 0.1$  and  $0.3$ . [8] performed PIV measurements for  $Re = 9500$ , with the boundary layer thick enough to have the entire cylinder immersed in it ( $G/D = 1.4$ ), comparable to the present simulations. Figure 9b shows very good agreement of the experimental and the present LES results in the near wake of the cylinder, confirming that the complex flow in the narrow gap between the cylinder and the wall is modelled correct. The discrepancies can first be noticed at  $x/D = 1$ , showing that LES yield a somewhat more upwards deflected wake.

[9] reported that such small  $G/D$  as  $0.1$  does not allow the development of the channelled flow below the cylinder. On the other hand, at  $G/D = 0.3$ , the velocity profile shows channelled flow farther downstream in the wake than for the present case. Qualitatively, the flow features are similar to the present study. The differences in the near wall flow might be attributed to a stronger interaction between the wall and the cylinder boundary layer for the smaller  $G/D = 0.2$  in this study, as well as to the different  $\delta/D$ . Comparing their results to the previously published studies ([34] and [35]), [9] measured significantly smaller wake velocities. It is therefore important to have in mind the differences of the various experimental and numerical parameters, while recognizing the similar qualitative behaviour.

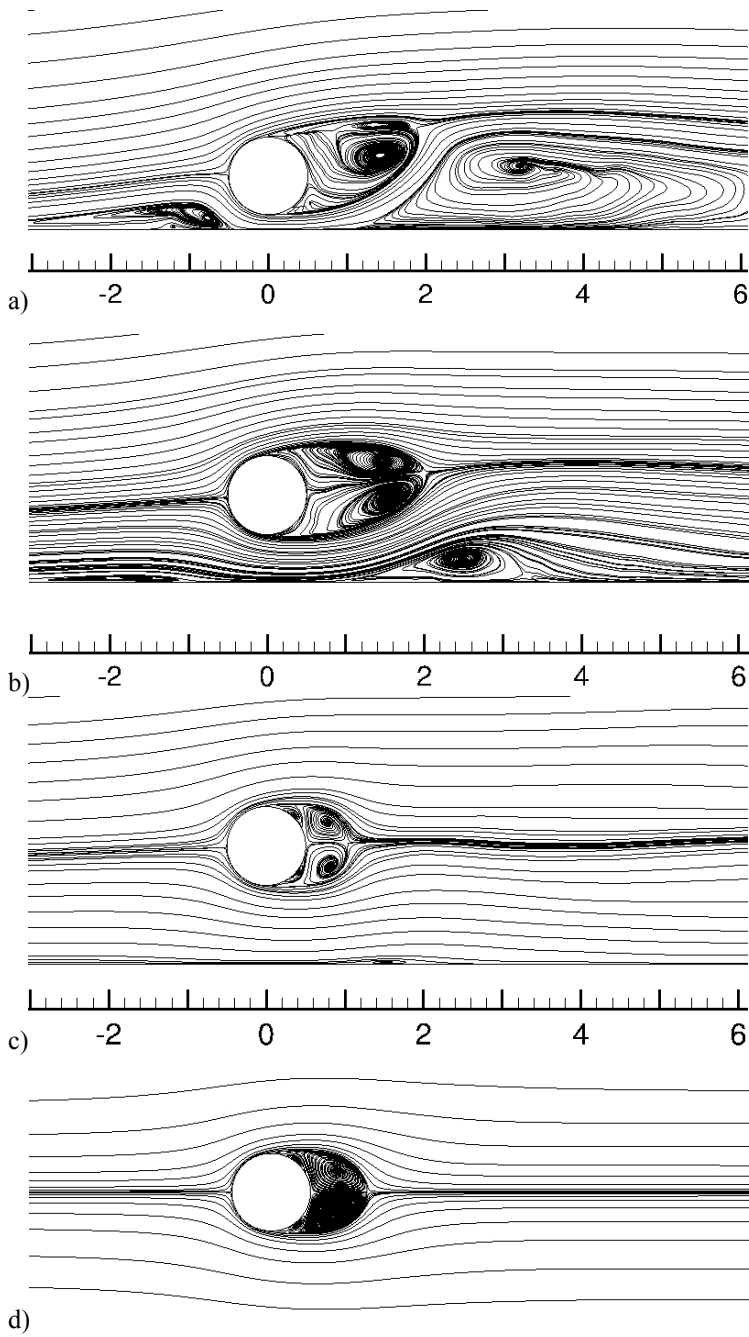


Figure 10. Time-averaged streamlines at  $z/D = 2$  for  $G/D = 0.2, 0.6$  and  $1$  at  $\delta/D = 1.6$ . Cases a)  $G02\ 1$ , b)  $G06\ 1$ , c)  $G1\ 1$  and d) cylinder in an infinite fluid ( $Re = 13100$ , Abrahamsen Prsic et al. [4]).



The distributions of the time-averaged streamlines for different  $G/D$  (Figure 10) show a clear distinction between the narrow and the wide gap regime. For  $G/D = 0.2$  (Figure 10a), the flow behaves in the same manner as described by [27] and [30]. The flow upstream of the cylinder is characterized by a prominent separation region. Downstream, the flow accelerates between the wall and the cylinder. The coupling between the bottom boundary layer and the shear layer at the lower side of the cylinder causes the deflection of the primary bubble away from the wall. Similar to the observations by [27], Figure 10a shows the strong asymmetry between the vortices curling up from the upper and the lower side of the cylinder. The whole primary bubble is relatively long and deflected upwards, leading to the formation of a large secondary bubble at the wall.

As the gap increases to  $G/D = 0.6$  (Figure 10b), the upstream separation region reduces to a thin area. This shorter and flatter upstream region is also reported by [7]. The primary bubble, even though more symmetric, is still long and deflected from the wall. It allows the secondary recirculation to develop on the wall, but only in a small region in the near wake of the cylinder. The flow undergoes even more significant changes as the gap reaches  $G/D = 1$  (Figure 10c), when the wall effect begins to cease. This is manifested through the disappearance of both the upstream and the downstream separation region, also reported by [27]. The primary separation bubble becomes symmetric and shortens to the size of the one behind a cylinder in an infinite fluid, also documented by [9]. Overall similarity of this wide gap flow and the flow around a cylinder in an unlimited fluid is shown in Figure 10c and 10d.

Through the experiments in the smoke tunnel, [10] photographed the flow behind the cylinder at  $G/D = 0.2$  and  $1.2$ , at  $Re = 45000$  (Figure 11a and 11b). The photographs are compared to the instantaneous streamlines at the cylinder mid-section for the cases  $G/D = 0.2$  and  $1$  (Figure 11c and 11d). This comparison gives an example that the experimental and the numerical results are complementary. While the experimental results offer a clear and trustworthy overview of the dynamic flow phenomena, the nature of the smoke tunnel experiments does not allow capturing the fine structures in the cylinder wake. On the other hand, while agreeing with the experiments, LES also provide a unique detailed insight in the fine structures in the cylinder wake.

At  $G/D = 0.2$ , both the experimental and the numerical results show that the vortices in the near wake are restricted to the upwards deflected separation bubble. The length of the primary bubble as well as the position of the secondary bubble from this study compare well with [10], see Figure 11a and 11c. The similarity of the instantaneous and the time-averaged streamlines (Figure 10a and 11c) confirms that there are only slight variations of the wake with time. On the other hand,  $G/D = 1$  and

1.2 allow for the vortex street to develop, as captured both by the experiments and the LES. Figures 11b and 11d show clear similarity, with comparable size and shape of the vortices in the cylinder wake.

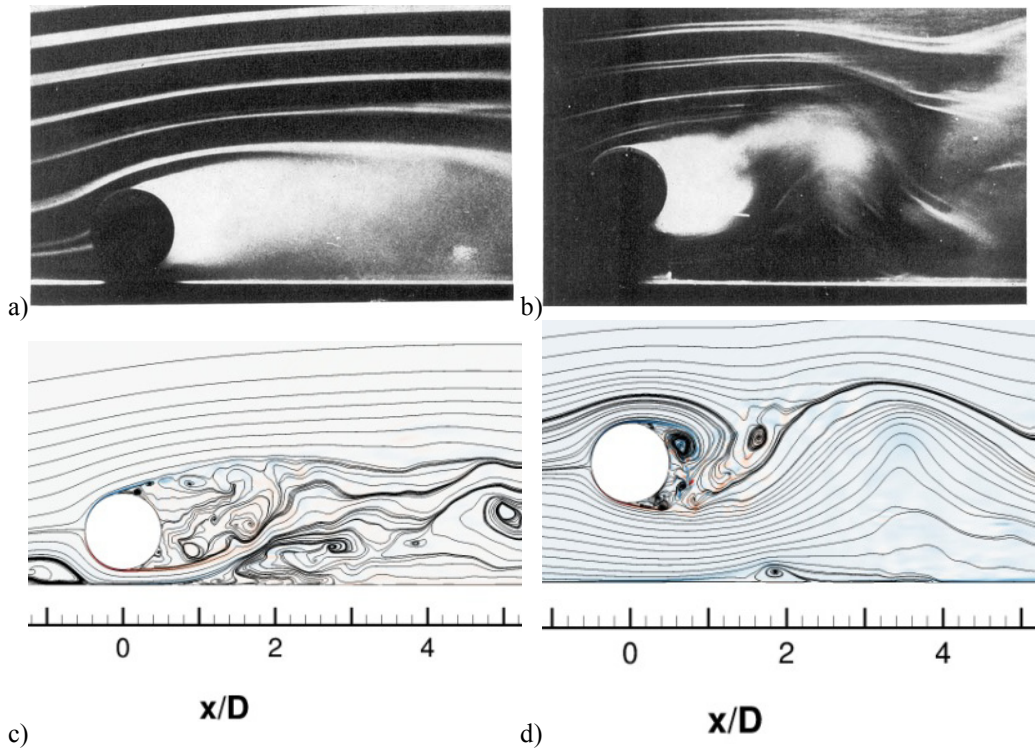


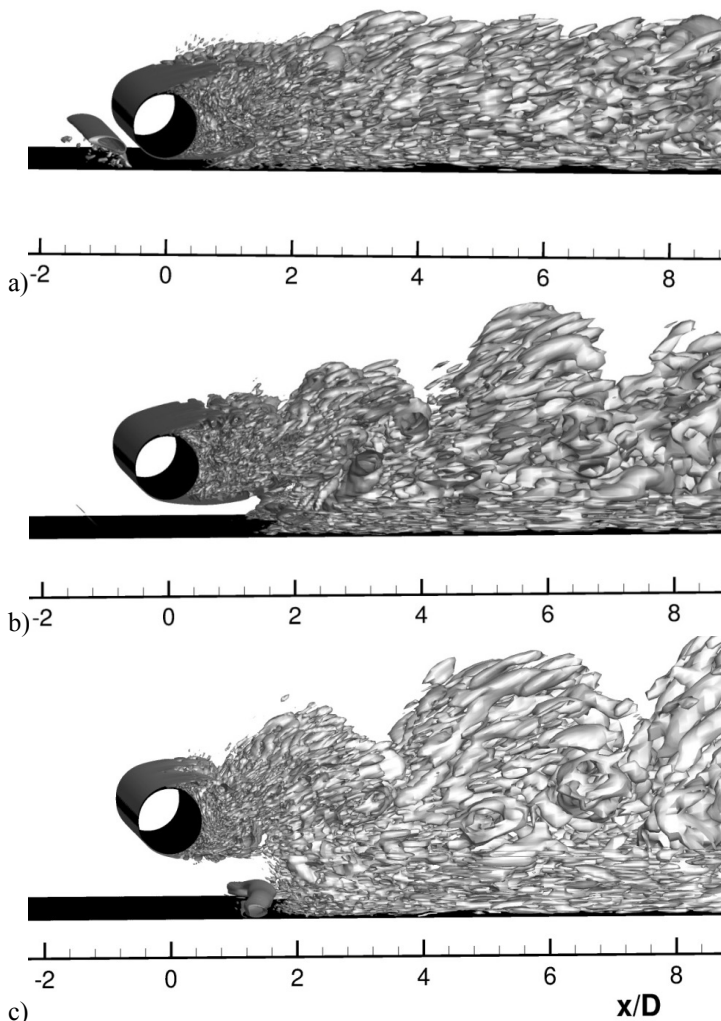
Figure 11. Instantaneous flow pattern. Figures 11a and 11b are taken from Bearman and Zdravkovich [10]. The wind tunnel measurements are performed for  $Re = 2.5 \times 10^4$ .

- e)  $G/D = 0.2$ .
- f)  $G/D = 1.2$ .
- g)  $G/D = 0.2$ . Present study, case G02 1.
- h)  $G/D = 1$ . Present study, case G1 1.

The instantaneous streamlines presented in 11c and 11d are taken at cylinder mid-plane,  $z/D = 2$  for  $Re = 1.31 \times 10^4$  and  $\delta/D = 1.6$ .

The instantaneous  $Q = 1$  iso-surfaces offer an insight into the development of the three-dimensional vortex structures in the cylinder wake. The inhibition of the vortex shedding for  $G/D = 0.2$  is clearly shown in Figure 12a. The upper shear layer extends relatively far into the wake, while the lower shear layer deflects from the wall. The resulting long separation region is also detectable in Figure 12a. In the cylinder wake, no signs of large coherent structures are observed; the small scale eddies dominate the wake flow. The wall separation region is also present.

As the gap increases, the von Karman vortex street, dappled with smaller eddies, is observed in Figures 12b and 12c. The upper shear layers become shorter. For the large gap, the shear layers shed and curl up on both sides of the cylinder, creating a regular vortex shedding pattern. However, at  $G/D = 0.6$ , the lower part of the cylinder is affected by the gradients in the wall boundary layer. In agreement with [13], the boundary layer interacts with the vortices shed from the lower half of the cylinder. They travel downstream at lower speed, experiencing more damping than the ones shed from the upper half of the cylinder. While deformation of the vortices in the vicinity of the wall is also noticeable for the largest gap (Figure 12c), stronger symmetry and coherence indicate a significant weakening of the wall influence.



c) Figure 11. Instantaneous  $Q = 1$  iso-surfaces for  $G/D = 0.2, 0.6$  and  $1$ . Cases a) G02 1, b) G06 1 and c) G1 1 at  $\delta/D = 1.6$ . The spanwise length of the cylinder is  $4D$ .

The suppression of the vortex shedding is analysed through the energy spectra sampled in the near wake of the cylinder for  $G/D = 0.2, 0.6$  and  $1$  (Figure 13).  $G/D = 1$  allows the vortex shedding to fully develop, resulting in a single, prominent peak of the energy spectrum, corresponding to  $St$ . For  $G/D = 0.6$ , the energy spectrum has maximum at a frequency slightly higher than for  $G/D = 1$  and for a cylinder in infinite fluid [4], [15]. The maximum is, however, less prominent, confirming the previous conclusion about the attenuation of the vortex shedding. The complete absence of the regular von Karman vortex street for  $G/D = 0.2$  is confirmed in Figure 13.

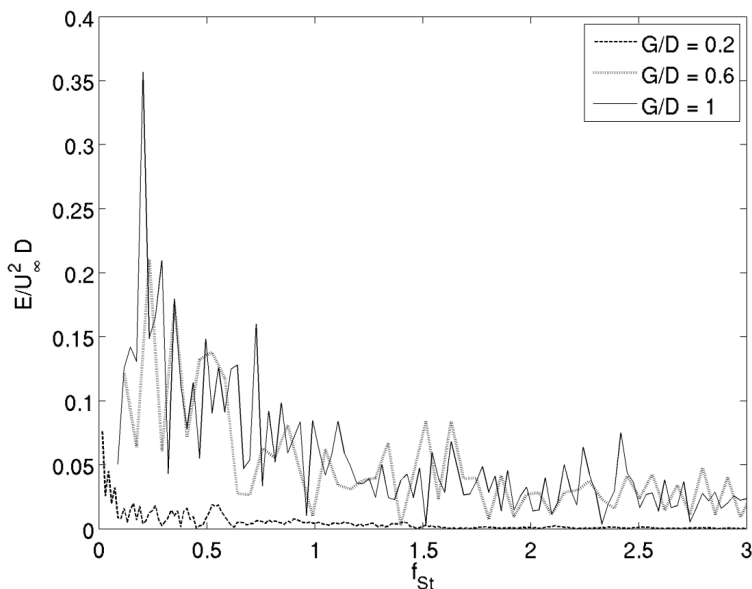


Figure 13. Energy spectra in the cylinder wake, sampled at  $x/D = 1, y/D = 0.3, z/D = 0$ . The normalized Strouhal frequency is given as  $f_{St} = fD/U_c$ .

#### 8.4.2. Influence of incoming boundary layer thickness $\delta/D$

The flow dependency on the thickness of the incoming boundary layer profile is examined through three simulations with constant  $G/D = 0.6$ , and varying  $\delta/D$  (see Table 3). The logarithmic profile is chosen to simulate a developed boundary layer profile near a flat, rigid wall.

Contrary to the extensive number of studies investigating the influence of  $G/D$ , data available on the influence of  $\delta/D$  is scarce. [31] conducted a series of experiments for a higher  $Re$  varying between 48000 and 140000. This  $Re$  range is, however, in the same flow-regime as the present study. The analysis was focused on the gap to

boundary layer thickness ratio,  $G/\delta$ , showing that  $\overline{C_d}$  decreases as  $G/\delta$  decreases below 1 and maintains a slowly increasing trend for  $G/\delta > 1$ . For  $Re = 61000$ , [31] obtained  $\overline{C_d} = 0.64, 0.96$  and  $1.05$  for  $\delta/D = 0.4, 1.2$  and  $2$ , respectively. While the present  $\overline{C_d}$  values are higher for all  $\delta/D$ , the same trend is observed (Figure 14a). The present values are in better agreement with the experimental study by [11] at a closer  $Re = 13000$ , as shown in Figure 14a.

$C_{l_{rms}}$  also decreases with increasing boundary layer thickness (Figure 14b). For the thinnest boundary layer, both  $\overline{C_d}$  and  $C_{l_{rms}}$  behave comparable to the cylinder in an infinite fluid. As the boundary layer thickens, the gap and the cylinder itself get immersed into the bottom boundary layer, leading to lower  $C_{l_{rms}}$ . [11] and [31] report a similar trend for the  $C_{l_{rms}}$ , showing a prominent decrease as the cylinder becomes immersed in the boundary layer.

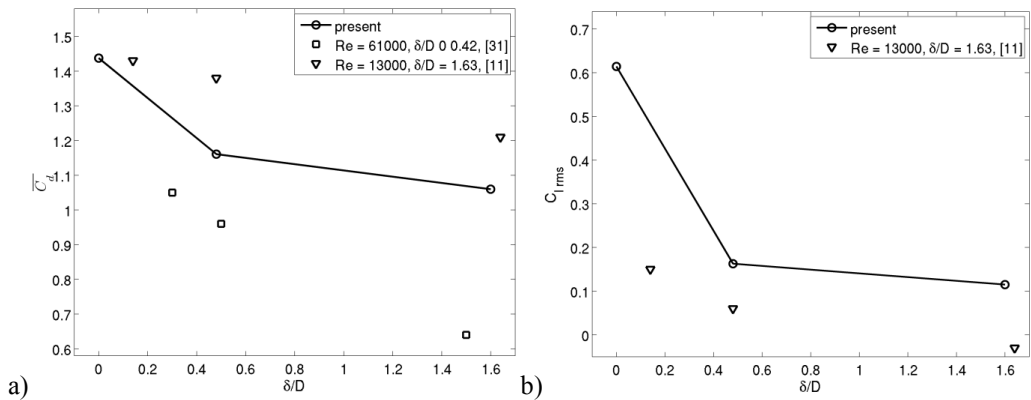


Figure 14:  $\overline{C_d}$  and  $C_{l_{rms}}$  versus  $\delta/D$  for  $G/D = 0.6$ .

The mean pressure coefficient ( $\overline{C_p}$ ) distribution is analysed in Figure 15;  $\overline{C_p}$  is the time- and spanwise-averaged pressure coefficient, and  $C_p = (p' - p_\infty)/(0.5\rho U_c^2)$ , for the fully developed flow. Here  $p'$  is the instantaneous pressure at the sampling point, and  $p_\infty$  is the pressure in the undisturbed flow. Here  $\theta = 0$  corresponds to the point at the cylinder closest to the wall and  $\theta$  increases clockwise (see Figure 1).

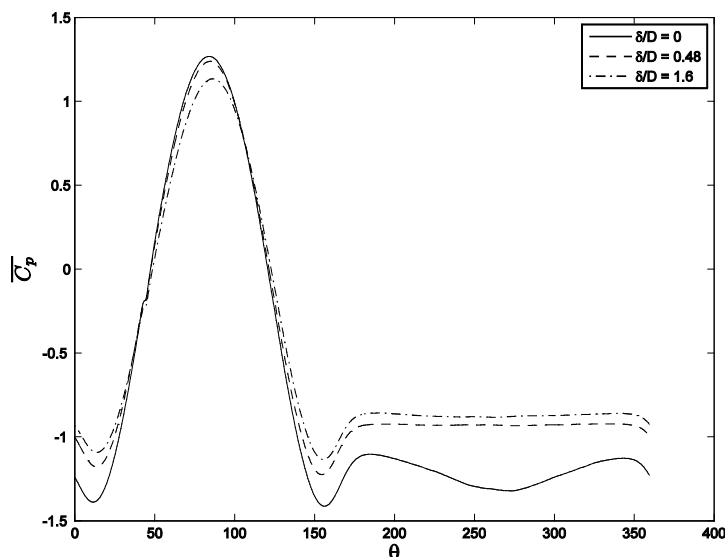


Figure 15.  $C_p$  distribution versus  $\delta/D$  ratio for  $G/D = 0.6$ . The angle  $\theta$  is defined in Figure 1.

A thinner boundary layer leads to a more pronounced maximum in  $\overline{C_p}$ . This behaviour is also reported by [11], who connected it to the exposure of the gap to the velocity gradient in the boundary layer. Exposure to the gradient can also be obtained by decreasing  $G/D$ , causing a similar effect. The decrease of the  $\overline{C_p}$  peak with a reduced gap is documented by [12] and [23]. The thickening of the wall boundary layer causes an increase of the base pressure. In the entire  $\overline{C_p}$  profile, Figure 15 shows the largest increase from the thinnest ( $\delta/D = 0$ ) to the intermediate ( $\delta/D = 0.48$ ) boundary layer, while further thickening of  $\delta/D$  results in smaller increase of the magnitude.

Mean velocity profiles in the cylinder wake are presented in Figure 16a. In the near wake ( $x/D = 0$  to 1), all three cases with different boundary layers exhibit similar profiles. Farther downstream, the two cases with thicker boundary layers behave similarly, maintaining a significant profile curvature up to  $x/D = 3$ . The thinnest boundary layer results in symmetric, but earlier flattened wake profile, indicating a shorter wake. The present results are compared with the PIV measurements, [9], for the same  $G/D = 0.6$ , comparable  $\delta/D = 0.4$  and  $Re = 12000$ . The qualitative behaviour of the profiles is similar, exhibiting the symmetry, the relatively late flattening of the profiles, and the transition from the characteristic 'u-' to 'v-profile'. However, all measurements for the various cases presented by [9] result in smaller velocities compared to the previously published and the present results. The focus is therefore on the qualitative comparison.

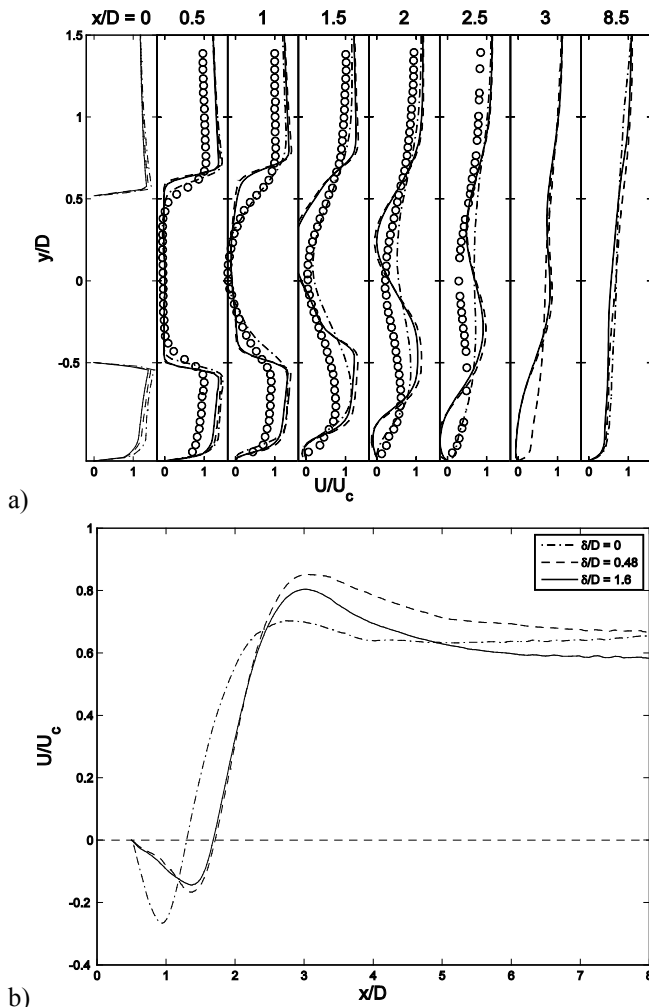


Figure 16. Mean, normalized streamwise velocity component ( $U/U_c$ ) in the cylinder wake,  $G/D = 0.6$

- a) in the  $(y, z)$  plane. Present study and “o”  $\delta/D = 0.4$ ,  $Re = 1.2 \times 10^4$ , Wang and Tan [9];
- b) in the  $(x, z)$  plane,  $y/D = 0$  versus the  $\delta/D$ , present study.

The analogy between the reduced thickness of the boundary layer and the widening of the gap can also be noticed in Figure 16b. While the near wakes for the two thicker boundary layers exhibit longer recirculation lengths and somewhat higher velocities, the wake profile of the thinnest boundary layer shows more resemblance with the one of the cylinder at large  $G/D$ . Comparison of the time-averaged streamlines for these three  $\delta/D$  cases at  $G/D = 0.6$  (Figure 17) with the wide gap,  $G/D = 1$  (Figure 10c) and the cylinder in the infinite fluid (Figure 10d) further confirms this. For  $\delta/D = 0$  (Figure 17a), the upstream separation region vanishes while the downstream region is

reduced. However, the presence of the wall still causes the deflection of the wake away from the wall, for  $G/D = 0.6$ . The thicker boundary layers engulf the channel between the cylinder and the wall, allowing the fluid particles to accelerate and eventually cause the upturn of the boundary layer. This results in longer primary bubbles and the prominent downstream separation zones for both  $\delta/D = 0.48$  (Figure 17b) and  $\delta/D = 1.6$  (Figure 17c).

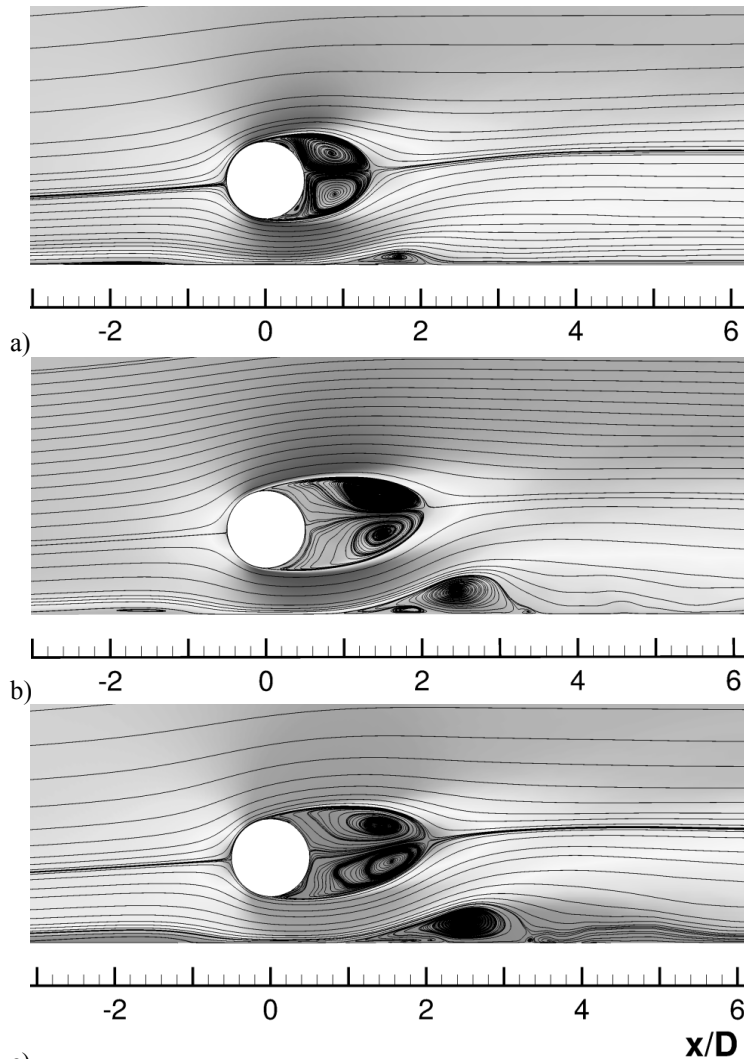


Figure 17. Time-averaged streamlines and  $U/U_c$  at  $z/D = 2$ .  $\delta/D = 0, 0.48$  and  $1.6$ ,  $G/D = 0.6$  in all cases.



## 8.5. Conclusions

Near-wall flow effects on a circular subsea pipeline in the vicinity of the seabed at  $Re = 13100$  are investigated by LES with Smagorinsky sub-grid scale model. The effects of the distance between the cylinder and the seabed, and the bottom boundary layer thickness, on the forces exerted on the cylinder and the flow field in the cylinder wake, are presented. The main conclusions are:

The gap to diameter ratio,  $G/D$ , has a strong influence on the forces on the cylinder and the development of the flow in the wake. For  $G/D$  smaller than the critical gap, the vortex shedding is suppressed, noticed in the present study for  $G/D = 0.2$ . Increasing  $G/D$ , asymmetric vortex shedding develops (demonstrated for  $G/D = 0.6$ ). Due to the reduced interaction between the wall and the cylinder boundary layer for the larger  $G/D = 1$ , the wake flow approaches the behaviour of a cylinder in an infinite fluid and uniform incoming velocity field.

By varying  $G/D$ , different aspects of the flow are displayed:

- a) For  $G/D = 0.2$ , both the primary and the secondary separation bubble are long and nearly stationary.
- b) The intermediate  $G/D = 0.6$  yields a slightly asymmetric wake, with long shear layers. The vortex shedding is limited and the secondary circulation at the wall boundary layer is substantial.
- c) The large  $G/D = 1$  allows a symmetric near wake (with respect to x-axis), while eddies interact with the wall farther in the wake. The cylinder shear layers and the wall boundary layer separate periodically.

Although the presence of the plane wall has the strongest influence on the general flow characteristics, it also depends on the boundary layer thickness to diameter ratio,  $\delta/D$ , and the shape of the boundary layer. Effects of a thicker boundary layer are similar to the effects of decreasing  $G/D$ . For  $G/D = 0.6$ , if the cylinder is not immersed in the boundary layer, the flow resembles the one around the cylinder in an infinite fluid. Larger  $\delta/D$ , where the cylinder is subjected to the shear flow, results in lower  $\overline{C_d}$  and  $C_{l_{rms}}$ , as well as an elongated and asymmetric wake.

Comparison of the present results with the experimental measurements shows that LES are a good numerical tool for the actual flow case. The 3D simulations also complement the experiments, offering insight into the detailed structures in the cylinder wake and allowing thorough exploration of the three-dimensional flow

behaviour. 3D LES offer clear improvements compared to the commonly used simple 2D RANS models as well as to 2D LES, giving more reliable integrated forces and capturing the details of the flow at different  $G/D$  and  $\delta/D$ , important for the structural analysis of the pipeline.

### ***Acknowledgements***

This work has been supported by the Norwegian University of Science and Technology (NTNU). Computing time on the supercomputer 'Vilje', supported by NOTUR (the Norwegian Metacenter for Computational Science) is granted by the Norwegian Research Council and NTNU. This support is gratefully acknowledged.

## References

- [1] Breuer, M., 1998. Large eddy simulation of the subcritical flow past a circular cylinder: numerical and modeling aspects. *International Journal for Numerical Methods in Fluids*, 28, 1280-1302.
- [2] Tremblay, F., Manhart, M., Friedrich, R., 2000. DNS of flow around the circular cylinder at subcritical Reynolds number with Cartesian grids. *Proceedings of the 8<sup>th</sup> European Turbulence Conference, EUROMECH, Barcelona, Spain, 659-662.*
- [3] Parnaudeau, P., Carlier, J., Heitz, D., Lamballais, E., 2008. Experimental and numerical studies of the flow over a circular cylinder at Reynolds number 3900. *Phys. Fluids* 20, 085101.
- [4] Abrahamsen Prsic, M., Ong, M. C., Pettersen, B., Myrhaug D., 2014. Large-eddy simulations of three dimensional flow around a smooth circular cylinder in a uniform current in the subcritical flow regime. *Ocean Engineering*, 77, 61-73.
- [5] Knight, P. J., Wilkinson, M., Glorioso, P., 1993. Current profile and sea-bed pressure and temperature records from the northern North Sea. *Challenger Cruises 84 and 85. September 1991 - November 1991. Birkenhead, Proudman Oceanographic Laboratory, 417pp. Proudman Oceanographic Laboratory, Report No. 28.*
- [6] Offshore standard Det Norske Veritas as Dnv-Os-F101; Submarine pipeline systems. Det Norske Veritas, August 2012.
- [7] Price, S. J., Sumner, D., Smith, J. G., Leong, K., Paidoussis, M. P., 2002. Flow visualization around a circular cylinder near to a plane wall. *Journal of Fluids and Structures*, 16(2), 175-191.
- [8] Alper Oner, A., Salih Kirgoz, M., Sami Akoz, M., 2008. Interaction of a current with a circular cylinder near a rigid bed. *Ocean Engineering*, 35, 1492-1504.
- [9] Wang, X. K., Tan, S. K., 2008. Comparison of flow patterns in the near wake of a circular cylinder and a square cylinder placed near a plane wall. *Ocean Engineering*, 35, 458-472.
- [10] Bearman, P. W., Zdravkovich, M. M., 1978. Flow around a circular cylinder near a plane boundary. *Journal of Fluid Mechanics*, 89, 33-47.
- [11] Lei, C., Cheng, L., Kavanagh, K., 1999. Re-examination of the effect of a plane boundary on force and vortex shedding of a circular cylinder. *Journal of Wind Engineering and Industrial Aerodynamics*, 80, 263-286.
- [12] Han, Y., Shi, B., Ren, X., Jing, X., 2009. Experimental study on the distribution of velocity and pressure near a submarine pipeline. *J. Ocean Univ. China (Oceanic and Coastal Sea Research)*, 8(4), 404-408.
- [13] Brørs, B., 1999. Numerical modelling of flow and scour at pipelines. *Journal of Hydraulic Engineering*, 125 (5), 511-523.
- [14] Ong, M. C., Utne, T., Holmedal, L. E., Myrhaug, D., Pettersen, B., 2010. Numerical simulation of flow around a circular cylinder close to a flat seabed at high Reynolds numbers using a k- $\epsilon$  model. *Coastal Engineering*, 57 (10), 931-947.
- [15] Lysenko, D. A., Ertesvåg, I. E., Rian, K. E., 2012. Large-eddy simulation of the flow over a circular cylinder at Reynolds number 3900 using the OpenFOAM toolbox. *Flow Turbulence Combust.* 89, 491-518.
- [16] Liou, T.-M., Chen, S.-H., Hwang, P.-W., 2002. Large eddy simulation of turbulent wake behind a square cylinder with nearby wall. *Journal of Fluids Engineering*, 124, 81-90.

- [17] Boileau, M., Duchaine, F., Jouhaud, J.-C., 2013. Large-Eddy Simulation of heat transfer around a square cylinder using unstructured grids. *AIAA Journal*, 51 (2), 372-385.
- [18] Smagorinsky, J., 1963. General circulation experiments with the primitive equations. *Monthly Weather Review*, 91 (3), 99-164.
- [19] Breuer, M., 2000. A challenging case for large eddy simulation of high Reynolds number circular cylinder flow. *International Journal of Heat and Fluid Flow*, 21, 648-654.
- [20] Ferziger, J. H., Peric, M., 2002. *Computational methods for fluid dynamics*. 3rd Ed, Springer-Verlag, Berlin, Germany.
- [21] Krajnovic, S., 2011. Flow around a tall finite cylinder explored by large eddy simulation. *Journal of Fluid Mechanics* 676, 294–317.
- [22] Liang, D., Cheng, L., 2005. Numerical modeling of flow and scour below a pipeline in currents; Part 1. Flow simulation. *Coastal Engineering*, 52, 25-42.
- [23] Ong, M. C., Utnes, T., Holmedal, L. E., Myrhaug, D., Pettersen, B., 2012. Near-bed flow mechanisms around a circular marine pipeline close to a flat seabed in the subcritical flow regime using a  $k - \epsilon$  model. *Journal of Offshore Mechanics and Arctic Engineering*, 134 (2), 021803.
- [24] ASME V&V 20, 2009. *Standard for Verification and Validation in Computational Fluid Dynamics and Heat Transfer*. ASME, New York, USA.
- [25] Sumer, B. M., Fredsøe, J., 2006. *Hydrodynamics Around Cylindrical Structures*, Revised Edition. *Advanced Series on Ocean Engineering*, World Scientific Publishing, Singapore.
- [26] Novak, M., Tanaka, H., 1977. Pressure correlations on a vibrating cylinder. *Proc. 4th Int. Conference on Wind Effects on Buildings and Structures*, Heathrow, UK., Ed. By Eaton., K. J. Cambridge University Press, pp. 227-232.
- [27] Sarkar, S., Sarkar, S., 2010. Vortex dynamics of a cylinder wake in proximity to a wall. *Journal of Fluids and Structures*, 26, 19-40.
- [28] Wissink, J. G., Rodi, W., 2008. Large-scale computations of flow around a circular cylinder in Resch, M., Roller, S., Lammers, P., Furui, T., Galle, M., Bez, W. 2008. *High Performance Computing on Vector Systems*. Springer-Verlag, Berlin Heidelberg, Germany.
- [29] Lesieur, M., Metais, O., Comte, P., 2005. *Large-Eddy Simulations of Turbulence*. Cambridge University Press, New York, USA.
- [30] Zdravkovich, M. M., 2009. *Flow around circular cylinders. Vol.2: Applications*. Oxford University Press, Oxford, United Kingdom.
- [31] Zdravkovich, M. M., 1985. Forces on a circular cylinder near a plane wall. *Applied Ocean Research*, 7 (4), 197-201.
- [32] Zhao, M., Cheng, L., Teng, B., 2007. Numerical modeling of flow and hydrodynamic forces around a piggyback pipeline near the seabed. *Journal of Waterway, Port, Coastal and Ocean Engineering*, v 133, n 4, p 286-295.
- [33] Zdravkovich, M. M. 1997. *Flow around Circular Cylinders: Vol 1: Fundamentals*. Oxford University Press, Oxford, United Kingdom.
- [34] Bosch, G., Rodi, W., 1996. Simulation of vortex shedding past a square cylinder near a wall. *International Journal of Heat and Fluid Flow*, 17 (3), 267-275.
- [35] Bo, J. C, Hui, D. L., Fang, L. D., 2003. Study of concentration fields in turbulent wake regions. *Journal of Hydraulic Research*, 41 (3), 311-318.



## Chapter 9

# Large Eddy Simulations of flow around tandem cylinders close to a horizontal wall

*Mia Abrahamsen Prsic\**, *Muk Chen Ong<sup>#</sup>*, *Bjørnar Pettersen\**, *Dag Myrhaug\**

\*Department of Marine Technology, Norwegian University of Science and Technology, Trondheim, Norway

<sup>#</sup>Norwegian Marine Technology Research Institute (MARINTEK), Trondheim, Norway

Paper 4: Not included due to copyright



## **Chapter 10**

### **Large Eddy Simulations of flow around tandem circular cylinders in the vicinity of a plane wall**

*Mia Abrahamsen Prsic\**, *Muk Chen Ong<sup>#</sup>*, *Bjørnar Pettersen\**, *Dag Myrhaug\**

*\* Department of Marine Technology, Norwegian University of Science and Technology, NO-7491 Trondheim, Norway*

*<sup>#</sup> Department of Mechanical and Structural Engineering and Materials Science, University of Stavanger, NO-4036 Stavanger, Norway*

Paper 5: Not included due to copyright





## Chapter 11

### Conclusions and suggestions for future work

Numerical simulations were performed for the flow around circular cylinders in three arrangements: in an infinite fluid and in a steady current; in the vicinity of a plane wall and in the tandem configuration close to a plane wall. LES with Smagorinsky subgrid scale model were utilised to simulate the fine structures in the cylinders wakes and to capture the complex interaction between the boundary layers, wakes and vortices.

The main conclusions are as following:

The code is successfully validated through the benchmark case of a single circular cylinder in the infinite fluid and in uniform flow at  $Re = 3900$ . Based on a careful comparison with the published experimental and detailed numerical results, LES has proven to be a suitable tool for modelling of the flow at higher subcritical  $Re$ . From the numerical point of view, attention needs to be paid to the mesh resolution in the cylinder near wake, as well as on the cylinder surface.

The presence of a plane wall in the vicinity of a circular cylinder has a strong influence on the flow characteristics. While small gaps attenuate vortex shedding, larger gaps yield asymmetric wake flow with strong interaction with the wall boundary layer. The flow around the cylinder placed more than  $1D$  away from the wall yields very mild influence of the wall. However, further downstream, the broadening wake interacts with the wall boundary layer, exposing possible objects in the wake to a complex, turbulent flow. The thickness and the shape of the incoming boundary layer flow have a milder, but significant influence on the flow. The complexity of this type of flow requests 3D simulations, while the 2D models show shortcomings.

The knowledge about the flow around tandem cylinders in the vicinity of a wall is scarce. It is, however, possible to compare such complex configuration to the better explored cases. At large gaps, the flow around tandem cylinders is not strongly influenced by the wall, and can thus be viewed through the classification of tandem

cylinders in an infinite fluid. Reattachment and extended body regimes are recognisable. The flow around narrow spaced tandem cylinders is influenced by the wall at a large gap from the plane wall, while the flow around a single cylinder, at the same gap, ceases to be influenced by the wall.

On the other hand, flow around each of the cylinders, with a large longitudinal spacing, can be compared to the flow around a single cylinder in the vicinity of a wall. The behaviour of the upstream cylinder compares well to the case of a single cylinder near a wall. The downstream cylinder is exposed to the vortices shed from upstream cylinder and distorted by the wall, causing asymmetric impingement and significant changes to the hydrodynamic loads.

As presented through all configurations, the flow around cylindrical structures acquires various behaviours, depending on  $Re$ , the presence of the wall and the spacing between the cylinders. A systematic and comprehensive classification of the flow types for each configuration is an important step in future research of these topics. Clearly classified flow characteristics can further lead to better understanding of the forces exerted on subsea structures, and thus provide basis for safer planning of their construction.

In the present study, an intermediate, subcritical  $Re$  is chosen to correspond to the realistic conditions subsea pipelines are exposed to. Offshore structures, however, encounter a large variety of environmental conditions, often corresponding to strong currents and high  $Re$ . A thorough investigation of the  $Re$  influence should be done for all mentioned configurations.

The ever increasing available computational power allows the use of precise numerical models, such as LES, for increasingly more complex flows and structures. Such detailed knowledge can be used for testing of simplified models or rational approaches used in the industry, exploring their capabilities or limitations. LES are also highly complementary to the experimental research. Precise time-dependant numerical results can easily be verified through comparison with the experiments, and further used to explore the details of the flow which are difficult to obtain experimentally.

## *Appendix*

### *List of additional publications*

Hidele Kalvig, R. B., Abrahamsen Prsic, M., Pettersen, B. (2016) Numerical investigation of 3D flow around two tandem cylinders. *Accepted for publication in Proceedings of the 26<sup>th</sup> International Ocean and Polar Engineering Conference, Rhodes, Greece, June 26 – July 2, 2016.*

Abrahamsen Prsic, M., Ong, M. C., Pettersen, B., Myrhaug, D. (2015) LES of flow around tandem cylinders close to a horizontal wall. *Proceedings of The 25<sup>th</sup> International Ocean and Polar Engineering Conference, Kona, Big Island, Hawaii, USA, June 21– 26, 2015.*

Abrahamsen Prsic, M., Ong, M. C., Pettersen, B., Myrhaug, D. (2013) Large Eddy Simulations of flow around a circular cylinder in the vicinity of a wall at Reynolds number of 13100. *MekIT'13 Seventh National Conference on Computational Mechanics, Trondheim 13-14 May 2013.*



**Previous PhD theses published at the Departement of Marine Technology**

**(earlier: Faculty of Marine Technology)**

**NORWEGIAN UNIVERSITY OF SCIENCE AND TECHNOLOGY**

<b>Report No.</b>	<b>Author</b>	<b>Title</b>
	Kavlie, Dag	Optimization of Plane Elastic Grillages, 1967
	Hansen, Hans R.	Man-Machine Communication and Data-Storage Methods in Ship Structural Design, 1971
	Gisvold, Kaare M.	A Method for non-linear mixed -integer programming and its Application to Design Problems, 1971
	Lund, Sverre	Tanker Frame Optimalization by means of SUMT-Transformation and Behaviour Models, 1971
	Vinje, Tor	On Vibration of Spherical Shells Interacting with Fluid, 1972
	Lorentz, Jan D.	Tank Arrangement for Crude Oil Carriers in Accordance with the new Anti-Pollution Regulations, 1975
	Carlsen, Carl A.	Computer-Aided Design of Tanker Structures, 1975
	Larsen, Carl M.	Static and Dynamic Analysis of Offshore Pipelines during Installation, 1976
UR-79-01	Brigt Hatlestad, MK	The finite element method used in a fatigue evaluation of fixed offshore platforms. (Dr.Ing. Thesis)
UR-79-02	Erik Pettersen, MK	Analysis and design of cellular structures. (Dr.Ing. Thesis)
UR-79-03	Sverre Valsgård, MK	Finite difference and finite element methods applied to nonlinear analysis of plated structures. (Dr.Ing. Thesis)
UR-79-04	Nils T. Nordsve, MK	Finite element collapse analysis of structural members considering imperfections and stresses due to fabrication. (Dr.Ing. Thesis)
UR-79-05	Ivar J. Fylling, MK	Analysis of towline forces in ocean towing systems. (Dr.Ing. Thesis)
UR-80-06	Nils Sandsmark, MM	Analysis of Stationary and Transient Heat Conduction by the Use of the Finite Element Method. (Dr.Ing. Thesis)
UR-80-09	Sverre Haver, MK	Analysis of uncertainties related to the stochastic modeling of ocean waves. (Dr.Ing. Thesis)
UR-81-15	Odland, Jonas	On the Strength of welded Ring stiffened cylindrical Shells primarily subjected to axial Compression
UR-82-17	Engesvik, Knut	Analysis of Uncertainties in the fatigue Capacity of Welded Joints
UR-82-18	Rye, Henrik	Ocean wave groups
UR-83-30	Eide, Oddvar Inge	On Cumulative Fatigue Damage in Steel Welded Joints
UR-83-33	Mo, Olav	Stochastic Time Domain Analysis of Slender Offshore

## Structures

UR-83-34	Amdahl, Jørgen	Energy absorption in Ship-platform impacts
UR-84-37	Morch, Morten	Motions and mooring forces of semi submersibles as determined by full-scale measurements and theoretical analysis
UR-84-38	Soares, C. Guedes	Probabilistic models for load effects in ship structures
UR-84-39	Aarsnes, Jan V.	Current forces on ships
UR-84-40	Czujko, Jerzy	Collapse Analysis of Plates subjected to Biaxial Compression and Lateral Load
UR-85-46	Alf G. Engseth, MK	Finite element collapse analysis of tubular steel offshore structures. (Dr.Ing. Thesis)
UR-86-47	Dengody Sheshappa, MP	A Computer Design Model for Optimizing Fishing Vessel Designs Based on Techno-Economic Analysis. (Dr.Ing. Thesis)
UR-86-48	Vidar Aanesland, MH	A Theoretical and Numerical Study of Ship Wave Resistance. (Dr.Ing. Thesis)
UR-86-49	Heinz-Joachim Wessel, MK	Fracture Mechanics Analysis of Crack Growth in Plate Girders. (Dr.Ing. Thesis)
UR-86-50	Jon Taby, MK	Ultimate and Post-ultimate Strength of Dented Tubular Members. (Dr.Ing. Thesis)
UR-86-51	Walter Lian, MH	A Numerical Study of Two-Dimensional Separated Flow Past Bluff Bodies at Moderate KC-Numbers. (Dr.Ing. Thesis)
UR-86-52	Bjørn Sortland, MH	Force Measurements in Oscillating Flow on Ship Sections and Circular Cylinders in a U-Tube Water Tank. (Dr.Ing. Thesis)
UR-86-53	Kurt Strand, MM	A System Dynamic Approach to One-dimensional Fluid Flow. (Dr.Ing. Thesis)
UR-86-54	Arne Edvin Løken, MH	Three Dimensional Second Order Hydrodynamic Effects on Ocean Structures in Waves. (Dr.Ing. Thesis)
UR-86-55	Sigurd Falch, MH	A Numerical Study of Slamming of Two-Dimensional Bodies. (Dr.Ing. Thesis)
UR-87-56	Arne Braathen, MH	Application of a Vortex Tracking Method to the Prediction of Roll Damping of a Two-Dimension Floating Body. (Dr.Ing. Thesis)
UR-87-57	Bernt Leira, MK	Gaussian Vector Processes for Reliability Analysis involving Wave-Induced Load Effects. (Dr.Ing. Thesis)
UR-87-58	Magnus Småvik, MM	Thermal Load and Process Characteristics in a Two-Stroke Diesel Engine with Thermal Barriers (in Norwegian). (Dr.Ing. Thesis)
MTA-88-59	Bernt Arild Bremdal, MP	An Investigation of Marine Installation Processes – A Knowledge - Based Planning Approach. (Dr.Ing. Thesis)
MTA-88-60	Xu Jun, MK	Non-linear Dynamic Analysis of Space-framed Offshore Structures. (Dr.Ing. Thesis)

MTA-89-61	Gang Miao, MH	Hydrodynamic Forces and Dynamic Responses of Circular Cylinders in Wave Zones. (Dr.Ing. Thesis)
MTA-89-62	Martin Greenhow, MH	Linear and Non-Linear Studies of Waves and Floating Bodies. Part I and Part II. (Dr.Techn. Thesis)
MTA-89-63	Chang Li, MH	Force Coefficients of Spheres and Cubes in Oscillatory Flow with and without Current. (Dr.Ing. Thesis)
MTA-89-64	Hu Ying, MP	A Study of Marketing and Design in Development of Marine Transport Systems. (Dr.Ing. Thesis)
MTA-89-65	Arild Jæger, MH	Seakeeping, Dynamic Stability and Performance of a Wedge Shaped Planing Hull. (Dr.Ing. Thesis)
MTA-89-66	Chan Siu Hung, MM	The dynamic characteristics of tilting-pad bearings
MTA-89-67	Kim Wikstrøm, MP	Analysis av projekteringen for ett offshore projekt. (Licenciat-avhandling)
MTA-89-68	Jiao Guoyang, MK	Reliability Analysis of Crack Growth under Random Loading, considering Model Updating. (Dr.Ing. Thesis)
MTA-89-69	Arnt Olufsen, MK	Uncertainty and Reliability Analysis of Fixed Offshore Structures. (Dr.Ing. Thesis)
MTA-89-70	Wu Yu-Lin, MR	System Reliability Analyses of Offshore Structures using improved Truss and Beam Models. (Dr.Ing. Thesis)
MTA-90-71	Jan Roger Hoff, MH	Three-dimensional Green function of a vessel with forward speed in waves. (Dr.Ing. Thesis)
MTA-90-72	Rong Zhao, MH	Slow-Drift Motions of a Moored Two-Dimensional Body in Irregular Waves. (Dr.Ing. Thesis)
MTA-90-73	Atle Minsaas, MP	Economical Risk Analysis. (Dr.Ing. Thesis)
MTA-90-74	Knut-Aril Farnes, MK	Long-term Statistics of Response in Non-linear Marine Structures. (Dr.Ing. Thesis)
MTA-90-75	Torbjørn Sotberg, MK	Application of Reliability Methods for Safety Assessment of Submarine Pipelines. (Dr.Ing. Thesis)
MTA-90-76	Zeuthen, Steffen, MP	SEAMAID. A computational model of the design process in a constraint-based logic programming environment. An example from the offshore domain. (Dr.Ing. Thesis)
MTA-91-77	Haagensen, Sven, MM	Fuel Dependant Cyclic Variability in a Spark Ignition Engine - An Optical Approach. (Dr.Ing. Thesis)
MTA-91-78	Løland, Geir, MH	Current forces on and flow through fish farms. (Dr.Ing. Thesis)
MTA-91-79	Hoen, Christopher, MK	System Identification of Structures Excited by Stochastic Load Processes. (Dr.Ing. Thesis)
MTA-91-80	Haugen, Stein, MK	Probabilistic Evaluation of Frequency of Collision between Ships and Offshore Platforms. (Dr.Ing. Thesis)
MTA-91-81	Sodahl, Nils, MK	Methods for Design and Analysis of Flexible Risers. (Dr.Ing. Thesis)
MTA-91-82	Ormberg, Harald, MK	Non-linear Response Analysis of Floating Fish Farm



		Systems. (Dr.Ing. Thesis)
MTA-91-83	Marley, Mark J., MK	Time Variant Reliability under Fatigue Degradation. (Dr.Ing. Thesis)
MTA-91-84	Krokstad, Jørgen R., MH	Second-order Loads in Multidirectional Seas. (Dr.Ing. Thesis)
MTA-91-85	Molteberg, Gunnar A., MM	The Application of System Identification Techniques to Performance Monitoring of Four Stroke Turbocharged Diesel Engines. (Dr.Ing. Thesis)
MTA-92-86	Mørch, Hans Jørgen Bjelke, MH	Aspects of Hydrofoil Design: with Emphasis on Hydrofoil Interaction in Calm Water. (Dr.Ing. Thesis)
MTA-92-87	Chan Siu Hung, MM	Nonlinear Analysis of Rotordynamic Instabilities in Highspeed Turbomachinery. (Dr.Ing. Thesis)
MTA-92-88	Bessason, Bjarni, MK	Assessment of Earthquake Loading and Response of Seismically Isolated Bridges. (Dr.Ing. Thesis)
MTA-92-89	Langli, Geir, MP	Improving Operational Safety through exploitation of Design Knowledge - an investigation of offshore platform safety. (Dr.Ing. Thesis)
MTA-92-90	Sævik, Svein, MK	On Stresses and Fatigue in Flexible Pipes. (Dr.Ing. Thesis)
MTA-92-91	Ask, Tor Ø., MM	Ignition and Flame Growth in Lean Gas-Air Mixtures. An Experimental Study with a Schlieren System. (Dr.Ing. Thesis)
MTA-86-92	Hessen, Gunnar, MK	Fracture Mechanics Analysis of Stiffened Tubular Members. (Dr.Ing. Thesis)
MTA-93-93	Steinebach, Christian, MM	Knowledge Based Systems for Diagnosis of Rotating Machinery. (Dr.Ing. Thesis)
MTA-93-94	Dalane, Jan Inge, MK	System Reliability in Design and Maintenance of Fixed Offshore Structures. (Dr.Ing. Thesis)
MTA-93-95	Steen, Sverre, MH	Cobblestone Effect on SES. (Dr.Ing. Thesis)
MTA-93-96	Karunakaran, Daniel, MK	Nonlinear Dynamic Response and Reliability Analysis of Drag-dominated Offshore Platforms. (Dr.Ing. Thesis)
MTA-93-97	Hagen, Arnulf, MP	The Framework of a Design Process Language. (Dr.Ing. Thesis)
MTA-93-98	Nordrik, Rune, MM	Investigation of Spark Ignition and Autoignition in Methane and Air Using Computational Fluid Dynamics and Chemical Reaction Kinetics. A Numerical Study of Ignition Processes in Internal Combustion Engines. (Dr.Ing. Thesis)
MTA-94-99	Passano, Elizabeth, MK	Efficient Analysis of Nonlinear Slender Marine Structures. (Dr.Ing. Thesis)
MTA-94-100	Kvålsvold, Jan, MH	Hydroelastic Modelling of Wetdeck Slamming on Multihull Vessels. (Dr.Ing. Thesis)
MTA-94-102	Bech, Sidsel M., MK	Experimental and Numerical Determination of Stiffness and Strength of GRP/PVC Sandwich Structures. (Dr.Ing. Thesis)
MTA-95-103	Paulsen, Hallvard, MM	A Study of Transient Jet and Spray using a Schlieren Method and Digital Image Processing. (Dr.Ing. Thesis)

MTA-95-104	Hovde, Geir Olav, MK	Fatigue and Overload Reliability of Offshore Structural Systems, Considering the Effect of Inspection and Repair. (Dr.Ing. Thesis)
MTA-95-105	Wang, Xiaozhi, MK	Reliability Analysis of Production Ships with Emphasis on Load Combination and Ultimate Strength. (Dr.Ing. Thesis)
MTA-95-106	Ulstein, Tore, MH	Nonlinear Effects of a Flexible Stern Seal Bag on Cobblestone Oscillations of an SES. (Dr.Ing. Thesis)
MTA-95-107	Solaas, Frøydis, MH	Analytical and Numerical Studies of Sloshing in Tanks. (Dr.Ing. Thesis)
MTA-95-108	Hellan, Øyvind, MK	Nonlinear Pushover and Cyclic Analyses in Ultimate Limit State Design and Reassessment of Tubular Steel Offshore Structures. (Dr.Ing. Thesis)
MTA-95-109	Hermundstad, Ole A., MK	Theoretical and Experimental Hydroelastic Analysis of High Speed Vessels. (Dr.Ing. Thesis)
MTA-96-110	Bratland, Anne K., MH	Wave-Current Interaction Effects on Large-Volume Bodies in Water of Finite Depth. (Dr.Ing. Thesis)
MTA-96-111	Herfjord, Kjell, MH	A Study of Two-dimensional Separated Flow by a Combination of the Finite Element Method and Navier-Stokes Equations. (Dr.Ing. Thesis)
MTA-96-112	Æsøy, Vilmar, MM	Hot Surface Assisted Compression Ignition in a Direct Injection Natural Gas Engine. (Dr.Ing. Thesis)
MTA-96-113	Eknes, Monika L., MK	Escalation Scenarios Initiated by Gas Explosions on Offshore Installations. (Dr.Ing. Thesis)
MTA-96-114	Erikstad, Stein O., MP	A Decision Support Model for Preliminary Ship Design. (Dr.Ing. Thesis)
MTA-96-115	Pedersen, Egil, MH	A Nautical Study of Towed Marine Seismic Streamer Cable Configurations. (Dr.Ing. Thesis)
MTA-97-116	Moksnes, Paul O., MM	Modelling Two-Phase Thermo-Fluid Systems Using Bond Graphs. (Dr.Ing. Thesis)
MTA-97-117	Halse, Karl H., MK	On Vortex Shedding and Prediction of Vortex-Induced Vibrations of Circular Cylinders. (Dr.Ing. Thesis)
MTA-97-118	Igland, Ragnar T., MK	Reliability Analysis of Pipelines during Laying, considering Ultimate Strength under Combined Loads. (Dr.Ing. Thesis)
MTA-97-119	Pedersen, Hans-P., MP	Levendefiskteknologi for fiskefartøy. (Dr.Ing. Thesis)
MTA-98-120	Vikestad, Kyrre, MK	Multi-Frequency Response of a Cylinder Subjected to Vortex Shedding and Support Motions. (Dr.Ing. Thesis)
MTA-98-121	Azadi, Mohammad R. E., MK	Analysis of Static and Dynamic Pile-Soil-Jacket Behaviour. (Dr.Ing. Thesis)
MTA-98-122	Ulltang, Terje, MP	A Communication Model for Product Information. (Dr.Ing. Thesis)
MTA-98-123	Torbergsen, Erik, MM	Impeller/Diffuser Interaction Forces in Centrifugal Pumps. (Dr.Ing. Thesis)
MTA-98-	Hansen, Edmond, MH	A Discrete Element Model to Study Marginal Ice Zone

124		Dynamics and the Behaviour of Vessels Moored in Broken Ice. (Dr.Ing. Thesis)
MTA-98-125	Videiro, Paulo M., MK	Reliability Based Design of Marine Structures. (Dr.Ing. Thesis)
MTA-99-126	Mainçon, Philippe, MK	Fatigue Reliability of Long Welds Application to Titanium Risers. (Dr.Ing. Thesis)
MTA-99-127	Haugen, Elin M., MH	Hydroelastic Analysis of Slamming on Stiffened Plates with Application to Catamaran Wetdecks. (Dr.Ing. Thesis)
MTA-99-128	Langhelle, Nina K., MK	Experimental Validation and Calibration of Nonlinear Finite Element Models for Use in Design of Aluminium Structures Exposed to Fire. (Dr.Ing. Thesis)
MTA-99-129	Berstad, Are J., MK	Calculation of Fatigue Damage in Ship Structures. (Dr.Ing. Thesis)
MTA-99-130	Andersen, Trond M., MM	Short Term Maintenance Planning. (Dr.Ing. Thesis)
MTA-99-131	Tveiten, Bård Wathne, MK	Fatigue Assessment of Welded Aluminium Ship Details. (Dr.Ing. Thesis)
MTA-99-132	Søreide, Fredrik, MP	Applications of underwater technology in deep water archaeology. Principles and practice. (Dr.Ing. Thesis)
MTA-99-133	Tønnessen, Rune, MH	A Finite Element Method Applied to Unsteady Viscous Flow Around 2D Blunt Bodies With Sharp Corners. (Dr.Ing. Thesis)
MTA-99-134	Elvekrok, Dag R., MP	Engineering Integration in Field Development Projects in the Norwegian Oil and Gas Industry. The Supplier Management of Norne. (Dr.Ing. Thesis)
MTA-99-135	Fagerholt, Kjetil, MP	Optimeringsbaserte Metoder for Ruteplanlegging innen skipsfart. (Dr.Ing. Thesis)
MTA-99-136	Bysveen, Marie, MM	Visualization in Two Directions on a Dynamic Combustion Rig for Studies of Fuel Quality. (Dr.Ing. Thesis)
MTA-2000-137	Storteig, Eskild, MM	Dynamic characteristics and leakage performance of liquid annular seals in centrifugal pumps. (Dr.Ing. Thesis)
MTA-2000-138	Sagli, Gro, MK	Model uncertainty and simplified estimates of long term extremes of hull girder loads in ships. (Dr.Ing. Thesis)
MTA-2000-139	Tronstad, Harald, MK	Nonlinear analysis and design of cable net structures like fishing gear based on the finite element method. (Dr.Ing. Thesis)
MTA-2000-140	Kroneberg, André, MP	Innovation in shipping by using scenarios. (Dr.Ing. Thesis)
MTA-2000-141	Haslum, Herbjørn Alf, MH	Simplified methods applied to nonlinear motion of spar platforms. (Dr.Ing. Thesis)
MTA-2001-142	Samdal, Ole Johan, MM	Modelling of Degradation Mechanisms and Stressor Interaction on Static Mechanical Equipment Residual Lifetime. (Dr.Ing. Thesis)
MTA-2001-143	Baarholm, Rolf Jarle, MH	Theoretical and experimental studies of wave impact underneath decks of offshore platforms. (Dr.Ing. Thesis)

MTA-2001-144	Wang, Lihua, MK	Probabilistic Analysis of Nonlinear Wave-induced Loads on Ships. (Dr.Ing. Thesis)
MTA-2001-145	Kristensen, Odd H. Holt, MK	Ultimate Capacity of Aluminium Plates under Multiple Loads, Considering HAZ Properties. (Dr.Ing. Thesis)
MTA-2001-146	Greco, Marilena, MH	A Two-Dimensional Study of Green-Water Loading. (Dr.Ing. Thesis)
MTA-2001-147	Heggelund, Svein E., MK	Calculation of Global Design Loads and Load Effects in Large High Speed Catamarans. (Dr.Ing. Thesis)
MTA-2001-148	Babalola, Olusegun T., MK	Fatigue Strength of Titanium Risers – Defect Sensitivity. (Dr.Ing. Thesis)
MTA-2001-149	Mohammed, Abuu K., MK	Nonlinear Shell Finite Elements for Ultimate Strength and Collapse Analysis of Ship Structures. (Dr.Ing. Thesis)
MTA-2002-150	Holmedal, Lars E., MH	Wave-current interactions in the vicinity of the sea bed. (Dr.Ing. Thesis)
MTA-2002-151	Rognebakke, Olav F., MH	Sloshing in rectangular tanks and interaction with ship motions. (Dr.Ing. Thesis)
MTA-2002-152	Lader, Pål Furset, MH	Geometry and Kinematics of Breaking Waves. (Dr.Ing. Thesis)
MTA-2002-153	Yang, Qinzhen, MH	Wash and wave resistance of ships in finite water depth. (Dr.Ing. Thesis)
MTA-2002-154	Melhus, Øyvind, MM	Utilization of VOC in Diesel Engines. Ignition and combustion of VOC released by crude oil tankers. (Dr.Ing. Thesis)
MTA-2002-155	Ronæss, Marit, MH	Wave Induced Motions of Two Ships Advancing on Parallel Course. (Dr.Ing. Thesis)
MTA-2002-156	Økland, Ole D., MK	Numerical and experimental investigation of whipping in twin hull vessels exposed to severe wet deck slamming. (Dr.Ing. Thesis)
MTA-2002-157	Ge, Chunhua, MK	Global Hydroelastic Response of Catamarans due to Wet Deck Slamming. (Dr.Ing. Thesis)
MTA-2002-158	Byklum, Eirik, MK	Nonlinear Shell Finite Elements for Ultimate Strength and Collapse Analysis of Ship Structures. (Dr.Ing. Thesis)
IMT-2003-1	Chen, Haibo, MK	Probabilistic Evaluation of FPSO-Tanker Collision in Tandem Offloading Operation. (Dr.Ing. Thesis)
IMT-2003-2	Skaugset, Kjetil Bjørn, MK	On the Suppression of Vortex Induced Vibrations of Circular Cylinders by Radial Water Jets. (Dr.Ing. Thesis)
IMT-2003-3	Chezian, Muthu	Three-Dimensional Analysis of Slamming. (Dr.Ing. Thesis)
IMT-2003-4	Buhaug, Øyvind	Deposit Formation on Cylinder Liner Surfaces in Medium Speed Engines. (Dr.Ing. Thesis)
IMT-2003-5	Tregde, Vidar	Aspects of Ship Design: Optimization of Aft Hull with Inverse Geometry Design. (Dr.Ing. Thesis)

Statistical Properties of Successive Ocean Wave Parameters.

		(Dr.Ing. Thesis)
IMT-2003-6	Wist, Hanne Therese	
IMT-2004-7	Ransau, Samuel	Numerical Methods for Flows with Evolving Interfaces. (Dr.Ing. Thesis)
IMT-2004-8	Soma, Torkel	Blue-Chip or Sub-Standard. A data interrogation approach of identity safety characteristics of shipping organization. (Dr.Ing. Thesis)
IMT-2004-9	Ersdal, Svein	An experimental study of hydrodynamic forces on cylinders and cables in near axial flow. (Dr.Ing. Thesis)
IMT-2005-10	Brodtkorb, Per Andreas	The Probability of Occurrence of Dangerous Wave Situations at Sea. (Dr.Ing. Thesis)
IMT-2005-11	Yttervik, Rune	Ocean current variability in relation to offshore engineering. (Dr.Ing. Thesis)
IMT-2005-12	Fredheim, Arne	Current Forces on Net-Structures. (Dr.Ing. Thesis)
IMT-2005-13	Heggernes, Kjetil	Flow around marine structures. (Dr.Ing. Thesis)
IMT-2005-14	Fouques, Sebastien	Lagrangian Modelling of Ocean Surface Waves and Synthetic Aperture Radar Wave Measurements. (Dr.Ing. Thesis)
IMT-2006-15	Holm, Håvard	Numerical calculation of viscous free surface flow around marine structures. (Dr.Ing. Thesis)
IMT-2006-16	Bjørheim, Lars G.	Failure Assessment of Long Through Thickness Fatigue Cracks in Ship Hulls. (Dr.Ing. Thesis)
IMT-2006-17	Hansson, Lisbeth	Safety Management for Prevention of Occupational Accidents. (Dr.Ing. Thesis)
IMT-2006-18	Zhu, Xinying	Application of the CIP Method to Strongly Nonlinear Wave-Body Interaction Problems. (Dr.Ing. Thesis)
IMT-2006-19	Reite, Karl Johan	Modelling and Control of Trawl Systems. (Dr.Ing. Thesis)
IMT-2006-20	Smogeli, Øyvind Notland	Control of Marine Propellers. From Normal to Extreme Conditions. (Dr.Ing. Thesis)
IMT-2007-21	Storhaug, Gaute	Experimental Investigation of Wave Induced Vibrations and Their Effect on the Fatigue Loading of Ships. (Dr.Ing. Thesis)
IMT-2007-22	Sun, Hui	A Boundary Element Method Applied to Strongly Nonlinear Wave-Body Interaction Problems. (PhD Thesis, CeSOS)
IMT-2007-23	Rustad, Anne Marthine	Modelling and Control of Top Tensioned Risers. (PhD Thesis, CeSOS)
IMT-2007-24	Johansen, Vegar	Modelling flexible slender system for real-time simulations and control applications
IMT-2007-25	Wroldsen, Anders Sunde	Modelling and control of tensegrity structures. (PhD Thesis, CeSOS)

IMT-2007-26	Aronsen, Kristoffer Høy	An experimental investigation of in-line and combined inline and cross flow vortex induced vibrations. (Dr. avhandling, IMT)
IMT-2007-27	Gao, Zhen	Stochastic Response Analysis of Mooring Systems with Emphasis on Frequency-domain Analysis of Fatigue due to Wide-band Response Processes (PhD Thesis, CeSOS)
IMT-2007-28	Thorstensen, Tom Anders	Lifetime Profit Modelling of Ageing Systems Utilizing Information about Technical Condition. (Dr.ing. thesis, IMT)
IMT-2008-29	Refsnes, Jon Erling Gorset	Nonlinear Model-Based Control of Slender Body AUVs (PhD Thesis, IMT)
IMT-2008-30	Berntsen, Per Ivar B.	Structural Reliability Based Position Mooring. (PhD-Thesis, IMT)
IMT-2008-31	Ye, Naiquan	Fatigue Assessment of Aluminium Welded Box-stiffener Joints in Ships (Dr.ing. thesis, IMT)
IMT-2008-32	Radan, Damir	Integrated Control of Marine Electrical Power Systems. (PhD-Thesis, IMT)
IMT-2008-33	Thomassen, Paul	Methods for Dynamic Response Analysis and Fatigue Life Estimation of Floating Fish Cages. (Dr.ing. thesis, IMT)
IMT-2008-34	Pákozdi, Csaba	A Smoothed Particle Hydrodynamics Study of Two-dimensional Nonlinear Sloshing in Rectangular Tanks. (Dr.ing.thesis, IMT/ CeSOS)
IMT-2007-35	Grytøyr, Guttorm	A Higher-Order Boundary Element Method and Applications to Marine Hydrodynamics. (Dr.ing.thesis, IMT)
IMT-2008-36	Drummen, Ingo	Experimental and Numerical Investigation of Nonlinear Wave-Induced Load Effects in Containerships considering Hydroelasticity. (PhD thesis, CeSOS)
IMT-2008-37	Skejic, Renato	Maneuvering and Seakeeping of a Singel Ship and of Two Ships in Interaction. (PhD-Thesis, CeSOS)
IMT-2008-38	Harlem, Alf	An Age-Based Replacement Model for Repairable Systems with Attention to High-Speed Marine Diesel Engines. (PhD-Thesis, IMT)
IMT-2008-39	Alsos, Hagbart S.	Ship Grounding. Analysis of Ductile Fracture, Bottom Damage and Hull Girder Response. (PhD-thesis, IMT)
IMT-2008-40	Graczyk, Mateusz	Experimental Investigation of Sloshing Loading and Load Effects in Membrane LNG Tanks Subjected to Random Excitation. (PhD-thesis, CeSOS)
IMT-2008-41	Taghipour, Reza	Efficient Prediction of Dynamic Response for Flexible and Multi-body Marine Structures. (PhD-thesis, CeSOS)
IMT-2008-42	Ruth, Eivind	Propulsion control and thrust allocation on marine vessels. (PhD thesis, CeSOS)
IMT-2008-43	Nystad, Bent Helge	Technical Condition Indexes and Remaining Useful Life of Aggregated Systems. PhD thesis, IMT
IMT-2008-44	Soni, Prashant Kumar	Hydrodynamic Coefficients for Vortex Induced Vibrations of Flexible Beams, PhD thesis,

CeSOS

IMT-2009-45	Amlashi, Hadi K.K.	Ultimate Strength and Reliability-based Design of Ship Hulls with Emphasis on Combined Global and Local Loads. PhD Thesis, IMT
IMT-2009-46	Pedersen, Tom Arne	Bond Graph Modelling of Marine Power Systems. PhD Thesis, IMT
IMT-2009-47	Kristiansen, Trygve	Two-Dimensional Numerical and Experimental Studies of Piston-Mode Resonance. PhD-Thesis, CeSOS
IMT-2009-48	Ong, Muk Chen	Applications of a Standard High Reynolds Number Model and a Stochastic Scour Prediction Model for Marine Structures. PhD-thesis, IMT
IMT-2009-49	Hong, Lin	Simplified Analysis and Design of Ships subjected to Collision and Grounding. PhD-thesis, IMT
IMT-2009-50	Koushan, Kamran	Vortex Induced Vibrations of Free Span Pipelines, PhD thesis, IMT
IMT-2009-51	Korsvik, Jarl Eirik	Heuristic Methods for Ship Routing and Scheduling. PhD-thesis, IMT
IMT-2009-52	Lee, Jihoon	Experimental Investigation and Numerical in Analyzing the Ocean Current Displacement of Longlines. Ph.d.-Thesis, IMT.
IMT-2009-53	Vestbøstad, Tone Gran	A Numerical Study of Wave-in-Deck Impact using a Two-Dimensional Constrained Interpolation Profile Method, Ph.d.thesis, CeSOS.
IMT-2009-54	Bruun, Kristine	Bond Graph Modelling of Fuel Cells for Marine Power Plants. Ph.d.-thesis, IMT
IMT 2009-55	Holstad, Anders	Numerical Investigation of Turbulence in a Skewed Three-Dimensional Channel Flow, Ph.d.-thesis, IMT.
IMT 2009-56	Ayala-Uraga, Efrén	Reliability-Based Assessment of Deteriorating Ship-shaped Offshore Structures, Ph.d.-thesis, IMT
IMT 2009-57	Kong, Xiangjun	A Numerical Study of a Damaged Ship in Beam Sea Waves. Ph.d.-thesis, IMT/CeSOS.
IMT 2010-58	Kristiansen, David	Wave Induced Effects on Floaters of Aquaculture Plants, Ph.d.-thesis, CeSOS.
IMT 2010-59	Ludvigsen, Martin	An ROV-Toolbox for Optical and Acoustic Scientific Seabed Investigation. Ph.d.-thesis IMT.
IMT 2010-60	Hals, Jørgen	Modelling and Phase Control of Wave-Energy Converters. Ph.d.thesis, CeSOS.
IMT 2010-61	Shu, Zhi	Uncertainty Assessment of Wave Loads and Ultimate Strength of Tankers and Bulk Carriers in a Reliability Framework. Ph.d. Thesis, IMT/ CeSOS
IMT 2010-62	Shao, Yanlin	Numerical Potential-Flow Studies on Weakly-Nonlinear Wave-Body Interactions with/without Small Forward Speed, Ph.d.thesis,CeSOS.

IMT 2010-63	Califano, Andrea	Dynamic Loads on Marine Propellers due to Intermittent Ventilation. Ph.d.thesis, IMT.
IMT 2010-64	El Khoury, George	Numerical Simulations of Massively Separated Turbulent Flows, Ph.d.-thesis, IMT
IMT 2010-65	Seim, Knut Sponheim	Mixing Process in Dense Overflows with Emphasis on the Faroe Bank Channel Overflow. Ph.d.thesis, IMT
IMT 2010-66	Jia, Huirong	Structural Analysis of Intact and Damaged Ships in a Collision Risk Analysis Perspective. Ph.d.thesis CeSOS.
IMT 2010- 67	Jiao, Linlin	Wave-Induced Effects on a Pontoon-type Very Large Floating Structures (VLFS). Ph.D.-thesis, CeSOS.
IMT 2010- 68	Abrahamsen, Bjørn Christian	Sloshing Induced Tank Roof Impact with Entrapped Air Pocket. Ph.d.thesis, CeSOS.
IMT 2011- 69	Karimirad, Madjid	Stochastic Dynamic Response Analysis of Spar-Type Wind Turbines with Catenary or Taut Mooring Systems. Ph.d.-thesis, CeSOS.
IMT -2011- 70	Erlend Meland	Condition Monitoring of Safety Critical Valves. Ph.d.-thesis, IMT.
IMT – 2011-71	Yang, Limin	Stochastic Dynamic System Analysis of Wave Energy Converter with Hydraulic Power Take-Off, with Particular Reference to Wear Damage Analysis, Ph.d. Thesis, CeSOS.
IMT – 2011-72	Visscher, Jan	Application of Particle Image Velocimetry on Turbulent Marine Flows, Ph.d.Thesis, IMT.
IMT – 2011-73	Su, Biao	Numerical Predictions of Global and Local Ice Loads on Ships. Ph.d.Thesis, CeSOS.
IMT – 2011-74	Liu, Zhenhui	Analytical and Numerical Analysis of Iceberg Collision with Ship Structures. Ph.d.Thesis, IMT.
IMT – 2011-75	Aarsæther, Karl Gunnar	Modeling and Analysis of Ship Traffic by Observation and Numerical Simulation. Ph.d.Thesis, IMT.
Imt – 2011- 76	Wu, Jie	Hydrodynamic Force Identification from Stochastic Vortex Induced Vibration Experiments with Slender Beams. Ph.d.Thesis, IMT.
Imt – 2011- 77	Amini, Hamid	Azimuth Propulsors in Off-design Conditions. Ph.d.Thesis, IMT.
IMT – 2011-78	Nguyen, Tan-Hoi	Toward a System of Real-Time Prediction and Monitoring of Bottom Damage Conditions During Ship Grounding. Ph.d.thesis, IMT.
IMT- 2011- 79	Tavakoli, Mohammad T.	Assessment of Oil Spill in Ship Collision and Grounding, Ph.d.thesis, IMT.
IMT- 2011- 80	Guo, Bingjie	Numerical and Experimental Investigation of Added Resistance in Waves. Ph.d.Thesis, IMT.



IMT- 2011-81	Chen, Qiaofeng	Ultimate Strength of Aluminium Panels, considering HAZ Effects, IMT
IMT-2012-82	Kota, Ravikiran S.	Wave Loads on Decks of Offshore Structures in Random Seas, CeSOS.
IMT-2012-83	Sten, Ronny	Dynamic Simulation of Deep Water Drilling Risers with Heave Compensating System, IMT.
IMT-2012-84	Berle, Øyvind	Risk and resilience in global maritime supply chains, IMT.
IMT-2012-85	Fang, Shaoji	Fault Tolerant Position Mooring Control Based on Structural Reliability, CeSOS.
IMT-2012-86	You, Jikun	Numerical studies on wave forces and moored ship motions in intermediate and shallow water, CeSOS.
IMT-2012-87	Xiang ,Xu	Maneuvering of two interacting ships in waves, CeSOS
IMT-2012-88	Dong, Wenbin	Time-domain fatigue response and reliability analysis of offshore wind turbines with emphasis on welded tubular joints and gear components, CeSOS
IMT-2012-89	Zhu, Suji	Investigation of Wave-Induced Nonlinear Load Effects in Open Ships considering Hull Girder Vibrations in Bending and Torsion, CeSOS
IMT-2012-90	Zhou, Li	Numerical and Experimental Investigation of Station-keeping in Level Ice, CeSOS
IMT-2012-91	Ushakov, Sergey	Particulate matter emission characteristics from diesel engines operating on conventional and alternative marine fuels, IMT
IMT-2013-1	Yin, Decao	Experimental and Numerical Analysis of Combined In-line and Cross-flow Vortex Induced Vibrations, CeSOS
IMT-2013-2	Kurniawan, Adi	Modelling and geometry optimisation of wave energy converters, CeSOS
IMT- 2013-3	Al Ryati, Nabil	Technical condition indexes doe auxiliary marine diesel engines, IMT
IMT-2013-4	Firoozkoohi, Reza	Experimental, numerical and analytical investigation of the effect of screens on sloshing, CeSOS
IMT-2013-5	Ommani, Babak	Potential-Flow Predictions of a Semi-Displacement Vessel Including Applications to Calm Water Broaching, CeSOS
IMT- 2013-6	Xing, Yihan	Modelling and analysis of the gearbox in a floating spar-type wind turbine, CeSOS
IMT-7-2013	Balland, Océane	Optimization models for reducing air emissions from ships, IMT
IMT-8-2013	Yang, Dan	Transitional wake flow behind an inclined flat plate----- Computation and analysis, IMT

IMT-9-2013	Abdillah, Suyuthi	Prediction of Extreme Loads and Fatigue Damage for a Ship Hull due to Ice Action, IMT
IMT-10-2013	Ramirez, Pedro Agustin Pérez	Ageing management and life extension of technical systems- Concepts and methods applied to oil and gas facilities, IMT
IMT-11-2013	Chuang, Zhenju	Experimental and Numerical Investigation of Speed Loss due to Seakeeping and Maneuvering, IMT
IMT-12-2013	Etemaddar, Mahmoud	Load and Response Analysis of Wind Turbines under Atmospheric Icing and Controller System Faults with Emphasis on Spar Type Floating Wind Turbines, IMT
IMT-13-2013	Lindstad, Haakon	Strategies and measures for reducing maritime CO2 emissions, IMT
IMT-14-2013	Haris, Sabril	Damage interaction analysis of ship collisions, IMT
IMT-15-2013	Shainee, Mohamed	Conceptual Design, Numerical and Experimental Investigation of a SPM Cage Concept for Offshore Mariculture, IMT
IMT-16-2013	Gansel, Lars	Flow past porous cylinders and effects of biofouling and fish behavior on the flow in and around Atlantic salmon net cages, IMT
IMT-17-2013	Gaspar, Henrique	Handling Aspects of Complexity in Conceptual Ship Design, IMT
IMT-18-2013	Thys, Maxime	Theoretical and Experimental Investigation of a Free Running Fishing Vessel at Small Frequency of Encounter, CeSOS
IMT-19-2013	Aglen, Ida	VIV in Free Spanning Pipelines, CeSOS
IMT-1-2014	Song, An	Theoretical and experimental studies of wave diffraction and radiation loads on a horizontally submerged perforated plate, CeSOS
IMT-2-2014	Rogne, Øyvind Ygre	Numerical and Experimental Investigation of a Hinged 5-body Wave Energy Converter, CeSOS
IMT-3-2014	Dai, Lijuan	Safe and efficient operation and maintenance of offshore wind farms, IMT
IMT-4-2014	Bachynski, Erin Elizabeth	Design and Dynamic Analysis of Tension Leg Platform Wind Turbines, CeSOS
IMT-5-2014	Wang, Jingbo	Water Entry of Freefall Wedged – Wedge motions and Cavity Dynamics, CeSOS
IMT-6-2014	Kim, Ekaterina	Experimental and numerical studies related to the coupled behavior of ice mass and steel structures during accidental collisions, IMT
IMT-7-2014	Tan, Xiang	Numerical investigation of ship's continuous- mode icebreaking in level ice, CeSOS
IMT-8-2014	Muliawan, Made Jaya	Design and Analysis of Combined Floating Wave and Wind Power Facilities, with Emphasis on Extreme Load Effects of the Mooring System, CeSOS

IMT-9-2014	Jiang, Zhiyu	Long-term response analysis of wind turbines with an emphasis on fault and shutdown conditions, IMT
IMT-10-2014	Dukan, Fredrik	ROV Motion Control Systems, IMT
IMT-11-2014	Grimsmo, Nils I.	Dynamic simulations of hydraulic cylinder for heave compensation of deep water drilling risers, IMT
IMT-12-2014	Kvittem, Marit I.	Modelling and response analysis for fatigue design of a semisubmersible wind turbine, CeSOS
IMT-13-2014	Akhtar, Juned	The Effects of Human Fatigue on Risk at Sea, IMT
IMT-14-2014	Syahroni, Nur	Fatigue Assessment of Welded Joints Taking into Account Effects of Residual Stress, IMT
IMT-1-2015	Böckmann, Eirik	Wave Propulsion of ships, IMT
IMT-2-2015	Wang, Kai	Modelling and dynamic analysis of a semi-submersible floating vertical axis wind turbine, CeSOS
IMT-3-2015	Fredriksen, Arnt Gunvald	A numerical and experimental study of a two-dimensional body with moonpool in waves and current, CeSOS
IMT-4-2015	Jose Patricio Gallardo Canabes	Numerical studies of viscous flow around bluff bodies, IMT
IMT-5-2015	Vegard Longva	Formulation and application of finite element techniques for slender marine structures subjected to contact interactions, IMT
IMT-6-2015	Jacobus De Vaal	Aerodynamic modelling of floating wind turbines, CeSOS
IMT-7-2015	Fachri Nasution	Fatigue Performance of Copper Power Conductors, IMT
IMT-8-2015	Oleh I Karpa	Development of bivariate extreme value distributions for applications in marine technology, CeSOS
IMT-9-2015	Daniel de Almeida Fernandes	An output feedback motion control system for ROVs, AMOS
IMT-10-2015	Bo Zhao	Particle Filter for Fault Diagnosis: Application to Dynamic Positioning Vessel and Underwater Robotics, CeSOS
IMT-11-2015	Wenting Zhu	Impact of emission allocation in maritime transportation, IMT
IMT-12-2015	Amir Rasekhi Nejad	Dynamic Analysis and Design of Gearboxes in Offshore Wind Turbines in a Structural Reliability Perspective, CeSOS
IMT-13-2015	Arturo Jesús Ortega Malca	Dynamic Response of Flexibles Risers due to Unsteady Slug Flow, CeSOS
IMT-14-2015	Dagfinn Husjord	Guidance and decision-support system for safe navigation of ships operating in close proximity, IMT
IMT-15-2015	Anirban Bhattacharyya	Ducted Propellers: Behaviour in Waves and Scale Effects, IMT

IMT-16-2015	Qin Zhang	Image Processing for Ice Parameter Identification in Ice Management, IMT
IMT-1-2016	Vincentius Rumawas	Human Factors in Ship Design and Operation: An Experiential Learning, IMT
IMT-2-2016	Martin Storheim	Structural response in ship-platform and ship-ice collisions, IMT
IMT-3-2016	Mia Abrahamsen Prsic	Numerical Simulations of the Flow around single and Tandem Circular Cylinders Close to a Plane Wall, IMT